University of Glasgow

Edgar, Matthew Patrick (2011) *Experimental investigations into diffractive optics and optomechanical systems for future gravitational wave detectors.*
PhD thesis.

http://theses.gla.ac.uk/2927/

Experimental Investigations into Diffractive Optics and Optomechanical Systems for Future Gravitational Wave Detectors

Matthew Patrick Edgar, B.Sc.

School of Physics and Astronomy,

University of Glasgow

Presented as a thesis for the degree of Ph.D.

in the University of Glasgow, University Avenue,

Glasgow G12 8QQ

October 15, 2011

Contents

List of Figures

List of Tables

Acknowledgements

I must say, if I can do it, anyone can! Seriously.

I came to this field with wide eyes, a large imagination, and a positive attitude. Three parts of my personality that were slowly squashed by the daily level of work required, but then inflated again by the people surrounding me. So, a well deserved thank you is in order to all those people who made me believe in the light at the end of the vacuum system. There are many people that deserve a mention so bear with me.

Firstly, I would like to thank Ken Strain, Jim Hough, and Sheila Rowan for taking me on as a PhD student, with only the letters BSc to my name, and their continued encouragement, help and excellent support throughout. I can honestly say joining this group was one of the best decisions of my short life so far. You gave me the opportunity to get involved with scientific outreach, and travel across the world from New York to Berlin to Japan. Thanks also to Stefan Hild for his help and support in the latter stages of my PhD.

So, from the moment I stepped foot into the group as a new "lazy-boy", an overwhelming big thanks goes to Bryan Barr, for your endless patience, help and support throughout my entire PhD and beyond. It's good to know there is someone who knows most of the answers when you really need help, and

One legendary person, who may never read this but is the reason I studied Physics in the first place, is the inspirational teacher Mr Harkins! Thank you.

I specially want to thank my fiancé Samantha for her love and support over the years, and for making me the happiest man in the known Universe!

Finally, I would like to thank my loving parents, my brother, my sister and the rest of my encouraging family who believe in me. Without you I would not have had the confidence to undertake my PhD.

To anyone I have somehow forgotten to mention, thank you, whoever and wherever you are.

"Yesterday is history, tomorrow is a mystery, but today is a gift, that's why they call it the present."

- The wise old turtle, Kung Fu Panda

Preface

Chapter 1 details the nature of gravitational waves by developing Einstein's General Theory of Relativity. From this analysis potential sources of astronomical origin are discussed, revealing the frequency bandwidth for which gravitational wave detectors are optimised.

Chapter 2 outlines the different interferometric topologies currently used for large baseline gravitational wave detectors. The length sensing scheme for controlling the various separations between each optical component is also discussed. A summary is given of the different noise sources that limit the ground-based detectors and suitable expressions for quantifying these processes are provided.

Chapter 3 contains the first experimental demonstration of a triple-suspended diffractively-coupled Fabry-Pérot cavity utilising one of the arms in the Glasgow 10 m prototype interferometer. The motivation for employing grating devices in future gravitational wave detectors is highlighted, followed by a discussion of the different fabrication techniques and a detailed summary of the benefits related to different design choices. A full experimental design and characterisation of the grating under investigation is presented, with a further analysis performed on the effects associated to the dynamic behaviour of such systems. The work included in this chapter was performed in collaboration

with Dr Bryan Barr, Dr Oliver Burmeister, Mr Jonathan Hallam, Dr John Nelson and Dr Mike Plissi.

Chapter 4 presents the research on the modified dynamic behaviour of suspended cavity mirrors when acted upon by sufficiently large radiation pressure forces. The choice of design for the light-weight mirror and associated suspension that was required for this investigation is provided, including conclusions on its construction and ease of installation. The observed results are discussed in context with a numerical model that was derived. The work presented in this chapter was carried out in collaboration with Dr Bryan Barr, Dr Mike Plissi and Dr Sabina Huttner.

Chapter 5 summarises the results from both experiments, providing conclusions on the research in context with challenges for the wider collaboration and future work.

Summary

In 1916 Einstein published his General Theory of Relativity, from which the existence of gravitational waves was predicted. Gravitational waves are considered to be ripples or fluctuations in the curvature of space-time, propagating isotropically from their source at the speed of light. However, due to the weak nature of gravity, observing this phenomenon presents a great challenge to the scientific community.

Small deviations in the apparent positions of stellar objects were measured by Eddington during a solar eclipse in 1919, which confirmed the curvature of space-time and its effect on light, and there have since been many astronomical observations of gravitational lenses. In 1993 Hulse and Taylor were awarded the Nobel Prize in Physics for their observations of a pulsar in a binary system, providing strong evidence for energy loss by emission of gravitational waves. However, the quest for a direct detection of gravitational waves is ongoing through the development of ever more sensitive technology.

The development of laser interferometry, based on Michelson topologies, provides the most encouraging route to observing gravitational radiation. There is currently a global network of first generation interferometric gravitational wave detectors in operation, including GEO600 (UK/Germany), Virgo (Italy/France) and TAMA (Japan) as well as several second generation detectors under con-

struction such as Advanced LIGO (USA) and LIGO-Australia (Australia). In the coming years GEO600 will also undergo a series of small sequential upgrades to GEO-HF, while Virgo aims to become an order of magnitude more sensitive across the entire frequency band, as Advanced Virgo.

The Institute for Gravitational Research (IGR) at the University of Glasgow has for many years been in strong collaboration with the Albert Einstein Institute in Hanover and Golm, the University of Hanover, the University of Cardiff and the University of Birmingham. The Glasgow group have been involved with developments on GEO600 since its initial construction in 1995, from which a lot of technology has been subsequently adopted for use in other large baseline detectors. There is a 10 m prototype interferometer housed in the JIF laboratory at Glasgow, which is utilised for testing new technology and optical configurations of interest to this and the wider collaboration.

The research contained in this thesis has been carried out on the Glasgow prototype to investigate novel technology of potential importance to future generations of gravitational wave detectors.

In Chapter 1 the history of gravitational radiation is discussed, along with a summary of Einstein's General Theory of Relativity to reveal the nature of gravitational radiation production. From this analysis several potential sources of astronomical origin are detailed for which the design of ground based detectors are optimised.

Various interferometric solutions for detecting gravitational waves are described in Chapter 2, beginning with the most fundamental Michelson topology and thereupon key enhancements, such as Fabry-Pérot cavities, power recycling and signal recycling are outlined. The Pound-Drever-Hall scheme used to sense and control the relative distances between each optical component is

detailed, including modifications to this technique for controlling significantly more complex systems with many optical elements.

The most important attribute in the overall design of an interferometric gravitational wave detector is the total noise limit to the sensitivity, which is comprised of both technical noise and fundamental noise. A summary is provided of the seismic, thermal, and laser noise contributing to technical noise as well as the fundamental quantum noise, consisting of photon shot noise and radiation pressure noise. From this discussion, the author introduces the current global network, and proposed future generations of ground-based detectors intended to open a new field of gravitational wave astronomy.

In all proposed upgrades and future detectors the input power must be increased to improve detector sensitivity. Two experiments were designed, constructed and completed at the Glasgow prototype interferometer related to separate issues of concern for high power regimes.

In the first experiment, one of the arms of the Glasgow prototype was commissioned as an all-reflective optical cavity, whereby the partially transmissive input mirror was replaced with a three-port diffraction grating mounted on the bottom stage of a triple pendulum. This investigation was designed to characterise the performance of the grating compared to the conventional input mirror of a Fabry-Pérot cavity, whilst revealing issues related to the dynamics of suspended grating input couplers on the control signals. The realisation of grating devices for use in interferometric systems would open a pathway to mitigating the otherwise limiting thermal noise associated to the mirror coatings.

The other arm of the Glasgow prototype was chosen to investigate the modified dynamic behaviour of suspended cavity mirrors when signifiant radiation

pressure forces are incident. The experiment involved replacing one of the suspended cavity mirrors with a light-weight counterpart designed specifically to increase the overall sensitivity to radiation pressure. By probing the system response for different cavity detunings, it was possible to observe and characterise the opto-mechanical resonance, commonly termed an *optical spring*, which induces optical rigidity at lower frequencies and enhanced sensitivity around the resonant feature.

Although optical rigidity suppresses the system response, which is otherwise undesired within gravitational wave detectors, it does however enable systems, which under the right conditions can be self-locking, i.e. the mirror control turned off. Furthermore, the enhanced detector sensitivity at the optical spring frequency can be optimised for different frequencies of interest, and could potentially be used to beat the limit imposed by the Heisenberg Uncertainty Principle for independent cavity mirrors.

Together, these experiments may provide information useful to the design of future interferometric gravitational wave detectors.

Chapter 1

The History, Nature and Sources of Gravitational Radiation

1.1   Introduction

Gravity is a rather special force. This is because it is almost completely different from the other known forces. Gravity appears to have an infinite reach upon the universe and is inherently connected with the geometrical properties of space and time. The earlier notions of Newtonian gravity described it as a simple force acting instantaneously between bodies with mass, from which the dynamics of our own solar system could be understood. Newton's interpretation of this unique force was quite simple and yet also reasonably robust, taking centre stage for several hundred years and proving its worth with, for example, the prediction and eventual discovery of the planet Neptune based on the orbital motions of Uranus. However, nearly one hundred years ago, when

the concept of inertial frames had been introduced and Einstein was formulating the Special Theory of Relativity [1] it became obvious that the theory of gravity was incompatible with the current understanding. This led Einstein to develop the General Theory of Relativity in 1916 [2] where he described gravity as a property of space-time. Einstein proposed that space-time was not flat but instead curved by the presence of mass or energy. From this theory it was shown that accelerating mass would generate gravitational radiation, which is commonly termed gravitational waves, and these waves will propagate isotropically from their source at the speed of light. The relatively weak strength of gravitational waves is important for two reasons; firstly, it means that they can propagate where electromagnetic radiation would otherwise be blocked, and second it requires very sensitive instrumentation in order to detect them.

The rest of this chapter is dedicated to the theory of relativity and generation of gravitational waves, and highlights why laser interferometers are the optimum tool for their detection. I will also include some detail on the types of source that are likely candidates for generating strong enough levels of radiation for detection and their associated noise limits.

1.2   A Brief Summary of Relativity

Einstein's Special Theory of Relativity states that the space-time interval ds between two points is given by:

$$ds^2 = \eta_{\mu\nu}dx^\mu dx^\nu, \tag{1.1}$$

with the Minkowski metric of flat space-time, $\eta_{\mu\nu}$, given in cartesian coordinates by

$$\eta_{\mu\nu} = \begin{pmatrix} -c^2 & 0 & 0 & 0 \\ 0 & 1 & 0 & 0 \\ 0 & 0 & 1 & 0 \\ 0 & 0 & 0 & 1 \end{pmatrix}. \tag{1.2}$$

In General Relativity the presence of mass causes space-time to curve giving a space-time interval defined by

$$ds^2 = g_{\mu\nu}dx^\mu dx^\nu, \tag{1.3}$$

with all information about the space-time curvature described by the metric $g_{\mu\nu}$. It is the curvature of space-time that we experience which we call gravity.

In the absence of a gravitational field space-time is flat. We define a weak gravitational field as one in which space-time is nearly flat and so can define

$$g_{\mu\nu} = \eta_{\mu\nu} + h_{\mu\nu}, \tag{1.4}$$

where $h_{\mu\nu}$ is a small perturbation from Minkowski space-time. Equation 1.4 is known as a nearly Lorentz coordinate system. It can be shown that an arbitrary small vector ξ^μ can be applied to x^μ without altering our assumption that space-time is nearly flat. It is therefore permissible to choose the components of ξ^μ to make Einstein's equations as simple as possible. This is known as choosing a coordinate system, or gauge, for the problem and there is one in particular in which the behaviour of gravitational waves becomes evident - the Lorentz gauge. Therefore, we can write Einstein's Field equations as a wave equation [3], i.e.

$$\left(\nabla^2 - \frac{1}{c^2}\frac{\delta^2}{\delta t^2} \right) h_{\mu\nu} = 0, \tag{1.5}$$

with the elements of $h_{\mu\nu}$ taking the form $h(2\pi ft - \mathbf{k}.\mathbf{x})$, and the frequency of the wave $f = (|\mathbf{k}|/2\pi)c$, describing a plane wave propagating in the direction $\hat{k} \equiv \mathbf{k}/|\mathbf{k}|$ at the speed of light.

To obtain the wave amplitude components in their simplest form, we can choose the transverse-traceless gauge, which is a small adjustment to the original Lorentz gauge transformation and satisfies the Lorentz condition. Then by orientating our coordinate system so that the plane wave is travelling in the positive z direction, this gives

$$h_{\mu\nu} = \begin{pmatrix} 0 & 0 & 0 & 0 \\ 0 & a & b & 0 \\ 0 & b & -a & 0 \\ 0 & 0 & 0 & 0 \end{pmatrix}. \tag{1.6}$$

In other words, the propagating gravitational perturbation can be written as the sum of two components, $h = ah_+ + bh_\times$, where

$$h_+ = \begin{pmatrix} 0 & 0 & 0 & 0 \\ 0 & 1 & 0 & 0 \\ 0 & 0 & -1 & 0 \\ 0 & 0 & 0 & 0 \end{pmatrix} \tag{1.7}$$

and

$$h_\times = \begin{pmatrix} 0 & 0 & 0 & 0 \\ 0 & 0 & 1 & 0 \\ 0 & 1 & 0 & 0 \\ 0 & 0 & 0 & 0 \end{pmatrix}. \tag{1.8}$$

Therefore, this analysis has shown that there are two distinct linear polarisations of the wave that are termed 'plus' (+) and 'cross' (×).

By inserting the solution to gravitational wave amplitude into Equation 1.4 we can obtain the space-time interval from Equation 1.3 to obtain

$$ds^2 = (1 + h_+)dx^2 + 2(1 + h_\times)dxdy + (1 - h_+)dy^2 - cdt^2. \tag{1.9}$$

As will be discussed later, laser interferometers are used for the detection of gravitational waves. The quadrupolar nature of gravitational waves means

that these relatively old precision instruments are ideal tools for their detection. The basic principle behind these detectors (a more detailed discussion of this material can be found in Saulson 1994 [4]) is to measure the effect the gravitational wave will have on two beams of light that are travelling in orthogonal directions. Considering the case when one beam is travelling along the x-axis ($dy = 0$) and the other travelling along the y-axis ($dx = 0$), Equation 1.9 becomes:

$$(1 + h_+)dx^2 - cdt^2 = 0 \tag{1.10}$$

and

$$(1 - h_+)dy^2 - cdt^2 = 0 \tag{1.11}$$

which can be easily rearranged to show the differential behaviour in orthogonal axes by:

$$\frac{dx}{dt} = \frac{c}{\sqrt{1 + h_+}} \tag{1.12}$$

and

$$\frac{dy}{dt} = \frac{c}{\sqrt{1 - h_+}}. \tag{1.13}$$

When considering the length of the two orthogonal arms of an interferometer when there is no gravitational radiation present, the optical path length for each axis can be defined by:

$$l = c\tau, \tag{1.14}$$

where τ is the time light takes to travel the length of the arm. However, in the presence of gravitational radiation, using Equations 1.12 and 1.13 we obtain

$$l_{GW_x} = \int_0^\tau \frac{dx}{dt}\,dt = c\tau + \frac{c}{2}\int_0^\tau h_+(t)\,dt \tag{1.15}$$

and

$$l_{GW_y} = \int_0^\tau \frac{dy}{dt}\,dt = c\tau - \frac{c}{2}\int_0^\tau h_+(t)\,dt \tag{1.16}$$

by expanding to first order. Therefore the presence of h_+ polarised gravitational radiation will cause a change in the optical path lengths, given by

$$dl_x = l_{GW_x} - l = \frac{h_+}{2}c\tau \tag{1.17}$$

and

$$dl_y = l_{GW_y} - l = \frac{-h_+}{2} c\tau. \tag{1.18}$$

Thus, with a slight rearrangement and substitution using Equation 1.14 we obtain

$$\frac{dl_x}{l} = \frac{h_+}{2} \tag{1.19}$$

and

$$\frac{dl_y}{l} = -\frac{h_+}{2}. \tag{1.20}$$

This result highlights the differential nature of a passing gravitational wave and its effect on the orthogonal arms of a laser interferometer. It can be seen that the dimensionless strain amplitude of this polarisation is $h = h_+$. Figure 1.1 indicates how the two polarisations of a gravitational wave would affect a ring of freely suspended test particles. It is worth noting that unlike electromagnetic wave polarisation states, which are rotated by 90^0, the two gravitational wave states are instead manifest at 45^0.

1.3 Sources of Gravitational Waves

Before detailing the various sources of gravitational waves it is important to recognise the fundamental limits imposed on any ground-based detector. Seismic activity on the surface of the Earth, and the subsequent gravitational coupling to the detector, sets a lower limit of around $1\,\text{Hz}$ for which detectors can be sensitive. At frequencies above about $10\,\text{kHz}$ it is photodetector shot noise that sets an upper limit for laser interferometers. It is the band between these limits in which ground-based detectors are sensitive. However, the proposed Laser Interferometer Space Antenna (LISA), which is due to launch sometime around 2020, will be capable of observing gravitational waves at frequencies
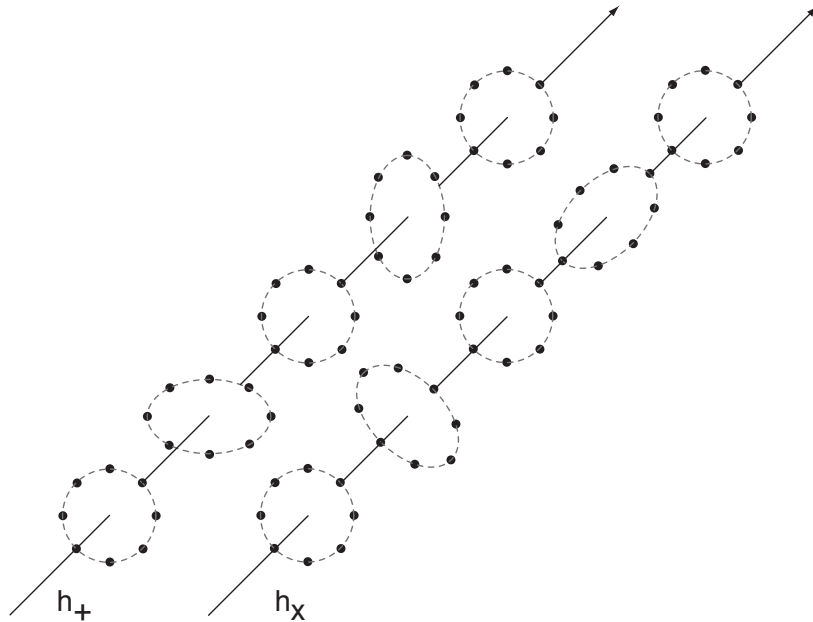
Figure 1.1: *Illustration of the effect that a gravitational wave, which is propagating along the direction of the arrow, will have on a ring of freely suspended test particles over time.*

of around $0.03\,\text{mHz}$ to $0.1\,\text{Hz}$ and will compliment the existing network of ground-based gravitational wave observatories.

Following other proposed physics experiments on Earth, such as a neutrino factory intended to study the fundamental properties of these weakly interacting particles, one might propose building a source of gravitational waves in the aim to then detect them. However, it can be shown that such experiments would yield levels of gravitational radiation with an amplitude of $h = 1 \times 10^{-43}$ [5]. It is understood that this is about 20 orders of magnitude weaker than the level of amplitude humans will realistically be able to detect. We therefore turn our attention to astrophysical sources that might generate strong enough levels of radiation that could be detected here on Earth, and of these there are a great many.

1.3.1 Burst Sources

Burst sources, as the name suggests, are those that emit gravitational radiation for only a brief period. They happen and very quickly disappear so only strong enough sources stand a chance to ever be detected with confidence. Typical candidates include astronomical events such as supernova explosions and coalescing binary systems.

Supernovae

A supernova explosion occurs when a stellar object very quickly ejects a considerable proportion of its mass, normally resulting in a remnant compact object. Throughout this process, which can last between a few milliseconds and a few minutes, the star becomes extremely bright, sometimes outshining their host galaxy and can often be observed by the human eye. There are two types of supernovae, which are defined by the expected trigger processes. Type I are believed to occur when a white dwarf star has accreted enough mass from a companion star, or merged, causing the stellar core to exceed the Chandrasekhar limit ($M_{ch} \simeq 1.38 M_{\odot} \simeq 3 \times 10^{30}$ kg). The white dwarf can no longer prevent gravitational collapse and explodes. If the core collapse is non-symmetrical, due to inherent orbital angular momentum, then gravitational radiation can be emitted.

Type II supernovae are the result of stars that are at least nine solar masses and have undergone a complex sequence of fusion processes within the core and outer layers. The nuclear fusion process will eventually reach a final stage with the production of an Iron-Nickel core, when it is no longer capable of generating energy to maintain hydrostatic equilibrium. This results in core-collapse with the formation of neutron stars and stellar mass black holes.

According to [3] the gravitational wave amplitude expected from a supernovae is

$$h = 5 \times 10^{-22} \left(\frac{E}{10^{-3} M_\odot c^2}\right) \left(\frac{15\text{Mpc}}{r}\right) \left(\frac{1\text{kHz}}{f}\right) \left(\frac{1\text{ms}}{\tau}\right)^{1/2} \qquad (1.21)$$

where E is the total energy radiated, f is the frequency of the gravitational signal, τ is the time taken for the collapse to occur and r is the distance to source.

The event rate for Type I and II supernovae, out to the Virgo cluster (at a distance of about 50 million light years $\simeq$ 15Mpc), has been estimated as a few per year.

1.3.2 Coalescing Compact Binary Systems

A binary star system is one that contains two stars orbiting around their common centre of mass. When considering compact binary systems there can be various combinations such as neutron star/neutron star (NS/NS), neutron star/black hole (NS/BH), and black hole/black hole (BH/BH). As these binary systems evolve they lose energy, through the production of gravitational waves, which eventually leads to them merging. Towards the final stage of coalescence, the orbital frequency and the gravitational wave amplitude will increase with a characteristic 'chirp', leaving a remnant black hole, most likely. These signals should be observable by ground based detectors since the amplitude has been determined [3] using the approximation

$$h = 1 \times 10^{-23} \left(\frac{100\text{Mpc}}{r}\right) \left(\frac{M_b}{1.2 M_\odot}\right)^{5/3} \left(\frac{f}{200\text{Hz}}\right)^{2/3}, \qquad (1.22)$$

where $M_b = \frac{(M_1 M_2)^{3/5}}{(M_1 + M_2)^{1/5}}$ is the mass parameter of the binary system with M_1 and M_2 being the masses of the stellar objects.

Estimates of the event rates of coalescing neutron stars [6, 7] are based on extrapolations from observed binary systems in the Milky Way, which yields a rate of $100 \, \mathrm{Myr}^{-1}$. Based on data from some of the current ground based detectors during the LIGO S5 and Virgo VSR2 science runs, (see Chapter 2) this translates into a possible detection rate of 0.02 per year. Whilst projections for the advanced detectors (the Advanced LIGO – Virgo network, see Chapter 2) suggest the event rate will increase to around 40 events per year [8].

1.3.3 Continuous Wave Sources

A continuous wave source is one which emits an almost sinusoidal gravitational wave signal for a relatively long duration. Since these signals are present for extended periods of time, it means that any monitoring of the source can benefit from improved signal-to-noise ratio. Therefore, the detectors could be sensitive to signals intrinsically weaker than other burst sources.

Binary Systems

Binary systems, well before becoming compact binaries and merging, will inspiral due to the loss of energy by way of gravitational radiation. Experimental observations of this behaviour were reported by Hulse and Taylor [9, 10] after monitoring the binary pulsar PSR $1913 + 16$. They found that the orbital period of the system decayed at $76.5 \mu s$ each year with the semi-major axis decreasing by $3.5 \, \mathrm{m}$ each year, in precise agreement with a decay model that is based on Einstein's General Theory of Relativity. Hulse and Taylor's work was awarded the Nobel Prize for Physics in 1993 and has become the first indirect evidence for the existence of gravitational waves.

It is possible to approximate the gravitational wave amplitude, h, for two stars in a binary system separated by R and of equal mass m (see [11]) using the equation

$$h = \frac{(GM)^{5/3}\Omega^{2/3}}{c^4 r}, \tag{1.23}$$

where G is the universal gravitational constant ($6.67 \times 10^{-11}\text{m}^3\text{kg}^{-1}\text{s}^{-2}$), M represents the combined mass ($M = 2m$), Ω is the angular frequency, and r is the distance from Earth. From this equation, it can be determined that the gravitational wave amplitude of the binary pulsar PSR1913 + 16 should be approximately $h = 4 \times 10^{-23}$, which would be detectable with the current sensitivity, however the frequency of this radiation is around $f = 70\mu$Hz. Unfortunately, signals of this frequency are way out of band for ground based detectors, and even for the space-based gravitational detector (LISA). We therefore turn our attention to more realistically detectable sources.

Neutron Stars

Neutron stars are thought to be a very strong candidate for the emission of high frequency continuous gravitational radiation. These compact stellar objects are extremely dense ($8 - 25\text{M}_\odot$) and since their discovery in 1967 by Hewish and Bell [12], almost 2000 have been detected at the time of writing. However, recent estimates suggest there could be as many as $200\,000$ in the Milky Way alone [13], meaning there is an abundance of possible sources.

Pulsars are highly magnetised rotating neutron stars, which emit beams of electromagnetic radiation from their magnetic poles. It is possible for the magnetic axis of the pulsar to be inclined towards Earth's line of sight, and if the magnetic poles and the rotational axis are not co-aligned, then a periodic pulse of radiation can be seen, commonly called the 'light house effect'.

Gravitational radiation will only be emitted from neutron stars and pulsars that have some degree of asymmetry. The common term used to define the amount of asymmetry is the equatorial ellipticity ϵ. The gravitational wave amplitude emitted from a pulsar is given by [14]

$$h = 6 \times 10^{-25} \left(\frac{f_{rot}}{500\text{Hz}} \right)^2 \left(\frac{1\text{kpc}}{r} \right) \left(\frac{\epsilon}{10^{-6}} \right), \qquad (1.24)$$

where f_{rot} is the rotational frequency of the pulsar, and r is the distance from Earth. The frequency of gravitational radiation emitted from pulsars occurs at twice the spin frequency and covers a relatively wide range of around $0.1\text{Hz} - 1\text{kHz}$.

1.3.4 Stochastic Sources

There is believed to be a cosmic background of gravitational radiation, analogous to the cosmic microwave background radiation. The stochastic background is expected to be composed of all the gravitational radiation sources highlighted previously along with remnant radiation from the big bang itself. Unlike electromagnetic radiation which is only visible in the transparent Universe (approximately $300\,000$ years after the big bang), gravitational radiation could still permeate through a primordial dense plasma, due to its weakly interacting nature. Detecting this background radiation could potentially lead to a much fuller understanding of the physics in extreme conditions and the origins of the Universe.

The gravitational wave amplitude for the stochastic background has been estimated to be [15]

$$h = 2.4 \times 10^{-25} \left(\frac{f}{100\text{Hz}} \right)^{-\frac{3}{2}} \left(\frac{B}{2\text{Hz}} \right)^{\frac{1}{2}} \left(\frac{\Omega_{GW}}{10^{-8}} \right)^{\frac{1}{2}} \left(\frac{H_0}{75\text{kms}^{-1}\text{Mpc}^{-1}} \right), \quad (1.25)$$

where B is the bandwidth over the frequency f, Ω_{GW} is the energy density per logarithmic frequency interval required to close the universe and H_0 is the present value of the Hubble constant.

Chapter 2

Laser Interferometry for Gravitational Wave Detection

In the previous chapter, we mentioned briefly the use of laser interferometers for gravitational wave detection to understand the types of sources that mainly ground-based detectors are optimised for. This chapter will now detail the fundamentals behind the various types of interferometer topologies that make up the current network and will also provide an overview of the technology implemented.

2.1 Michelson Interferometer

The Michelson interferometer is the fundamental interferometric configuration designed by Albert Michelson in the late 19th century. It has become the foundation for almost all interferometric solutions to gravitational wave detection. The Michelson topology is illustrated in Figure 2.1. Before we begin to exam-
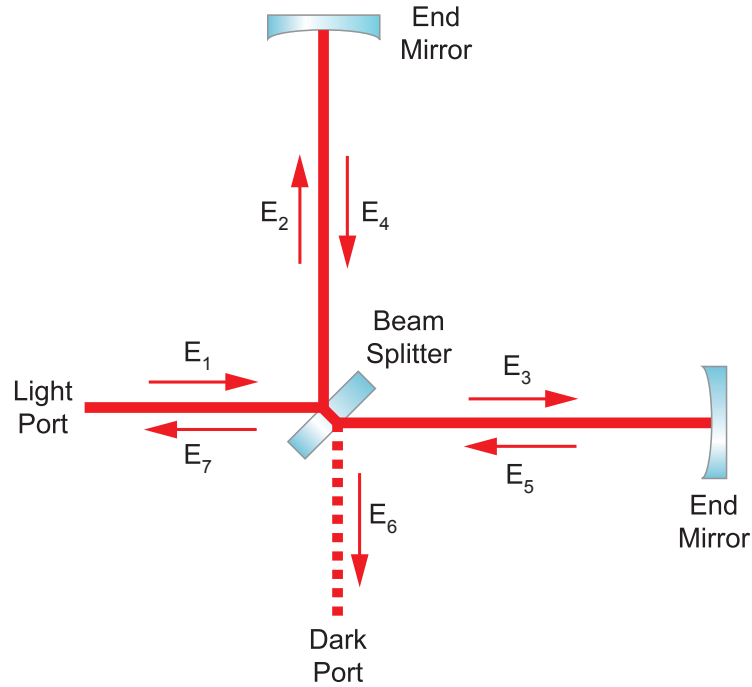
Figure 2.1: *Basic layout for a Michelson interferometer. There is one input port for a coherent light field (***E**$_1$*) and two possible output ports for light exiting the system (***E**$_6$* and ***E**$_7$*). The input light splits (***E**$_2$* and ***E**$_3$*) upon incidence with the beam splitter, travelling down two orthogonal 'arms'. The light fields (***E**$_4$* and ***E**$_5$*) then return to the beam splitter after reflection with each of the end mirrors.*

ine the interaction of the light fields within this interferometric topology and others that follow, it is important to first describe the convention that will herein be used. Any optical component, such as mirrors and beam splitters, can be described by a complex valued $n \times n$ matrix $\mathbf{S_n}$, where n input ports are represented by a vector $\mathbf{a}$, and the output ports are represented by the vector $\mathbf{b}$. Both $\mathbf{a}$ and $\mathbf{b}$ have components a_i and b_i respectively, which are complex amplitudes at the ith port. The coupling of input and output ports
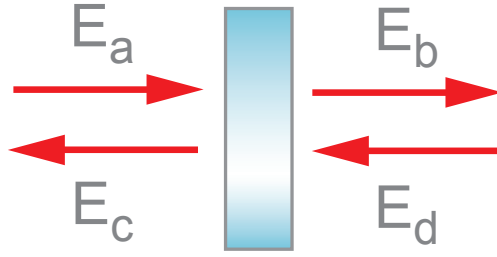
Figure 2.2: *Simple schematic of the input fields ($\mathbf{E}_a$ and $\mathbf{E}_d$) and output fields ($\mathbf{E}_b$ and $\mathbf{E}_c$) upon interaction with a mirror.*

for a mirror or beam splitter is then given by

$$\mathbf{b} = \mathbf{S_{2p}} \cdot \mathbf{a}, \tag{2.1}$$

such that the field interactions at a mirror, as shown in Figure 2.2, can be described by

$$\begin{pmatrix} \mathbf{E}_b \\ \mathbf{E}_c \end{pmatrix} = \begin{pmatrix} i\tau & \rho \\ \rho & i\tau \end{pmatrix} \cdot \begin{pmatrix} \mathbf{E}_a \\ \mathbf{E}_d \end{pmatrix}, \tag{2.2}$$

where ρ and τ are the amplitude reflectivity and transmitivity of the mirror respectively. The input light field entering the Michelson interferometer at time t can be represented by the scalar expression

$$\mathbf{E}_1 = \mathbf{E}_0 e^{i\omega t}, \tag{2.3}$$

where $\mathbf{E}_0$ is the amplitude of the field and ω is the angular frequency of the light. Here we assume the beam splitter in Figure 2.1 is 50:50, meaning that 50% of the light is reflected along one arm, whilst 50% is transmitted along the other arm, and we define

$$\mathbf{E}_2 = \rho \mathbf{E}_1, \tag{2.4}$$

and

$$\mathbf{E}_3 = i\tau \mathbf{E}_1. \tag{2.5}$$

These two light beams then travel down each arm and are reflected by the end mirrors, arriving back at the beam splitter. Any difference in length between the two arms Δl will result in the time taken to traverse the extra length $t = 2\Delta l/c$, so that the angular frequency of the returning light fields is out of phase by an amount

$$\phi = \omega t = \frac{2\pi c}{\lambda}\frac{2\Delta l}{c} = \frac{4\pi\Delta l}{\lambda}. \tag{2.6}$$

The returning light fields, just before the beam splitter as depicted in Figure 2.1, are then given by

$$\mathbf{E}_4 = \rho\mathbf{E}_1 e^{i\frac{\phi}{2}}, \tag{2.7}$$

and

$$\mathbf{E}_5 = i\tau\mathbf{E}_1 e^{-i\frac{\phi}{2}}. \tag{2.8}$$

At the beam splitter these two beams recombine to produce a single light field exiting the 'dark port', given by

$$\mathbf{E}_6 = i\tau\mathbf{E}_4 + \rho\mathbf{E}_5, \tag{2.9}$$

and another light field returning to the 'light port', described by the expression

$$\mathbf{E}_7 = \rho\mathbf{E}_4 + i\tau\mathbf{E}_5. \tag{2.10}$$

Both light fields exiting the Michelson interferometer can be detected on photodetectors in order to obtain information about the lengths of the orthogonal arms. Photodetectors produce a current based on the amount of power in the beam that is incident. Therefore, they are sensitive to the absolute square of the amplitude as shown by

$$P \propto |\mathbf{E}|^2 = \mathbf{E}.\mathbf{E}^*. \tag{2.11}$$

Applying this to the output fields given by Equation 2.9 and 2.10 it is then possible to obtain the relative power at each port dependent on the phase difference between the two returning light fields:

$$\frac{P_6}{P_0} = 2(\rho\tau)^2 + 2(\rho\tau)^2\cos\phi, \tag{2.12}$$

and

$$\frac{P_7}{P_0} = (\rho)^4 + (\tau)^4 - 2(\rho\tau)^2 \cos\phi. \tag{2.13}$$

For the purpose of gravitational wave detection, the interferometer is held at the operating point (as will be discussed later), which means that the dark port is maintained at the point of destructive interference and therefore minimum light exiting through this path. Meanwhile most of the light is returning along the input path to the light port, meaning that the interferometer is effectively a mirror. To achieve this operating point requires the phase difference, as indicated by Equation 2.12 and 2.13, between each arm $\phi = \pi$, i.e. a balanced interferometer. The presence of a gravitational wave will thereby act to change the relative phase between the returning light fields and result in a portion of light exiting the dark port to be subsequently detected on a photodetector.

The above experimental apparatus and method for detecting gravitational waves is fundamental to all current laser interferometric gravitational wave detectors, however, several enhancements have been made in order to improve the detector sensitivity as will now be discussed.

2.2 Fabry-Pérot Michelson Interferometer

The evolution from a basic Michelson interferometer to the current and future states of these detectors all have the same goal, which is to maximise the number of photons in the system and store them for as long as feasibly possible before detection. One technique is to create off axis paths for light beams to travel down the arms of the interferometer, known as 'delay lines', as indicated by Figure 2.3. It's worth noting that the largest detectors have kilometre scale arm lengths, which is much smaller than the wavelength of gravitational waves expected from typical astronomical candidates. Therefore by folding the arms
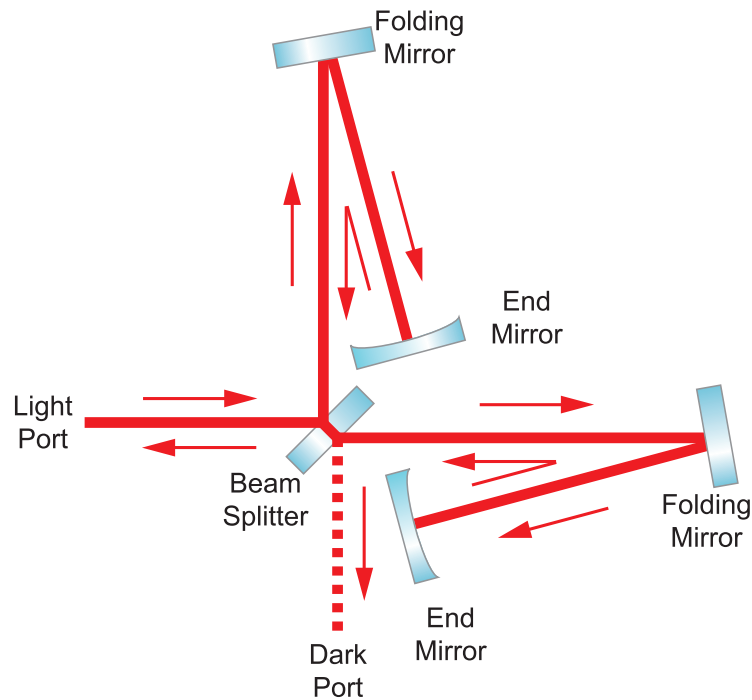
Figure 2.3: *The simplest delay line Michelson interferometer. The effective arm length is doubled with the folding mirror and end mirror positioned off-axis to obtain one reflection. Other off-axis positions of the mirrors can result in multiple reflections of light within the arms.*

until the effective length reaches half the gravitational wavelength, the phase shift between the returning light from each arm will be maximised, and this in turn will give rise to a larger detected signal exiting the dark port.

Another technique that is often adopted and follows the same principle as delay line interferometers is an additional partially transmitting mirror at the inner position of each arm. This results in the arms of the interferometer forming optical cavities, called Fabry-Pérot cavities (see Figure 2.4), named after a spectroscopy standard by Fabry and Pérot [16]. If the length of the arm is tuned, such that exactly an integral number of half wavelengths of laser light are stored within the cavity, then the cavity is on resonance. Maintaining
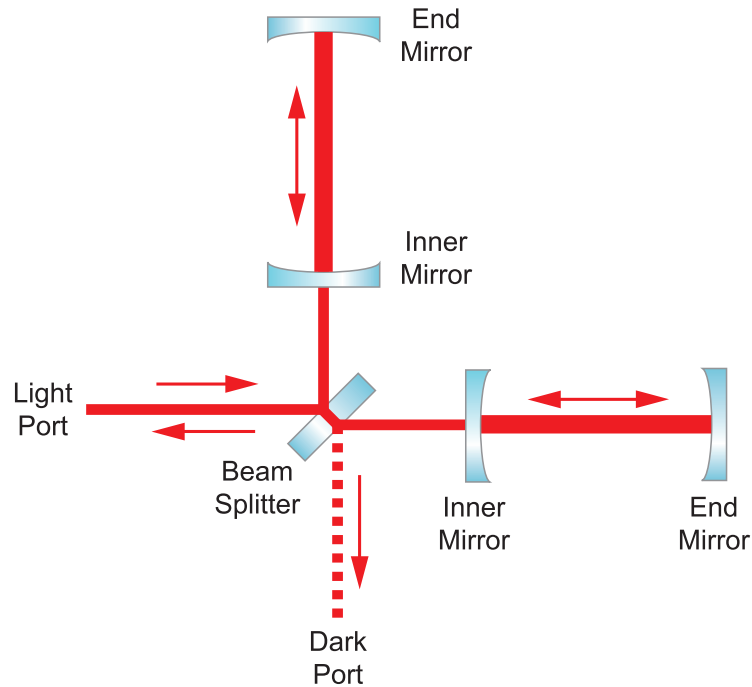
Figure 2.4: *Schematic of the Fabry-Pérot Michelson Interferometer.*

the resonant condition means that incoming light is superimposed onto the light inside the cavity many times, maximising the overall energy, which will eventually leak out towards the beam splitter after a certain amount of time, known as the cavity storage time τ_s. The storage time of a cavity is defined by the properties of the cavity mirrors and their separation. It is possible to measure the storage time of a cavity experimentally by removing the light source and monitoring the time taken for the light level in the cavity to fall to $1/e$ from the initial cavity level. Alternatively, to understand the properties of the cavity it is also useful to measure the cavity linewidth, which is inversely proportional to storage time and also related to the mirror properties.

2.3   Power Recycling

As previously discussed, the use of resonant optical cavities can be used to enhance the interferometer sensitivity to differential changes in arm length, but we have so far ignored the light that eventually does leak back to the light port. In section 2.1 it was mentioned that the interferometer can be essentially treated like a mirror. It is therefore possible to form another optical cavity with the interferometer itself by placing an additional partially transmitting mirror at the light port. This technique is known as power recycling because it acts to re-use otherwise wasted light by feeding it back into the system, as shown by Figure 2.5. With this technology, a higher level of power and therefore higher number of photons are incident on the two arms of the interferometer, which improves the output signal at the dark port.

2.4   Signal Recycling

Signal recycling is another complimentary technique to improve the detector sensitivity, in that while power recycling acts to maximise the power in the arms, signal recycling controls the resonance of the signal fields. The basic principle is to add another partially transmitting mirror at the dark port as shown by Figure 2.6. When the beam splitter is in the right position for power recycling (to see the common mode of the arms), it also allows the signal recycling mirror to see the differential mode, hence forming what is effectively a cavity for the light in that mode, directed to the signal recycling mirror by the beam splitter. Since the signal recycling cavity contains the signal sidebands there is also the opportunity to tune the position of the mirror in a way that enhances a specific band of resonant frequencies. The enhanced
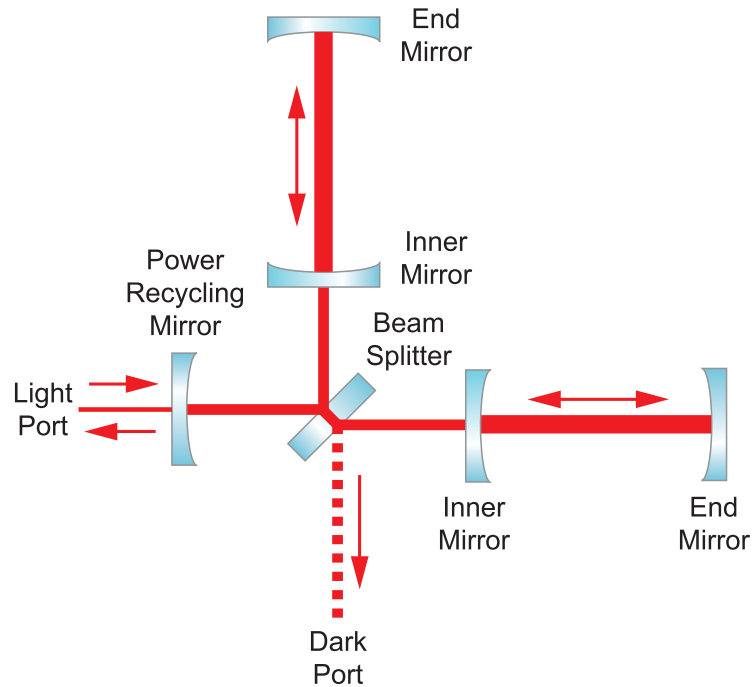
Figure 2.5: *Schematic of the Fabry-Pérot Michelson Interferometer with the addition of a power recycling mirror at the light port. The injected power is of the order $1 - 200$W, the power inside the recycling cavity is of order* kW *and the power inside the arm cavities is ~ 10kW to 1MW in current or planned instruments.*

sensitivity can be achieved in three particular modes of operation; *broadband signal recycling, resonant sideband extraction* and *detuned signal recycling*. In order to describe the basic principles behind each of these operating conditions it helps to consider the light fields in the frequency domain. The primary laser light frequency injected into the interferometer is usually termed the 'carrier' frequency, and to this various modulation radio frequencies are added, also known as 'control sidebands', in order to extract information about the numerous cavity lengths.

Broadband Signal Recycling

It has already been mentioned that the carrier light is resonant inside the arm cavities to enhance the detector sensitivity. In broadband recycling the position of the signal recycling mirror is maintained at a location such that the carrier frequency is *anti-resonant* inside the cavity which is formed with the inner mirrors of the interferometer arms. This technique increases the effective reflectivity of the inner mirrors and thereby leads to an increased storage time for the signal sidebands, i.e. allows more signal sideband amplitude to be accumulated. An increase in storage time however leads to a smaller bandwidth of operation.

Resonant Sideband Extraction

Conversely, in resonant sideband extraction, the position of the recycling mirror is held at a location where the carrier frequency is *resonant* inside the recycling cavity. This actually reduces the effective reflectivity of the arm cavities, which reduces the time spent by the photons inside the system, however this also increases the bandwidth of the detector. Therefore, by implementing very high finesse arm cavities with ultra low loss, resonant sideband extraction can be used to build a very broadband and sensitive detector.

Detuned Signal Recycling

This mode of operation relies on detuning the signal recycling mirror away from the position where the carrier is resonant and consequently into a position where the optical resonance occurs at a frequency which can be even higher than the linewidth of the arm cavities. The position of the signal recycling
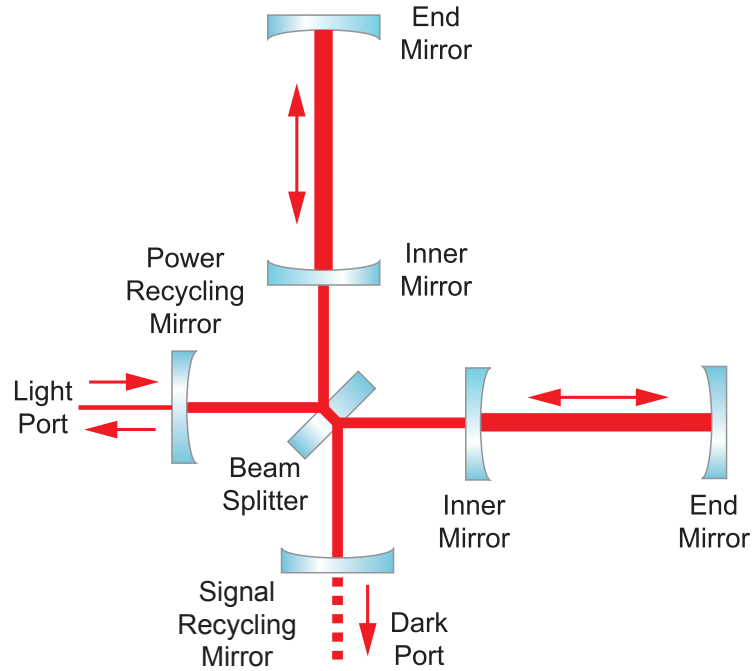
Figure 2.6: *Schematic of the Fabry-Pérot Michelson Interferometer with power recycling and the addition of a signal recycling mirror at the dark port.*

mirror can be tuned independently from the arm cavities and therefore the peak in detector sensitivity can be optimised for different frequencies of radiation at different times.

In addition to the well known optical resonance, there is a secondary resonance which has been observed in signal recycled interferometers [17] [18]. This other resonance is in fact optomechanical in nature due to the classical coupling of the light field with the antisymmetric mode of the mirrors. When the signal recycling mirror is maintained in a detuned mode of operation, the phase modulated sidebands induced by a gravitational wave will be partially converted into amplitude modulations that beat with the carrier light. This light field induces a motion-dependent force acting back onto the arm cavity mirrors [19]. More on the optomechanical nature of detuned cavities will be

covered in chapter 4.

2.5 Length Sensing and Control

In order to hold the interferometer at the desired operating point requires knowing the relative lengths between each of the component mirrors and controlling their length by way of electromagnetic feedback. Each of the mirrors, along with the feedback mechanism, must also be free to move, which is conventionally achieved through the use of multistage pendulums as indicated by Figures 2.7. This also very effectively isolates the mirrors from seismic activity above the pendulum resonant frequency. The electromagnetic feedback is achieved by using an array of fixed magnets and copper wound coils that sit close together as indicated by Figure 2.8. By sending continuous current signals through the copper coils and generating magnetic fields, the fixed magnets will experience a force, which in turn will control the separation between the test mass and the reaction mass. The current signals, usually termed control signals, are derived from the interferometer output signals, which indicate the relative length between each component mirror. The arrangement of sidebands that are added to the carrier light are chosen to optimise the ability to observe small length changes and the whole process is achieved through modulation and demodulation.

2.6 Modulation and Demodulation

As interferometric systems become more complex, the number of optical components increases, whose relative separations must be maintained at the correct
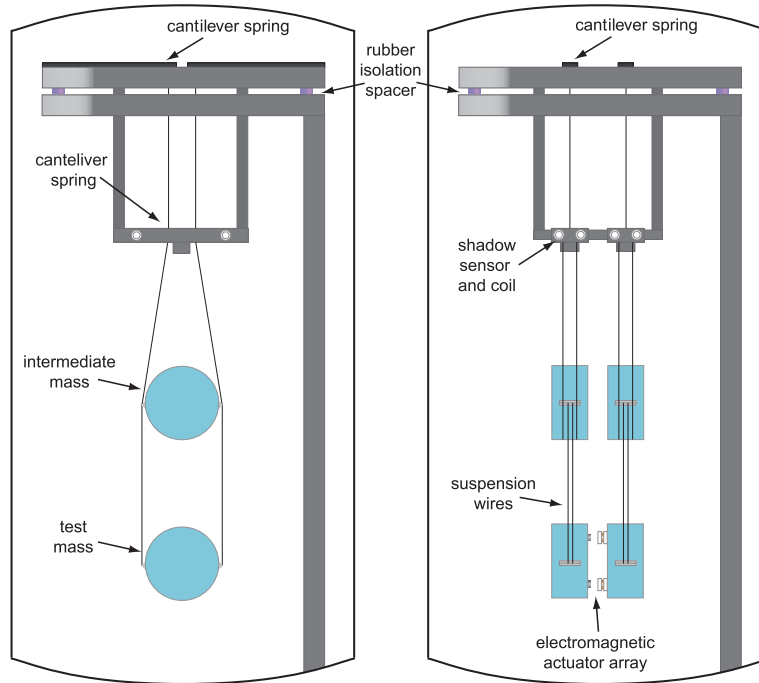
Figure 2.7: *Schematic of a triple-suspended test mass indicating the interme-diate and upper mass stages. A reaction chain is also shown to illustrate the feedback mechanism to the free suspension stages.*

operating point. The technique used to monitor the cavity length relies upon modulation to add frequency sidebands to carrier light. When propagated inside a cavity the phase of the carrier component moves relative to non-resonant sideband fields, resulting in a change to the relative strength of the beat frequencies. Monitoring the fields exiting the cavity on photodetectors, and demodulating at the modulation/beat frequency, reveals an antisymmet-ric error signal. This length sensitive signal can then be applied with suitable negative feedback through electromagnetic actuators to control the cavity mir-ror positions. Modulation of the carrier light field can be achieved with two different techniques; phase modulation and amplitude modulation.
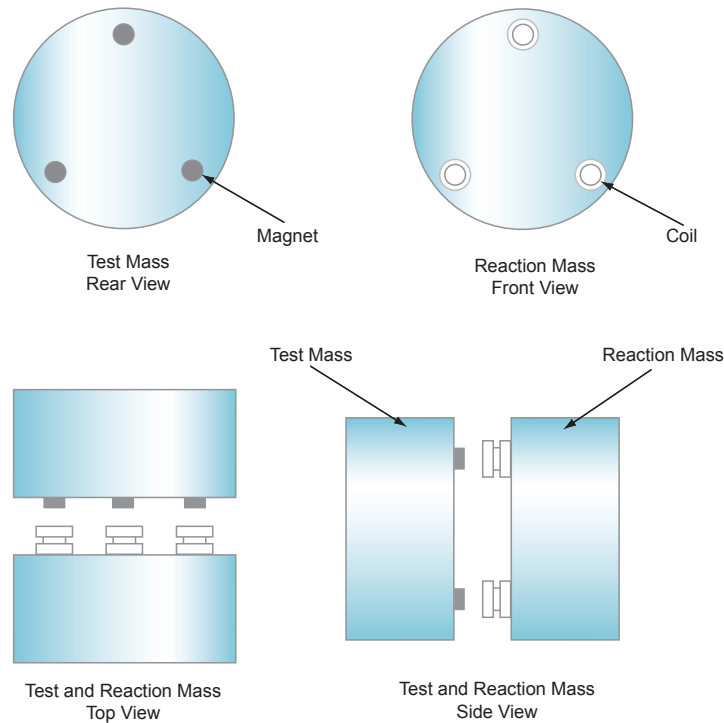
Figure 2.8: *Illustration of test masses and reaction masses that are located at the bottom of a three or four stage pendulum. The magnets are rare earth metals, usually Nickel plated Neodymium Iron Boron (Nd:Fe:B), used because of their high magnetic properties. The coils are constructed from vacuum compatible material formas (in our system PEEK) wound with typically $\sim 100 - 1000$ turns of insulated copper wire. The schematic also indicates the relative positions of the coils and magnets used for electromagnetic longitudinal feedback in the Glasgow prototype.*

Phase Modulation

As the name suggests, phase modulation changes the phase of the light field, and the amount of phase change is dependent on the strength of the modulation, known as the modulation index. To begin a mathematical analysis of

this technique we must first start with an unmodulated light field, given by

$$E = E_0 e^{i\omega_0 t}.$$ (2.14)

Applying phase modulation, with angular frequency ω_m and modulation index of m, onto this field yields

$$E_{PM} = E_0 e^{i\omega_0 t} e^{im \cos \omega_m t}.$$ (2.15)

By expanding Equation 2.15 to first order using standard identities gives

$$E_{PM} = E_0 e^{i\omega_0 t} \sum_{k=-\infty}^{\infty} i^k J_k(m) e^{ik\omega_m t}$$ (2.16)

$$\approx E_0 e^{i\omega_0 t} \left(J_0(m) + iJ_1(m) e^{i\omega_m t} + iJ_1(m) e^{-i\omega_m t} \right),$$ (2.17)

where $J_k(m)$ are Bessel functions of the first kind of order k and defined by [20]

$$J_k(m) = \sum_{j=0}^{\infty} \frac{-1^j}{j!(j+k)!} \left(\frac{m}{2}\right)^{k+2j}$$ (2.18)

and

$$J_{-k}(m) = (-1)^k J_k(m).$$ (2.19)

Here we consider only the first order expansion as we are concerned only with the first order sidebands and not the higher harmonics.

Amplitude Modulation

Amplitude modulation is a periodic modulation of the amplitude of a light field. Starting with an unmodulated light field, as before, and then applying amplitude modulation gives

$$E_{AM} = E_0 e^{i\omega_0 t}(1 + m \cos \omega_m t),$$ (2.20)

with a modulation index $m \leq 1$. This can be expressed by exponentials as

$$E_{AM} = E_0 e^{i\omega_0 t}(1 + \frac{m}{2} e^{i\omega_m t} + \frac{m}{2} e^{-i\omega_m t}),$$ (2.21)

where the modulation sidebands are at $\omega_0 \pm \omega_m$.

Demodulation

Once the light has been modulated appropriately, it is then injected into the interferometer to propagate. If there is an arm length difference or deliberate offset to allow modulation sidebands to reach the output, this is known as Schnupp Modulation [21]. The modulated light will then exit the interferometer through the dark port or the light port and be subsequently detected on photodetectors. As discussed briefly earlier, the photodetectors used are sensitive to power fluctuations which are related to the amplitude squared as described by Equation 2.11. The power that is detected by the photodetector now contains not only the DC signal that represents the carrier light and modulation sidebands, but it also contains a signal at the modulation frequency ω_m (generated by the beat between the carrier frequency and the modulation sidebands) and also a signal at twice the modulation frequency, $2\omega_m$, (generated by the upper sideband beating with the lower sideband). The detected power can therefore be written as

$$P_{DET} = P_0 + P_{\omega_m} + P_{2\omega_m}. \tag{2.22}$$

By detecting the light it is therefore possible to monitor the behaviour of the interferometer. The information about the lengths of the interferometer arms is contained in P_{ω_m}, but in order to extract this information, we must first manipulate the signal in a procedure called demodulation. By beating P_{DET} with another signal at the same modulation frequency ω_m, known as a local oscillator, we shift all of the frequency components and obtain a DC signal containing P_{ω_m} [1]. The phase of the local oscillator can be adjusted to either in-phase with the ω_m component, which would maximise the demodulated signal, or adjusted to quadrature-phase, thereby minimising the signal.

---

[1] Note that with detuned signal recycling it is more complicated as one sideband is larger than the other resulting in each quadrature having different signals.

2.7 Sources of Noise

This section will provide a description of the limitations to ground-based detectors that arise from various possible sources of noise. There are two groups of noise sources called *technical noise* and *fundamental noise*. Technical noise is a result of the quality of technology used in interferometry such as the laser light source, thermal noise associated with materials, seismic noise coupling from the isolation system, and any actuation or damping unit that is employed. Whereas fundamental noise is related to the theoretical limitations imposed on the measurement process by the quantum nature of the Universe. This *quantum noise* primarily consists of two components in regards to interferometers: photon shot noise and radiation pressure noise. The remainder of this section will focus on highlighting some of these sources of noise in order to provide a better understanding of the limits to the current network and future generations of ground-based detectors.

2.7.1 Seismic Noise

The external disturbances to the local environment of any ground-based detector is called seismic noise. It can couple into the detector through the mirror mountings or the injected laser light. If the mirrors are directly mounted onto an optical bench, seismic noise will directly couple into the light that transmits or reflects. However, if the mirrors are suspended from a single pendulum stage, then seismic noise at a frequency f will be attenuated to the order $(f_p/f)^2$, above the resonant frequency of the pendulum f_p, effectively filtering out the seismic noise [22]. It is possible to further attenuate the seismic noise by cascading the number of stages which will dramatically isolate vibrations coupling into the lowest stage.

Furthermore, it is also usual to add some kind of pre-isolation to supplement the attenuation of the pendulum. One passive isolation technique that is often used is a composite rubber stack sandwiched between two layers of the supporting structure. Another passive technique to isolate the vertical components of seismic noise is to use cantilever springs, consisting of specially designed steel blades, which can also be cascaded to improve performance. There are also active isolation schemes that feed forward to minimise the motion caused by measurable disturbances.

2.7.2 Thermal Noise

Thermal energy causes internal vibrations of the mirrors and the suspensions. These vibrations can couple to the light and hence limit the sensitivity to displacement. The amplitude of the thermal vibrations is maximal at the resonant frequency of the vibration, in other words the internal modes of the mirror masses, and the pendulum modes of the suspensions. This localises thermal noise to primarily two regions: below 50Hz for the pendulum and violin modes and above several kHz for the internal modes of the mirrors.

The contribution of the pendulum mode with a resonant angular frequency ω_0 to thermal noise spectrum can be shown to be

$$x(\omega) = \left(\frac{4k_B T}{\omega M} \frac{\omega_0^2 \phi_0(\omega)}{(\omega_0^2 - \omega^2)^2 + \omega_0^4 \phi_0(\omega)^2} \right)^{\frac{1}{2}}, \tag{2.23}$$

where k_B is the Boltzmann constant, T is the temperature, ω is angular frequency, M indicates the mirror mass and $\phi_0(\omega)$ represents the mechanical loss of the resonance mode [4]. The loss of a material is inversely proportional to the quality (Q factor) of the resonance mode, therefore by selecting high Q mirror and suspension materials with inherent low mechanical loss, the thermal energy can be concentrated inside a narrow frequency band and out of the

detection band of the interferometer.

The contribution of the internal modes of the mirror with angular frequency ω_n to the thermal noise spectrum can be shown to be

$$x(\omega) = \left[\sum_n \frac{4k_B T}{\alpha_n M \omega_n^2} \frac{\phi_n(\omega)}{\omega} \right]^{\frac{1}{2}}, \qquad (2.24)$$

where $\phi_n(\omega)$ is the loss associated to mode n, and α_n represents the effective mode mass coefficient describing the coupling of that mirror mode to the mirror surface displacement [23].

2.7.3 Laser Noise

The laser itself is prone to noise which can limit the sensitivity of detectors. These noise sources shall now be summarised.

Beam Geometry Fluctuations

The laser and the associated beam conditioning optics are usually located on an optical bench. Seismic and acoustic noise can therefore couple through the optical bench onto the laser beam and disturb the beam pointing or position. These fluctuations to the beam geometry result in changes to the cavity mode matching and therefore putting light into higher order spatial modes, which can couple into the detector output signal due to deviations in optical path lengths.

Frequency Noise

Given that the principal operation of a gravitational wave detector is to measure the phase difference between the two returning light paths from the arms of the interferometer, any process that might cause a variation on the relative phase between the two beams will eventually limit the overall sensitivity. This can occur if the two arms are not of equal length and the frequency of the light fluctuates over the time time spent inside the interferometer. The spectral density for the required frequency stability can be expressed as

$$\delta x = \delta l \left(\frac{\delta f}{f} \right),$$ (2.25)

where δl is the difference between the two arm lengths, δf represents the frequency fluctuations measured in units of $\text{Hz}/\sqrt{\text{Hz}}$, and $\delta f/f$ is the fractional frequency fluctuations in the laser light [4]. This can be overcome using a stable frequency reference and feeding back to the length of the cavity or the laser frequency.

Amplitude Noise

As gravitational wave detectors are designed so that the output is held at the dark fringe position, the phtotodetector at this port must be very sensitive to fluctuations in the intensity with the passing of a gravitational wave. However, if there is a small offset in length away from optimum operating point and there are fluctuations on the amplitude of the laser light, then these can couple into the output port and limit the overall sensitivity. It can be shown [24] that the spectral density for the required amplitude stability can be expressed as

$$\delta x = \delta l \left(\frac{\delta P}{P} \right),$$ (2.26)

where δl is the length offset from the optimum operating point, and $\delta P/P$ is the fractional change in power fluctuations in the laser light.

2.7.4 Photon Shot Noise

The photons in the laser light used for interferometry are quantised, and therefore will be created and detected randomly giving rise to statistical fluctuations in a measurement, which can best described by a Poisson distribution. Therefore the photon shot noise in the signal detected will approach a normal distribution when large numbers of photons are used and hence the uncertainty in detecting N photons will improve as $\sqrt{N}$. The minimum detectable strain sensitivity for a shot noise limited interferometer [25] is given by

$$h_{min} = \sqrt{\frac{\hbar\lambda\omega_g^2\Delta f}{2\pi\epsilon P_0 c}}, \tag{2.27}$$

where P_0 is the maximum power detected at the dark port of wavelength λ, $\hbar$ is the reduced Planck constant, ω_g is the angular frequency of the gravitational wave, Δf is the measurement bandwidth, c is the speed of light in vacuum, and the photodetector quantum efficiency is ϵ. It can be seen from equation 2.27 that by increasing the laser power the level of shot noise can be improved. However, there will eventually come a point at which the increase of laser power results in radiation pressure noise becoming a limiting factor.

2.7.5 Photon Radiation Pressure Noise

The photons in the laser light incident upon the surface of the mirrors of an interferometer will impart momentum. Although the incident force attributed to a single photon is very weak, the use of high finesse optical cavities allows

the storage of huge amounts of power such that the radiation pressure force becomes a dominant effect in some of the detection band in ground-based detectors. Therefore fluctuations in the relative power build up of the interferometer arms causes differential variations to the force exerted on the mirrors and causes radiation pressure noise which couples to the output signal. For a Delay-Line interferometer of length L and with N bounces, the radiation pressure noise can be described as a strain sensitivity by [4]

$$h_{RP}(f) = \frac{N}{mf^2L}\sqrt{\frac{2\hbar P_{in}}{\pi^3 c\lambda}}, \tag{2.28}$$

where m is the mirror mass, f is the measurement frequency, P_{in} is the input power, and λ is the wavelength of the laser light. From 2.28, we note $h_{RP} \propto \frac{\sqrt{P}}{f^2}$, therefore as frequency increases the radiation pressure noise decreases, while increasing the input power results in an increase to the radiation pressure noise.

2.7.6   The Standard Quantum Limit

We have shown that as the laser power is increased, the photon shot noise decreases while radiation pressure noise increases, thus revealing a fundamental limit to the performance of interferometric gravitational wave detectors where the test masses are free to move along the direction sensed by the interferometer and the two optical noise sources are uncorrelated. Then, for any given power there exists an optimum frequency for operating the detector, which is the minimum point for the sum of both. This fundamental limit to the detector sensitivity is known as the Standard Quantum Limit (SQL) as illustrated in Figure 2.9, and corresponds to the Heisenberg Uncertainty Principle that sets a formulation to the position and momentum of the mirrors [26, 27].

If all other noise sources are isolated, it is possible to reach the SQL for a range of frequencies, by adjusting the noise distribution in each quadrature
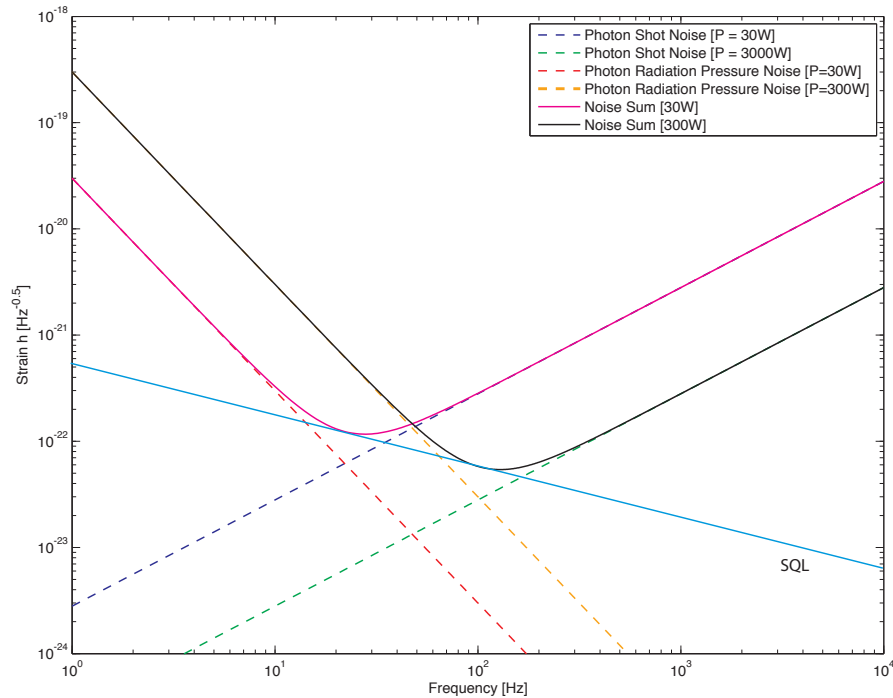
Figure 2.9: *Modelled noise curves for the radiation pressure noise, photon shot noise, and the sum for different input power levels. The SQL represents the minimum sensitivity for any given power.*

of the vacuum field. One technique to achieve this is to inject *squeezed* light into the dark port of the detector [27]. The squeezing technique is another advancement that has recently been successfully demonstrated experimentally on the GEO600 detector [28] and is expected to be implemented within other large baseline detectors, such as Advanced LIGO.

In principle, it should also be possible to not only reach the SQL, but also to overcome the fundamental limit for free masses. This is made possible by correlating phase and amplitude of the light fields in an interferometer. There are various ways by which such correlations may be introduced. One technique, where optical cavities are employed, is to induce an optomechanical resonance (see Chapter 4), whereby motions of the suspended cavity mirrors

are optically coupled. If that is achieved the masses are no longer free, and a new uncertainty limit emerges.

2.8 The Current Network and Future Detectors

The basic technology used in ground based gravitational wave detectors has been described along with the sources of noise associated to various components. It is therefore possible to investigate the types of systems that are currently operational around the world along with the respective sensitivity limits, also the planned upgrades to the detectors for the future network.

The laser interferometric gravitational-wave observatory (LIGO) is a ground-based detector at two separate sites in the USA (Livingstone, Louisiana and Hanford, Washington). LIGO has been operational since 2002 and has recently finished its sixth data run known as $S6$. Each interferometer has been built as a Fabry-Pérot Michelson interferometer with $4\,\mathrm{km}$ arm lengths and with power recycling also being implemented. All of the optical components are contained inside a vacuum with the main optics being suspended as multistage pendulums. Together they are the largest and most sensitive detectors that have yet been built with an upper sensitivity of $1 \times 10^{-23}\,\mathrm{m}/\sqrt{\mathrm{Hz}}$ at around $100\,\mathrm{Hz}$ as indicated by Figure 2.10.

At low frequencies, LIGO sensitivity is limited by suspension thermal noise caused by the losses at the top and the bottom attachments of each suspension fibre, whereas at high frequencies the detectors become limited by photon shot noise, which is the Poissonian noise in the number of photons detected.
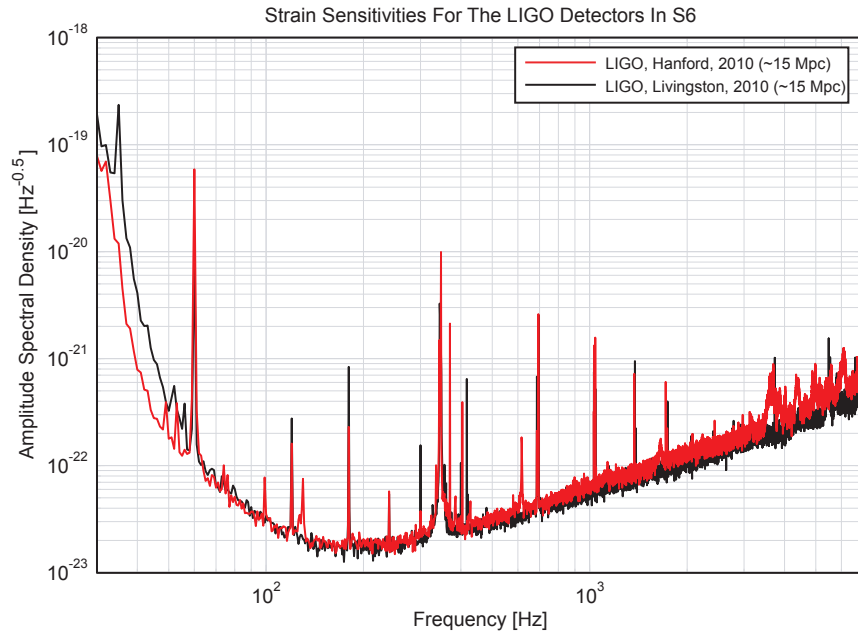
Figure 2.10: *LIGO strain sensitivity for a data run in May 2010 [29].*

The last few years have seen a huge effort around the world working towards the design, testing, construction and recently the installation of Advanced LIGO which is due to be operational in 2014. Many improvements have come from technology tested on GEO600, as will be discussed shortly, which help to lower the noise floor by an order of magnitude and hence expand the volume of space covered by ~ 1000.

The French/Italian gravitational wave detector is called Virgo, located at Cascina, Italy, and has been operational since 2007. All the optical components are contained in ultra-high vacuum environments. To increase the detector bandwidth at low frequencies the Virgo detector employs an array of super attenuators suspending some of the optical components to isolate seismic noise. The interferometer arms consist of $3\,\text{km}$ Fabry-Pérot optical cavities and the stored power is optimised using power recycling. The sensitivity limit
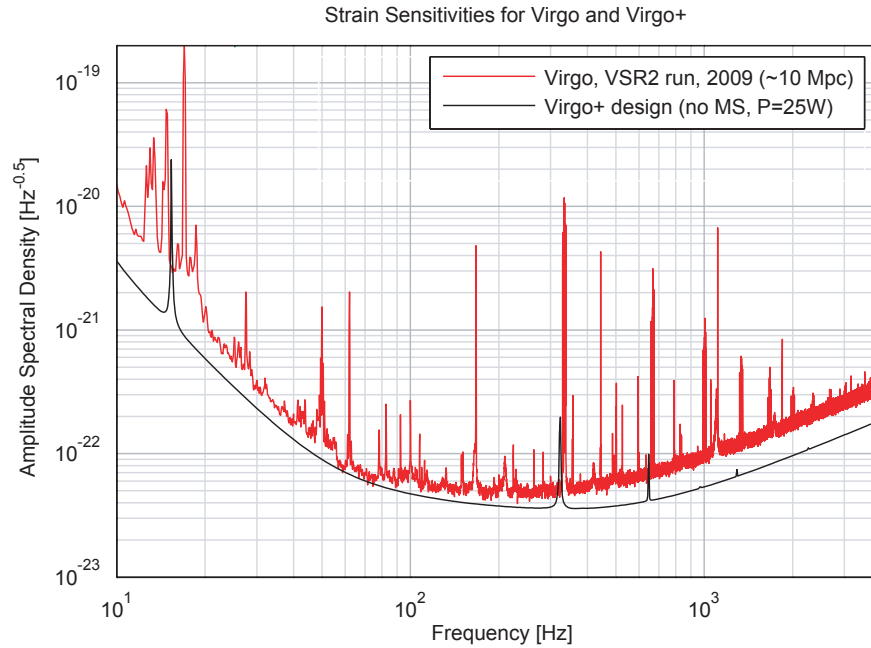
Figure 2.11: *Typical sensitivity curves for Virgo obtained during a late run in 2009, and theoretical sensitivity for Virgo+ [30].*

of the latest scientific data run VSR2 is indicated by Figure 2.11.

Similarly the Virgo detector is limited by suspension thermal noise at low frequencies and by photon shot noise at high frequencies. Over the next few years Virgo will also enter a period of planned upgrades in order to improve the overall sensitivity.

GEO600 is the joint UK/German gravitational wave detector located near Hanover, Germany, and has been operational since 2002. Unlike the LIGO and Virgo detectors it does not make use of Fabry-Pérot cavities but instead uses a delay-line topology with folded 600 m arms, giving effectively 1.2 km arm lengths. GEO600 makes use of power recycling and signal recycling, together termed dual-recycling, to maximise the stored light level. A typical sensitivity limit is provided in Figure 2.12.
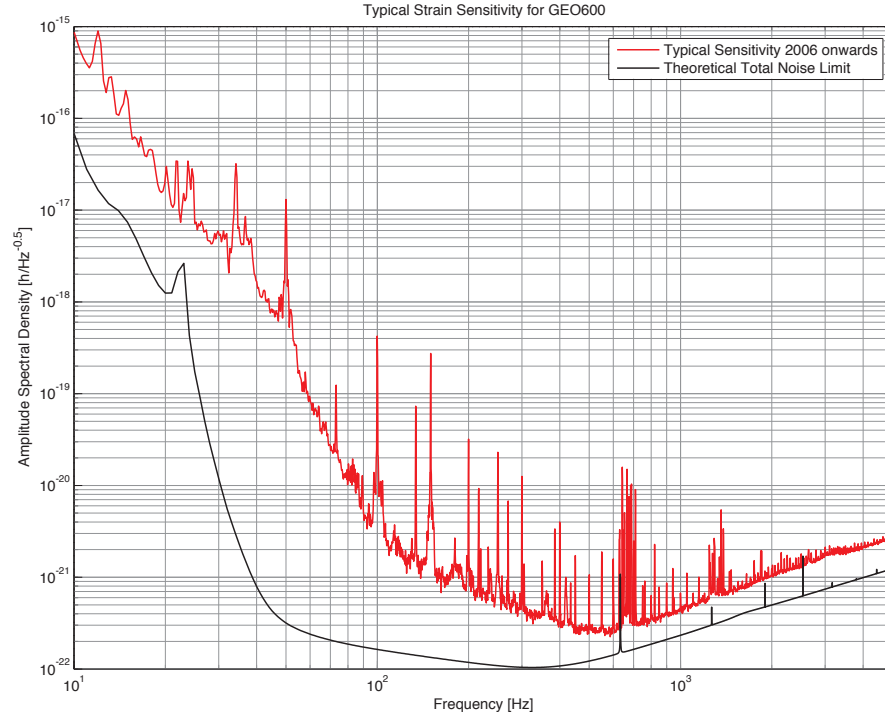
Figure 2.12: *Typical and theoretical sensitivity curves for GEO600 from* 2006 *onwards [31].*

Despite being much smaller compared to LIGO and Virgo, much of the second generation technology such as suspension design, advanced optical techniques and mirror materials have been developed and installed on GEO600 to help it achieve a higher sensitivity. This technology could then be transferred onto the larger detectors during their upgrading process. One of the advanced optical techniques recently tested on GEO600 and planned to be implemented on advanced LIGO is the squeezing of light, where it should be possible to aim for about 6 - 10 dB in sensitivity gain at frequencies where shot noise dominates without the requirement for increased input light. Other technologies for advanced LIGO from the UK/German collaboration come in the form of high power lasers and high Q suspensions for controlling the suspension thermal noise.

An even smaller scale detector called TAMA300 is the Japanese gravitational wave detector with 300m arm lengths which was one of the first large-scale detectors to achieve continuous lock at a maximum sensitivity of $1 \times 10^{-20}\,\mathrm{m}/\sqrt{\mathrm{Hz}}$ [32]. TAMA300 is essentially the prototype towards the recently approved future project called Large-scale Cryogenic Gravitational-wave Telescope (LCGT). The LCGT will be built in the Kamioka mine in Japan, implementing cryogenic mirror techniques to reduce the effects of mirror thermal noise.

Whilst LIGO and Virgo are undergoing various upgrades, GEO600 will remain operational to ensure we are continuously observing the Universe in case of any nearby supernova or other large events. When the large scale detectors become operational once again, there are plans to upgrade GEO600 to GEO-HF, which will improve its sensitivity at high-frequencies above $\sim 1\,\mathrm{kHz}$.

2.9 Next Generation Ground-based Detectors

Beyond the current network and the already planned upgrades, there is scope for the next generation of gravitational wave detectors, which are completely open to new design topologies and the most advanced technology based on all the lessons learned with large scale detectors to date. The Einstein Telescope (ET) is a future third generation gravitational wave detector currently being designed by many European institutions [33]. ET will circumvent many of the limitations imposed on the second generation detectors with new infrastructures underground to limit the effects of seismic noise and with cryogenic techniques being employed on the suspensions to reduce the thermal vibrations of the test masses. Currently the preferred topology for ET is a triangular infrastructure consisting of three interferometers with $10\,\mathrm{km}$ arm lengths and the use of similar length filter cavities. Each interferometer will be optimised for
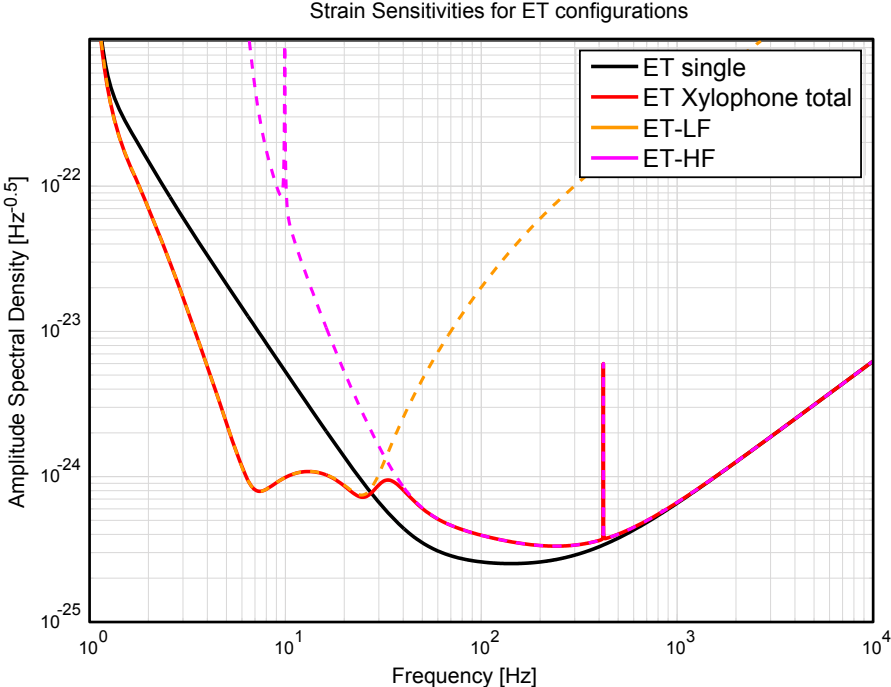
Figure 2.13: *Proposed ET strain sensitivity for the xylophone topology (red curve) comprised of a low frequency interferometer with low optical power, cryogenic silicon optics and very tall suspensions, and a high frequency interferometer using very high optical power, silica optics at room temperature and standard suspensions. A single broad-band detector (black curve) is also displayed for comparison, which highlights the improvement at low frequencies.*

specific frequency bands, which together will maximise the overall bandwidth of the detector. This so-called xylophone topology has been modelled with the best possible parameters [34] to provide a proposed design sensitivity curve as shown in Figure 2.13.

2.9.1 Advanced Techniques and Technology

The research of technologies for future generations of gravitational wave detectors is an exciting field with many opportunities coming from technology only recently available. Small scale prototype interferometers provide a test bed for these new technologies of which there are only a handful around the world. At Glasgow there is a 10m prototype in which I conducted two experimental projects investigating advanced technology and techniques. Chapter 3 contains the work that was carried out during 2007 - 2009 when the use of suspended diffractively coupled optical cavities was experimentally demonstrated. Chapter 4 describes the second experiment carried out during 2009 - 2010, investigating the dynamic behaviour and control requirements of optical springs when radiation pressure effects are sufficient to cause opto-mechanical coupling between cavity mirrors.

Chapter 3

Triple-Suspended, Diffractively-Coupled Fabry-Pérot Cavities

As discussed in chapter 2, there are a number of noise sources that can affect ground-based gravitational wave detectors. In this chapter I focus on the effect that high laser power can have on some of the primary optical components inside interferometers. I consider alternative technology that could be implemented within future gravitational wave detectors, whilst providing a thorough experimental demonstration of such technology.

3.1 Conventional Optical Components

3.1.1 Substrate Materials

Several criteria affect the choice of material used for the mirror and beam splitter substrates in ground-based gravitational wave detectors; (i) the material must have a low mechanical loss factor to constrain the effects of thermal noise, as previously discussed, (ii) it should also be possible to manufacture substrates in sizes suitable for the detectors, in mass up to tens of kilograms, (iii) the substrate material must have high thermal conductivity and a low thermal expansion to minimise thermo-mechanical distortions caused by any heating that results from absorption of laser light. This leaves a small selection of materials for consideration: in particular, fused silica and silicon, which are both high quality materials that can be manufactured to suitable sizes. Fused silica has favourable thermal conductivity and a thermal expansion coefficient $\alpha = 0.5 \times 10^{-6}/\text{K}$ [35] at room temperature. On the other hand it has been shown that the thermal expansion coefficient of silicon can reach zero at low temperatures, suggesting that the thermoelastic noise contribution should also become negligible [36]. Hence these two substrate materials have different regions in temperature in which they should be utilised in operation.

However, there is another criterion which currently dictates the material selection since current detector topologies require partially transmissive components, therefore the material must be transparent at the appropriate wavelength, normally 1064 nm. Since silicon is opaque at this frequency, this has led to fused silica as the nominal substrate material for the current network, along with the planned upgrades to the LIGO and Virgo detectors. The properties of fused silica however set limits to the performance of all first and second generation detectors, as will be discussed.

Figure 3.1: *Schematic of a multiple layer dielectric stack coating with alternating layers of refractive index n_1 and n_2 respectively, attached to a substrate material with refractive index n_s. Typical coatings have 20 to 32 pairs of layers.*

3.1.2 Mirror Coating Materials

Once a substrate material has been chosen using the selection criteria, a number of steps are required to shape, figure, polish and finally coat the surface to form a highly reflective mirror. Metallic mirror coatings are not suitable because their optical absorption is too high. Instead, a highly reflective coating is achieved by applying multiple alternating dielectric layers through a process known as ion-beam-sputtering. The layers are comprised of quarter wavelength dielectric materials with differing refractive indices as indicated by Figure 3.1.

For maximum reflection of the laser light with wavelength λ, from the contact surface of the substrate, the standard approach is to choose each layer of the dielectric material to be $\lambda/4$ in thickness. The relation between the optical thickness of each layer of material having a refractive index n and the physical thickness h is described by

$$\lambda/4 = nh. \tag{3.1}$$

For fused silica substrates used in interferometric gravitational wave detectors where Nd:YAG laser light is implemented the coatings are formed from up to 64 alternating layers of tantalum pentoxide (Ta_2O_5) and silica (SiO_2) to provide a highly reflective surface over a narrow frequency band [37].

3.1.3 Limitations of Conventional Materials in Future Detectors

Although using fused silica as the substrate material which has low mechanical loss on its own, it has been found that the addition of the multilayer coating on the surface introduces additional thermal noise into the interferometer [38]. The thermal noise associated with the dielectric coating is due to the mechanical loss of the multiple layers, with a dominant contribution coming from Ta_2O_5. There have been many studies into reducing the loss from the coatings by way of doping the coating material [39]. For instance, it has been shown that doping Ta_2O_5 with titania (TiO_2) can reduce the mechanical loss of the coating layers by a factor of 1.5 [40, 41], which, while encouraging for upgrades of current detectors, falls short of the requirements for future projects like the Einstein gravitational wave Telescope. It is therefore important to study alternative technologies that have lower mechanical loss yet still achieve the required high reflectivity for future detectors.

A further concern arises on consideration that the light power incident on some of the optical substrates in the current network during their operation is of the order 1 kW, while proposals for Advanced LIGO and Advanced Virgo require

even higher circulating light power to meet ambitious sensitivity targets. This also has troublesome implications, since a constant small fraction of incident light is always absorbed in the optical substrates of partially transmissive optics, causing localised heating which leads to thermal lensing due to a change of refractive index with temperature[42]. The strongest thermal lenses that will limit the detector sensitivity will occur inside the beam splitter and cavity input couplers, hence investigations into new technologies and interferometer topologies are currently underway to help overcome these concerns.

3.2 Diffractive Reflection Gratings

Diffractive reflection gratings offer a novel approach for splitting and recombining light fields without requiring transmission through optical substrates. Applying such devices in suitably modified interferometer topologies could potentially mitigate problems concerning thermal lenses in high power systems.

It is possible to create gratings on both fused silica and silicon substrates, therefore, these devices may also provide the solution for reducing the thermal noise contributions in optical components and suspensions if cryogenic techniques are adopted in the future. Otherwise, the use of silicon would require a change of laser wavelength to, for example, 1550 nm, where it is transparent.

Diffraction gratings can be manufactured for a range of potential applications within gravitational wave detectors such as cavity input couplers and beam splitters. Hence, gratings are appealing counterparts to conventional optical components.

Reflectivity approaching 100% has been obtained in gratings that are less than one wavelength thick [40]. Initial measurements on the mechanical loss of

grating structures etched onto substrate samples have been carried out at Glasgow, and in some tests show potentially lower loss than unetched samples [43]. Therefore, these encouraging initial tests have provided verification that diffractive devices are promising new alternatives for reducing the thermal noise inside interferometric gravitational wave detectors and should be investigated further.

An analysis of the behaviour of gratings when used as input couplers for cavities has revealed additional differences between gratings and traditional coupling mirrors that may affect the application of gratings in gravitational wave detectors. The most potentially damaging of these is the phase change due to transverse translational motion of the diffractive coupler relative to the laser beam when compared to an equivalent traditional cavity configuration [44]. A second feature of gratings is that there may be extra coupling ports, requiring changes to interferometer topology, and affecting the signals used to read out cavity lengths for the purpose of control and signal readout. It is therefore important to understand how to model diffractive couplers and validate such simulations by experiment. Moreover, testing grating coupled cavities is essential to inform design studies of 3rd generation gravitational wave detectors, such as the Einstein gravitational wave Telescope.

3.2.1   Considerations for Grating Design

Diffraction gratings can be designed for many applications. To generate a beam-splitter equivalent device, a four-port diffraction grating with appropriate diffraction efficiencies is topologically identical, as indicated by Figure 3.2, while a mirror equivalent can be generated by creating a two-port diffraction grating, as indicated by Figure 3.3 (b) or a three-port grating Figure 3.3 (c).
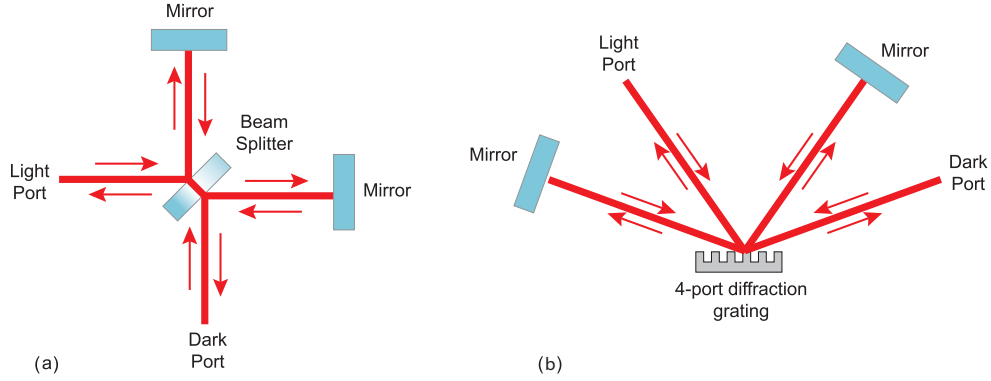
Figure 3.2: *(a) Illustration of a beam splitter within a Michelson interferometer topology and (b) a four-port diffractive reflection grating. There are four input and output ports on both the beam splitter and the diffraction grating and are thus topologically identical.*

When considering diffractive devices for use in gravitational wave detectors such as input couplers to Fabry-Pérot cavities, such as that described by 3.3 (c), it is important to understand the theoretical description for a standard optical cavity. Typically high finesse optical cavities are desired in gravitational wave detectors to maximise the detectors sensitivity to passing gravitational waves. The finesse $\mathcal{F}$ of a cavity can be defined in terms of the cavity mirror amplitude reflectivities ρ_1 and ρ_2 respectively as

$$\mathcal{F} = \frac{\pi\sqrt{\rho_1\rho_2}}{1 - \rho_1\rho_2}. \tag{3.2}$$

At Glasgow we were investigating the use of three-port diffraction grating, therefore I will use this device as an example for the following consideration of the technique. Figure 3.4(a) shows the input light coupling into the cavity by first order diffraction with an efficiency η_1, while the returning light from the end cavity mirror is coupled out by first and minus first order diffraction with the same efficiency. The gratings are typically fabricated by electron-beam
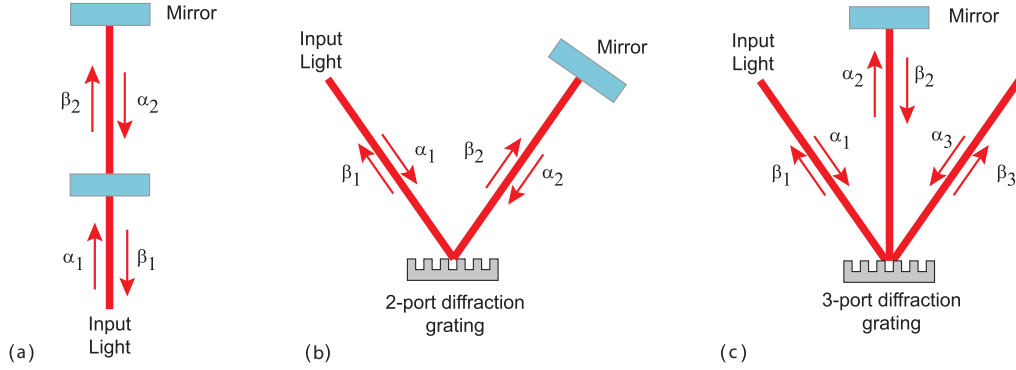
Figure 3.3: *(a) Illustration of a mirror as a Fabry-Pérot cavity input coupler, (b) a two-port diffractive reflection grating mounted as an input coupler, and (c) a three-port diffractive reflection grating in second order Littrow mount as input coupler to a Fabry-Pérot cavity.*

lithography, and we can initially assume each grating groove to be rectangular and therefore symmetric giving identical first order efficiencies. Therefore the reflectivity of the grating at normal incidence R_G (ρ_G^2), is determined by losses such as residual transmission through the substrate T_G (τ_G^2), and scattering S_G due to minor imperfections of the grating, as well as the two first order diffraction efficiencies as described by [45]

$$R_G = 1 - (2\eta_1 + T_G + S_G). \tag{3.3}$$

From Equation 3.3 it can be seen that to obtain maximum cavity finesse $\mathcal{F}$, it is important to minimise the scattering loss, the transmitted loss, and the first order diffraction efficiency in order to maximise the normal incidence grating reflectivity R_G.

The grating equation 3.4 describes the propagation angles of the diffracted orders ϕ_m, given by,

$$\sin\phi_m = \sin\phi_i + \frac{m\lambda}{d}, \tag{3.4}$$
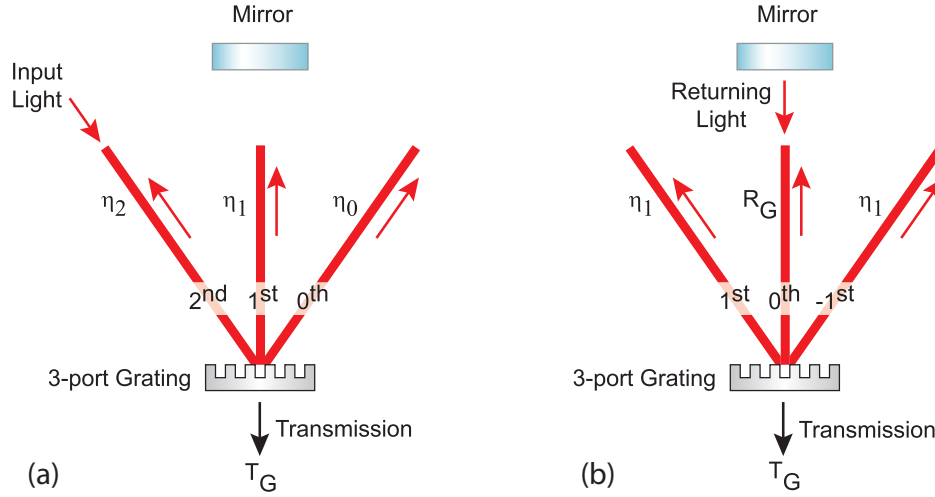
Figure 3.4: *(a) Illustration of a three-port diffractive reflection grating in second order Littrow mount as input coupler to a Fabry-Pérot cavity. The input light is first order diffracted into the cavity, and second order diffracted back along itself. (b) The intra-cavity light is first and minus first order diffracted out of the cavity. Transmission and scattering also affect the normal incidence reflection R_G.*

where ϕ_i is the angle of incident light, m is the diffracted order, λ is the wavelength of the light and d is the grating period. For the arrangement described by Figure 3.4 the incident beam requires the first order to be diffracted normally to the grating, giving,

$$\sin \phi_i = -\frac{\lambda}{d}. \tag{3.5}$$

Therefore, this demands the grating period to be larger than the laser wavelength, in our case $d > 1064$nm. Furthermore, to reduce scattering losses by unnecessary diffraction orders propagating in this configuration, the grating period is restricted to less than 2λ, hence the range of possible grating periods are restricted to 1064nm < d < 2128nm. The grating period that was used in our experiment was $d = 1450$nm, therefore given that $\phi_m = 0^0$, the incident

angle $\phi_i = 47.21^0$.

The transmission losses of the grating are determined by the surface material upon which the grating is formed. There are many techniques for generating grating structures on the surface of substrate material and I will here provide some fabrication details.

3.2.2 Grating Fabrication

Diffraction gratings can be manufactured through various fabrication techniques, with each method having different advantages and drawbacks. I will provide an overview of each technique and summarise the benefits and limitations of each method.

Gratings With Dielectric Coatings

A commonly used method to create gratings with high-efficiency reflectivity is to place the grating structure on top of a dielectric multilayer coating [46, 47] as shown by Figure 3.5(a). Alternatively, the grating can be etched into the substrate, upon which a multilayer coating is then applied as shown by Figure 3.5(b). The level of scattering losses in the device is determined by the quality of the grating structure, the dielectric coating and the substrate material.

Investigations of both fabrication techniques for generating three-port low-efficiency diffraction gratings show that applying the grating structure on the substrate *below* the high reflectivity coating can effectively reduce the grating scattering and transmission losses [45]. However, as the field progresses and lithographic technology improves, the optimum process for fabricating gratings
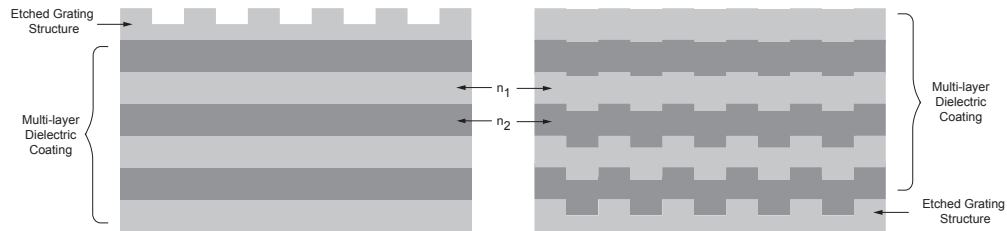
Figure 3.5: *Schematic diagram of a diffractive reflection grating etched above(a) and below (b) a dielectric multilayer stack of alternating layers of material with different refractive indices n_1 and n_2 respectively.*

will also evolve.

There are benefits to developing gratings with dielectric coatings onto fused silica substrates, as previously described. These include (i) the ability to use Nd:YAG laser light at 1064nm wavelength which is currently used within current and immediate planned upgrades of gravitational wave detectors, and (ii) the substrate and material choice are identical to conventional mirrors which provides a good tool for purely exploring the dynamic effects associated with gratings in optical cavities in comparison.

However, there are clear drawbacks to implementing dielectric coated gratings. This is due to the mechanical loss associated with the coating materials leading to thermal noise limitations in large baseline interferometers. Instead a different approach to obtaining high-reflectance low-loss low-efficiency diffractive optics must be found.

Realising Monolithic Gratings

A considerable amount of research in recent years has paved the way towards fabricating a high-reflectance low-loss low-efficiency diffractive device for coupling light into optical cavities. One suggested technique for generating these devices required generating resonant waveguide gratings from a periodically microstructured high refractive index layer attached to a low refractive index substrate [48] as illustrated in Figure 3.6(a). The principle behind the design requires higher diffraction orders to experience total internal reflection upon contact with the boundary layer of the low index substrate, thereby exciting resonant waveguide modes. In order to achieve resonant reflection at normal incidence, there are three grating parameter inequalities that must be satisfied [49]:

- $p < \lambda$ (to permit only zeroth order diffraction in air),

- $\lambda/n_H < p$ (to ensure first order diffraction in the high index layer),

- $p < \lambda/n_L$ (to permit only zeroth order diffraction in the substrate),

where p is the grating period, λ is the wavelength of incident light, n_H and n_L are the high and low refractive indices for the two dielectric layers respectively. It is possible to ensure that all transmitted light interferes destructively, provided the grating period p, the groove depth d, the ratio between the high to low refractive index media along with the ratio between the grating ridge b and grating period are all chosen properly. It has been shown that the waveguide layer thickness can even be zero as indicated by Figure 3.6(b), or alternatively a minimum thickness, t, of the low refractive index substrate material can provide zeroth order reflection with up to 100% grating reflectivity R_G and destructive transmission T_G as indicated by Figure 3.6(c).
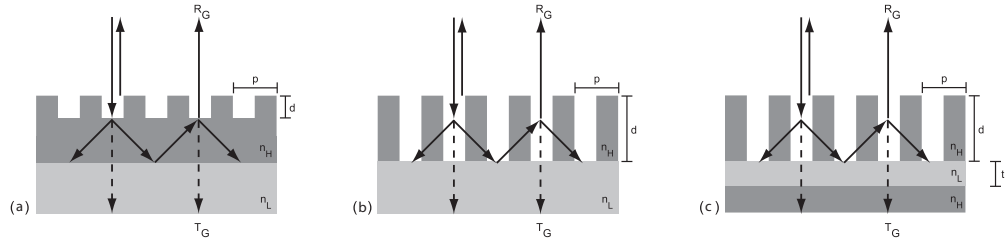
Figure 3.6: *Schematic diagram of a diffractive reflection grating etched onto a high refractive index layer attached to a low refractive index substrate (a). Another grating with identical properties can be formed without the high refractive index n_H layer (b) and furthermore a minimum thickness of the low refractive index n_L layer can be found to give the same grating properties (c).*

The overall reduction of the multi-layer dielectric coatings should greatly improve the associated thermal noise contributions, however, the required use of two materials in the fabrication could potentially decrease the high mechanical quality factor of the substrate [50]. Therefore, fabricating a monolithic grating design was pursued.

From the earlier grating designs it became apparent that a monolithic grating structure could be achieved by replacing the low refractive index layer with an effective medium such as air as shown in Figure 3.7(a). Once the difficult fabrication process had been overcome, it was possible to generate the desired grating structure onto a single silicon crystal as shown in Figure 3.7(b) and through experimental investigations a reflectivity of $99.79 \pm 0.01\,\%$ at a wavelength of $1550\,\text{nm}$ was observed [51], thus providing verification of high-reflectivity monolithic gratings for use in optical cavities.

One limitation of this particular monolithic grating design is the complicated fabrication process, requiring various techniques each working to very high tolerance. Additionally, at the time of writing, it has been possible to produce
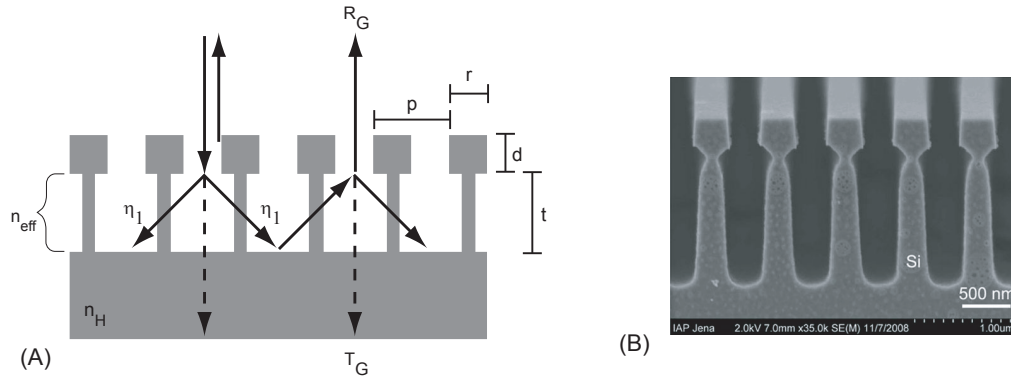
Figure 3.7: *Schematic diagram of a monolithic diffractive reflection grating (a) with a distinct T shape structure to give the desired properties and an electron microscope image (b) of such a grating formed onto a silicon crystal (image courtesy of IAP Jena).*

these gratings on relatively thin silicon substrates up to tens of centimetres in area, however, fabrication on much greater surface areas would need to be achieved before this technology becomes a realistic alternative to current mirrors designs for ground-based gravitational-wave detectors. Moreover, the exposed nano-structured grating surface is highly susceptible to damage and pollution with only a limited range of suitable cleaning processes.

Recently, there has been more research into new fabrication schemes that may allow burying the nano-structured diffraction grating below the surface of the substrate as illustrated by Figure 3.8. Such a device could be of enormous interest, because it may potentially protect the diffraction grating from damage and pollution and could allow the front flat surface to be polished. This device known as an encapsulated grating is based on the same basic principles for obtaining monolithic gratings as already mentioned, however the fabrication process for this device is based on a quasi-monolithic technique using both crystalline and amorphous silicon. Experimental investigations of a pro-
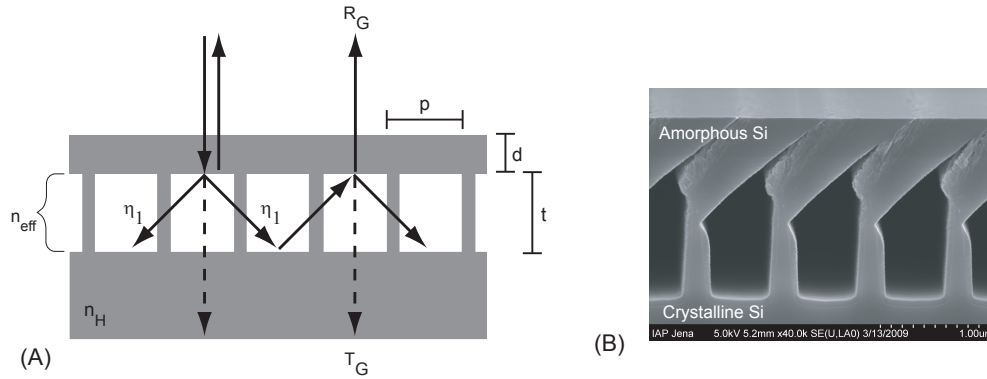
Figure 3.8: *Schematic diagram of an encapsulated quasi-monolithic diffractive
reflection grating (a) designed for high reflectivity and an electron microscope
image (b) of such a grating formed onto a silicon crystal with an amorphous
silicon flat surface (image courtesy of IAP Jena).*

totype encapsulated quasi-monolithic grating has revealed a normal incidence
reflectivity of $93 \pm 0.5\,\%$ at $1550\,\text{nm}$ wavelength [50]. Although, this level of
reflectivity is low compared to the aforementioned mirror alternatives, it is
expected that with further research and development into the design and fab-
rication process, perfect reflectivity is possible. Therefore, we want to provide
more evidence to support this technology as a serious alternative for future
generations of high-precision gravitational wave laser interferometers.

3.3 Experimental Demonstration of a Diffractively Coupled Fabry-Pérot Cavity

During the period $2007 - 2009$ the fabrication techniques of diffractive re-
flection gratings were showing promising signs for use in future gravitational
wave detectors and therefore numerous experimental investigations were re-

quired to validate their potential or indeed highlight issues concerning additional noise or isolation requirements. A number of theoretical and table-top experiments have examined the input-output amplitude and phase relations for a three-port diffractively coupled Fabry-Pérot cavity [48, 52]. At Glasgow, one of the prototype interferometer arms was commissioned as a diffractively coupled Fabry-Pérot cavity to investigate these devices in a triple-suspended environment. The primary aims of the experiment were to fully characterise the control signals and to verify predicted dynamic effects when maintaining the system at the operating condition.

3.3.1 The JIF Laboratory

The Glasgow 10 m prototype interferometer is housed in the Joint Infrastructure Facility (JIF) laboratory at Glasgow University as shown in Figure 3.9. The room is maintained to a class 100 cleanroom environment to prevent particle contamination. The prototype consists of a 10 m length vacuum system to remove any acoustic noise and all optical components are suspended as multistage pendulums to provide seismic isolation and allow freedom of motion. The mirrors used in the prototype are manufactured from fused silica substrates and coated with multiple dielectric layers to provide a highly reflective surface. A 2W Nd:YAG 1064 nm wavelength laser light source is input from an optics bench, where mode-matching and cleaning optics are located, along with necessary electro-optic modulators and photodetectors for interferometric length sensing and control schemes as will be discussed later. The room suspended above the interferometer houses the computer system to retrieve the suspension shadow sensor information and sensing signals for controlling the mirror positions through electromagnetic actuators.
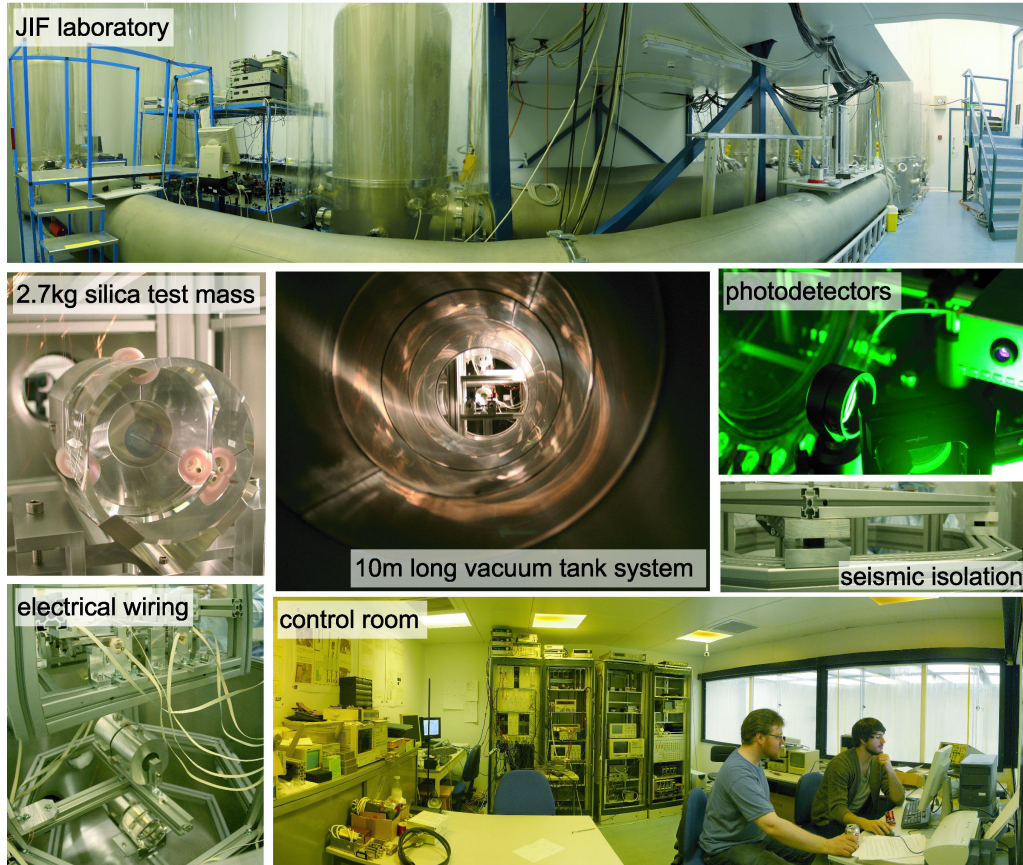
Figure 3.9: *(Clockwise from top) Panorama image of the JIF laboratory clean room, tuned photo-detetctors located at the system output ports, passive seismic isolation, JIF laboratory control room, shadow sensor and local control electrical wiring, typical fused silica test mass stage with reaction mass and electromagnetic feedback actuators for global control, (middle)* $10\,\mathrm{m}$ *length vacuum system containing interferometer arms.*

3.3.2 Upgrading the Glasgow $10\,\mathrm{m}$ Prototype

The diffraction grating under investigation was manufactured by etching a binary structure into a fused silica substrate then coating with multiple alternating layers of Tantala (Ta_2O_5) and Silica (SiO_2), to give an ultra low-loss low-efficiency three-port grating with a period $d = 1450\,\mathrm{nm}$ [45] as shown by
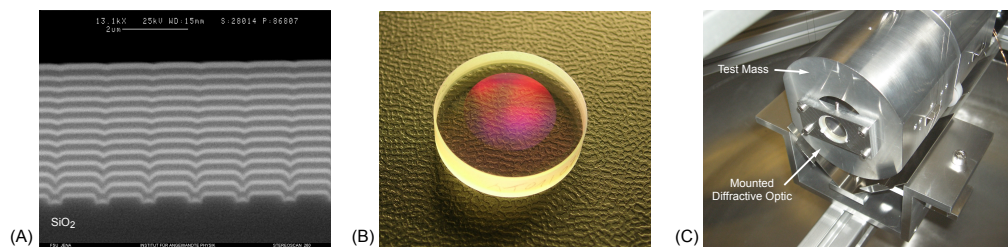
Figure 3.10: *Electron microscope image (a) of the three-port dielectric coated diffraction grating etched onto a fused silica substrate, photograph of the* 1 inch *diameter optic (b) with grating structure in centre, and photograph of grating mounted inside aluminium jig (c) attached to the front face of the triple-suspended inner test mass.*

Figure 3.10. The grating was mounted in second order Littrow configuration onto a an aluminium jig attached to the cavity face of the suspended test mass. The grating was illuminated at an angle of 47.2^0 with s-polarized light at 1064 nm wavelength, from a Nd:YAG laser (Model Mephisto 2000NE from Innolight). The configuration chosen, as illustrated by Figure 3.11, provides weak coupling into and out of the cavity, ensuring that the resulting system is directly comparable with a conventional Fabry-Pérot cavity.

3.3.3   Mode Matching

As with any large-baseline laser interferometer utilising optical cavities, the light input from the optical bench must be well mode matched into the system. This means that the propagating laser spatial mode should match the resonating cavity mode, or equivalently that the radius of curvature of the beam should be equal to the radius of curvature of the cavity mirrors at the mirror positions. Therefore, to mode match the input light requires understanding how a laser beam expands as it propagates. In the Glasgow 10 m
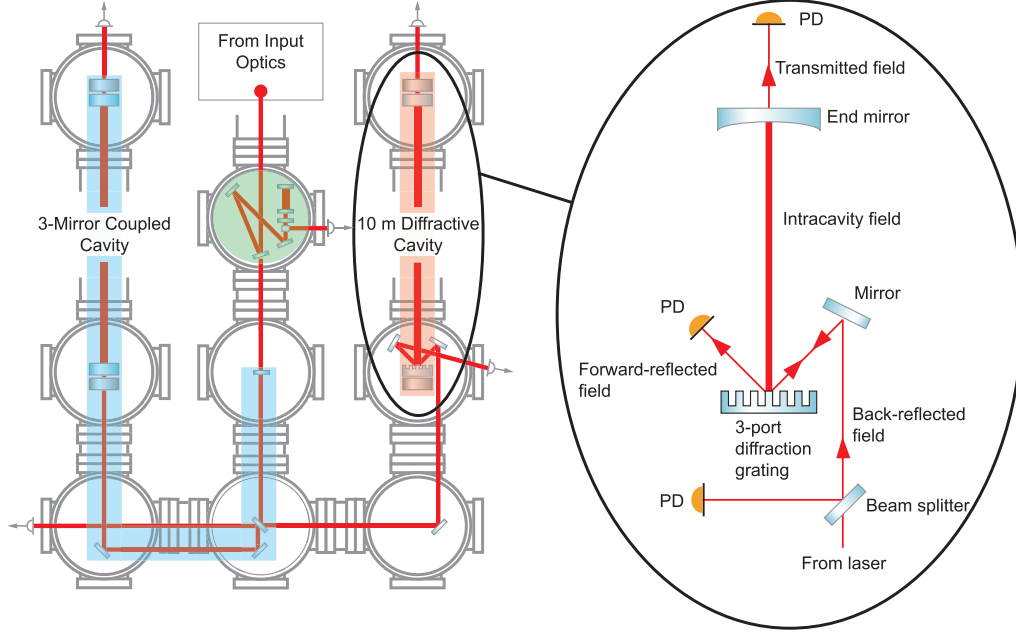
Figure 3.11: *Topology of the Glasgow* 10 m *prototype (left) showing the traditional and diffractive interferometer arms and simplified schematic of the three-port grating, used in second order Littrow configuration, as the input coupler for a diffractive cavity. Tuned photodiodes (PD's) are positioned at all 3 output ports to detect the DC power and RF component for derivation of the control signals.*

prototype system a Gaussian TEM_{00} beam profile is input, which expands according to the relations [53]

$$\frac{\pi w_0^2}{\lambda R} = \frac{\lambda}{\pi w^2} \left(z - z_0\right) \tag{3.6}$$

and

$$1 - \left(\frac{w_0}{w}\right)^2 = \frac{1}{R} \left(z - z_0\right), \tag{3.7}$$

where w_0 is the radius of the beam at the waist (narrowest point), z_0 is the position of the waist along the propagation axis of the beam, w is the beam radius at point z along the propagation axis, R is the radius of curvature of the beam at point z and λ is the wavelength of the light. The radius of a gaussian

beam is defined as the distance from the centre of the beam (point of maximum intensity) at which the intensity has dropped to $1/e^2$ of the maximum.

In this experiment the end cavity mirror has a $15\,\mathrm{m}$ radius of curvature and the inner cavity mirror, which is typically flat, was replaced with the aforementioned flat diffractive reflection grating. The parameters for the diffractively coupled cavity ($R = 15\,\mathrm{m}$, $z = 9.83\,\mathrm{m}$, $z_0 = 0\,\mathrm{m}$ and $\lambda = 1064\,\mathrm{nm}$) were substituted into Equations 3.6 and 3.7 and the system was solved for w_0. This gives the optimum coupling of light into the cavity when the waist at the diffraction grating $w_0 = 1.55\,\mathrm{mm}$, as seen along the cavity axis. However, the beam geometry was altered using a steering mirror to ensure the beam was incident on the face of the grating at an angle of 47.2^0. This required an elliptical input beam to provide a circular projection of the beam inside the cavity. Through elementary geometrical algebra, it can be shown that the x-waist (horizontal axis) should be 68% of the y-waist (vertical axis) in order to obtain the desired circular cavity beam.

The correct waist profile was achieved using two cylindrical lenses placed at appropriate locations and separations on the optical bench after the electro-optic modulators and before the steering of the beam into the system.

3.3.4 Amplitude Stabilisation

As the investigation began, some initial cavity tests were performed. By monitoring the transmitted demodulated error signal on an oscilloscope and slowly changing the laser frequency (known as sweeping the cavity) by at least one free spectral range, the shape of all the resonance features and their separation can be captured. The data indicated double carrier resonance features, which should not be present in an optimised system. The laser light was subsequently

monitored at a convenient pick-off point on the optical bench before entering
the system, using a simple photodiode arrangement powered with a $9\,\mathrm{V}$ DC
supply. Looking at the DC component on a spectrum analyser it was possi-
ble to observe amplitude spikes occurring at multiples of $100\,\mathrm{Hz}$, therefore it
became apparent that the mains supply of the laser could be adding in strong
levels of amplitude noise.

Pump diode fluctuations cause heating and cooling of the laser crystal, gen-
erating fluctuations of the laser frequency analogous to modulation, and with
these lasers there is a strong correlation between amplitude and frequency
noise. In our experiment the $100\,\mathrm{Hz}$ frequency fluctuations potentially had a
significantly sized modulation index to split the carrier frequency into multiple
resonance features. This affects the entire modulation scheme and can result
in unstable cavity locking. It is worth noting that the laser supply problem was
only recognised at this point because the new cavity finesse was larger than
that of earlier experiments. The higher cavity finesse is directly related to a
narrower resonance linewidth and therefore it was possible to resolve narrower
frequency components.

Before changing the experimental setup, the level of $100\,\mathrm{Hz}$ fluctuation was
checked. Monitoring the light using the same photodiode as previously men-
tioned, a DC level of $60.5\,\mathrm{mV}$ and an AC fluctuation of $14.04\,\mu\mathrm{Vpk}$ was ob-
served, giving a fractional voltage change of 2.32×10^{-4}. This is also equal
to the fractional current change, and since the laser pump current was set
to $4.4\,\mathrm{A}$, the fluctuation in the pump current was $1.02\,\mathrm{mA}$. Based on earlier
experimental results [54], which indicated $\sim 0.3\,\mathrm{MHz/mA}$ response at $100\,\mathrm{Hz}$,
this suggested there would be a laser frequency change of $\sim 306\,\mathrm{kHz}$. Since the
separation of the resonance peaks observed on the oscilloscope during a cavity
sweep was approximately $300\,\mathrm{kHz}$, this result satisfied the assumption that
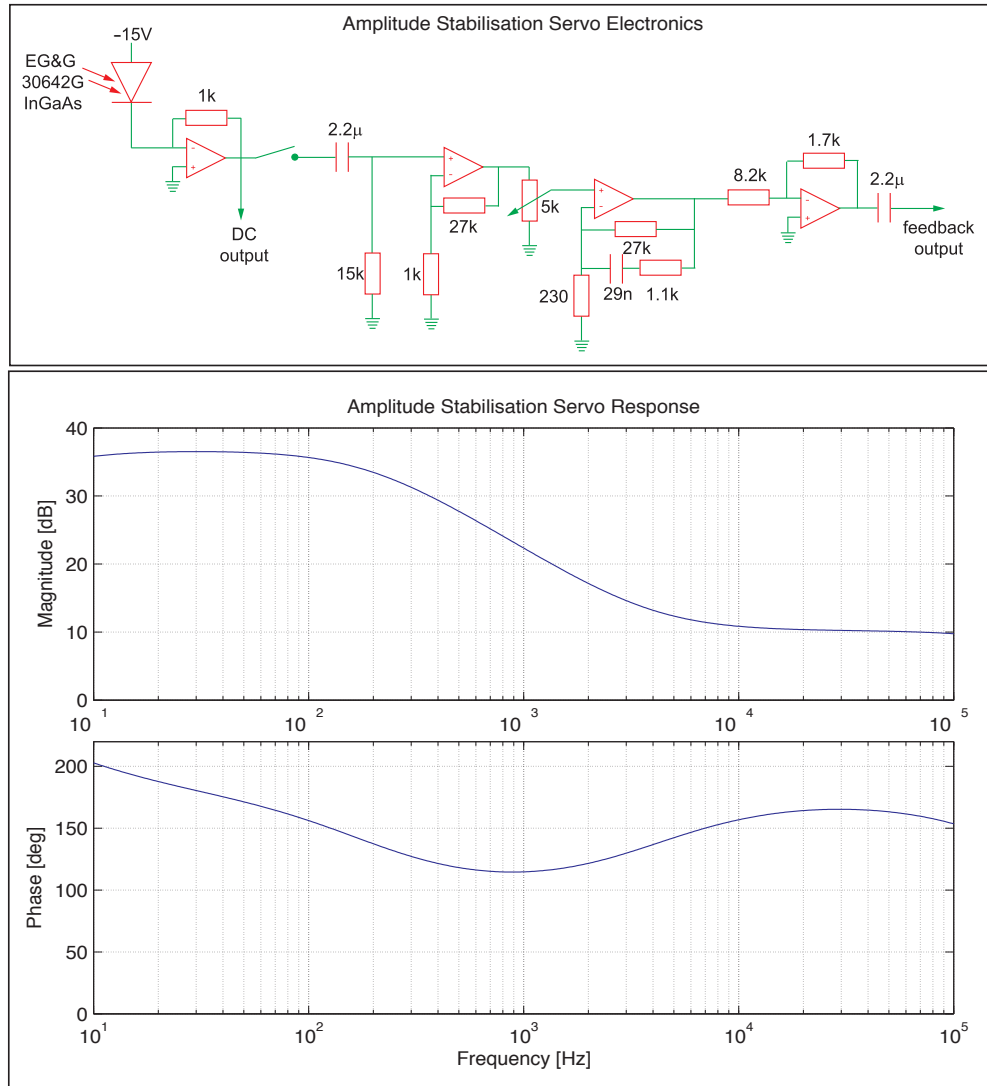
Figure 3.12: *Circuit diagram for the amplitude stabilisation photodetectors and servo system and the calculated servo response. The servo is a feedback system with enough range to stabilise the amplitude by removing unwanted noise components. A 360 degree correction has been applied to the phase data to remove phase wrapping.*

this problem was from the 100 Hz amplitude spikes due to the mains power supply of the laser.

A purpose-built amplitude stabilisation servo [20] was built using the design illustrated in Figure 3.12 in order to reduce the mains supply peaks. The photodetector used to monitor the light is a 2 mm InGaAs photodiodes from EG&G operated with a reverse bias of 15 V and shielded from ambient light. The photodetector has a bandwidth of 20 MHz and power dissipation of up to 250 mW.

The light level hitting the photodetector was around 9 mW giving an output DC level of ~ 6.15 V. This level was chosen as the suitable level before saturation effects were observed on the photodetector output. The output signal from the amplitude stabilisation servo was used for feedback onto the injection current input located on the laser power supply. This feedback signal was also directed to a spectrum analyser to provide an independent measurement of the amplitude fluctuations. The amplitude noise spectrum up to 12.8 kHz was monitored when the amplitude stabilisation servo was switched off and when it was turned on, showing a reduction of the 100 Hz peaks by around 30 dBVrms as shown by Figure 3.13.

With the amplitude stabilisation servo aligned to the pick-off light, with feedback onto the laser current supply and in operation, the multiple carrier peak features had been removed. This allowed the chosen modulation scheme to be implemented properly and allowed the system to be locked to TEM_{00} resonance in a stable state.
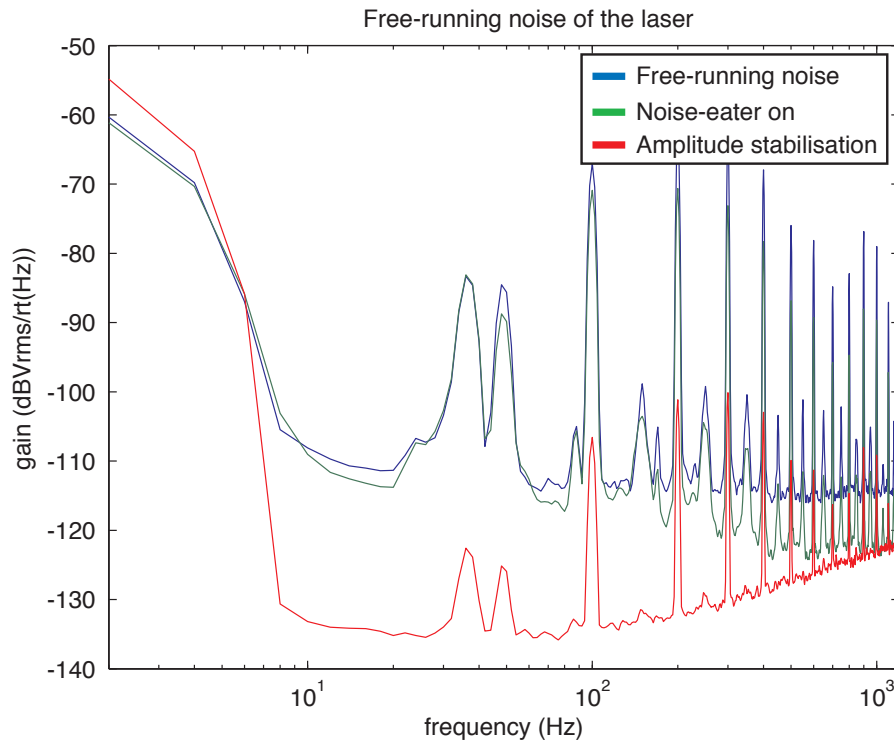
Figure 3.13: *Fast Fourier Transform (FFT) measurement taken using a spectrum analyser showing the effect of amplitude stabilisation by injecting into the laser current supply. An improvement of ~ 35 dBVrms is observed on the 100 Hz peaks as well as a reduction in the overall noise floor.*

3.4 Control and Length Sensing Signal Extraction

Conventionally, to maintain a gravitational wave detector at the operating point, monochromatic laser light, known as the carrier light, is held resonant inside the optical cavities of the interferometer by suitable feedback control. Modulation sidebands are added to the carrier light before entering the system, as prescribed in the Pound-Drever-Hall (PDH) technique [55], and the light
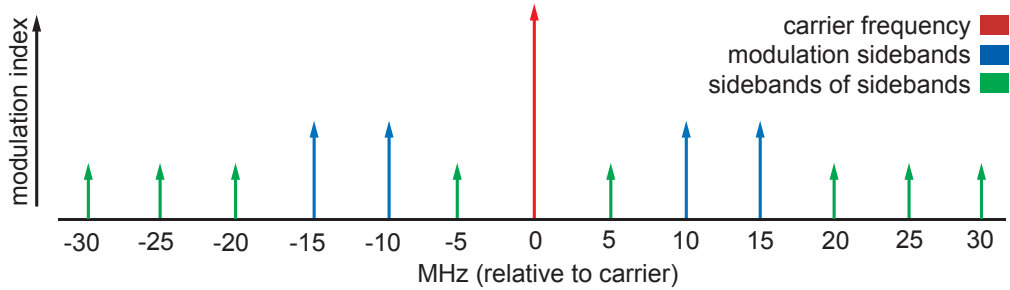
Figure 3.14: *Illustration of the different frequency components on the light field with modulation at* 10 MHz *and* 15.24 MHz*. Note this diagram is not to scale.*

exiting the cavity is subsequently detected on tuned photodetectors located at the output ports. The detected light is demodulated with a local oscillator at the modulation frequency to obtain information regarding the interaction of the frequency components. The bi-polar error signal obtained indicates the relative length between the cavity mirrors and can then be used to control the cavity length through suitable electronic feedback.

From Figure 3.11 it can be seen that our system has three detection ports, and to enable signal extraction from each output required the carrier light to be modulated twice. As with the traditional PDH technique, the modulation frequency for the forward- and back-reflected ports can be arbitrarily chosen, and for convenience 10 MHz was used in our system. However, to monitor the cavity length with the transmitted port required the use of sidebands just off-resonance at 15.24 MHz, close to the free spectral range of our cavity of 15.27 MHz. An illustration of the various radio frequency (RF) components on the light is provided in Figure 3.14 for clarity.

3.5 Modelling a Diffractively-Coupled Fabry-Pérot Cavity

The study of interferometer topologies is reasonably straight forward when dealing with the simple relationships among linear light fields and numerical techniques are routinely used to compute the signals obtained at various photodetectors in response to changes in the relative positions of the optics. When additional optical components or modulation sidebands are added, the use of numerical simulations becomes vital since the equations describing the fields become more and more complicated due to the increasing number of variables. There are a number of software packages available for modelling the interactions of light fields with optical topologies such as interferometers. FINESSE [56] is one script driven optical simulation program that has been used in this investigation to predict the various field amplitudes at different points in the system. Another computer programming package that has been used extensively throughout this work is MATLAB [57], which is a powerful and versatile tool for numerically solving otherwise complicated equations. Utilising numerical simulation packages such as these are necessary for the development of length sensing and control schemes required to keep the interferometers at the desired operating point and to read out the signals, including the gravitational wave signal.

One of the most fundamental concepts for advanced interferometry is the two-port Fabry-Pérot optical cavity consisting of two partially transmissive mirrors (see Figure 3.15). The incident light field E_i interacts with the input mirror giving the cavity fields E_{c1} and E_{c2}. The cavity field leaks light through the input mirror and superimposes with the directly reflected light to produce a reflected light field E_r, as well as the light leaking through the end mirror to
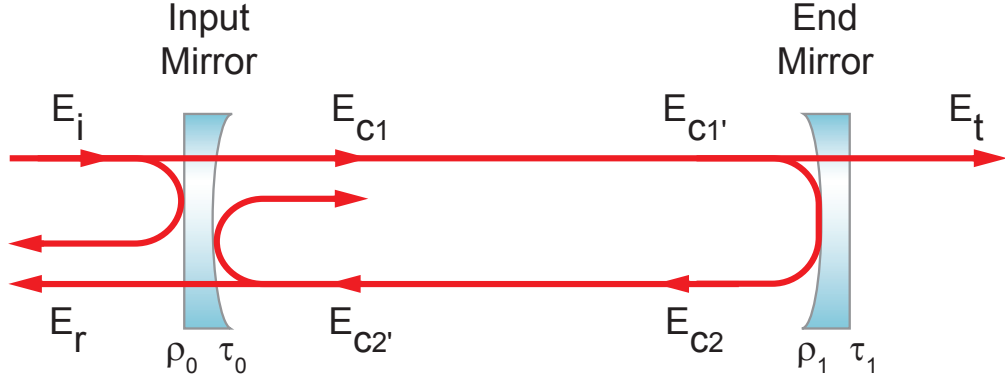
Figure 3.15: *Schematic diagram of a simple optical cavity showing the incident light field E_i interacting with the input mirror giving the cavity fields $E_{c1,c2}$ ($E_{c1',c2'}$ have gained an additional phase component due to traversing the length of the cavity). The cavity field leaks light through the input mirror and superimposes with the directly reflected light to produce a reflected light field E_r, as well as the light leaking through the end mirror to produce a transmitted field E_t.*

produce a transmitted field E_t. The input−output relations of such cavities are well understood and can be derived from the amplitude reflectance ρ and transmittance τ of the two-port mirrors as described by

$$\mathbf{S_{2p}} = \begin{bmatrix} \rho & i\tau \\ i\tau & \rho \end{bmatrix}. \tag{3.8}$$

Expressing the cavity length L as a tuning parameter $\phi = \omega Lc$, where ω is the angular frequency and c is the speed of light in vacuum, it can be shown that the cavity fields satisfy

$$E_{c1} = E_i i\tau_0 d, \tag{3.9}$$

and

$$E_{c2} = E_{c1}\rho_1 e^{i\phi}, \tag{3.10}$$
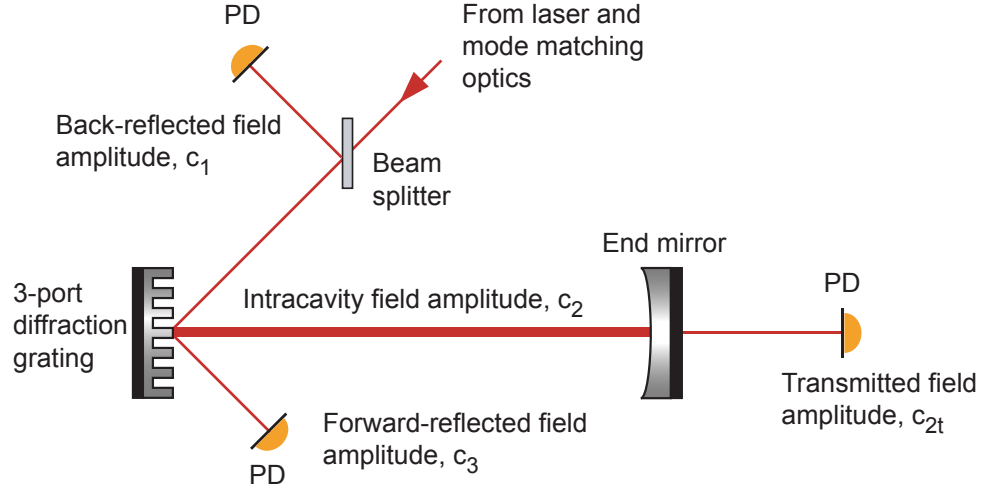
Figure 3.16: *Simplified schematic diagram of the 3-port diffraction grating as input coupler to a Fabry-Pérot cavity in 2nd order Littrow mount. There are three output fields; forward reflected (c_3), transmitted (c_{2t}) and back reflected (c_1). Tuned photodetectors are located at each port to detect the DC and RF components used for length sensing and cavity control.*

which can be used to derive the reflected and transmitted field as

$$E_r = E_i \left(\rho_0 - \tau_0^2 \rho_1 e^{2i\phi} \right) d, \tag{3.11}$$

and

$$E_t = E_i \left(-\tau_0 \tau_1 e^{i\phi} \right) d, \tag{3.12}$$

where $\rho_{0,1}$ and $\tau_{0,1}$ are the amplitude reflection and transmission efficiencies of the input mirror and end mirror respectively and d represents the resonance factor, defined by

$$d = \frac{1}{(1 - \rho_0 \rho_1 e^{2i\phi})}. \tag{3.13}$$

Therefore it has been shown that a traditional two-port Fabry-Pérot cavity couples one input field to two output fields and can be modelled using the

amplitude reflection/transmission efficiencies of the mirrors. However, by re-placing the input coupler with a three-port diffractive reflection grating, each input field couples to three output fields as shown in Figure 3.16. Modelling the configuration used in this investigation is achieved by implementing a second order Littrow incident beam ($\theta_i = \arcsin(\lambda/d)$) coupling to the orders $0, 1, 2$ and a normally incident beam coupling to the orders $-1, 0, +1$. This type of coupling leads to more complex phase relations compared to a conventional two-port cavity, which can be represented by a scattering matrix:

$$\mathbf{S_{3p}} = \begin{bmatrix} \eta_2 e^{i\phi_2} & \eta_1 e^{i\phi_1} & \eta_0 e^{i\phi_0} \\ \eta_1 e^{i\phi_1} & \rho_0 e^{i\phi_0} & \eta_1 e^{i\phi_1} \\ \eta_0 e^{i\phi_0} & \eta_1 e^{i\phi_1} & \eta_2 e^{i\phi_2} \end{bmatrix}, \tag{3.14}$$

where $\eta_{0,1,2}$ and $\phi_{0,1,2}$ are the amplitude diffraction efficiencies and phase changes on diffraction for zeroth, first and second orders respectively, and ρ_0 is the amplitude reflectivity at normal incidence. For each output port of the grating indicated by Figure 3.16, the field amplitudes have been investi-gated [52] and thus the amplitudes arriving at each of our photodetectors can be described by:

$$c_1 = \eta_2 e^{i\phi_2} + \rho_1 \eta_1^2 e^{2i(\phi_1 + \phi)} d, \tag{3.15}$$

$$c_{2t} = i\tau_1 \eta_1 e^{i(\phi_1 + \phi)} d, \tag{3.16}$$

$$c_3 = \eta_0 + \rho_1 \eta_1^2 e^{2i(\phi_1 + \phi)} d. \tag{3.17}$$

By assuming the grating is symmetrical with respect to normal incidence and that there is *no* optical loss attributed to it, the following energy-conservation law can be derived from the unitarity condition of $\mathbf{S_{3p}}$:

$$\rho_0^2 + 2\eta_1^2 = 1. \tag{3.18}$$

Hence, to obtain the maximum normal incidence reflection for use in high finesse cavities, demands a low first order diffraction efficiency η_1. Similarly,

for second-order Littrow incidence it is possible to define

$$\eta_0^2 + \eta_1^2 + \eta_2^2 = 1. \tag{3.19}$$

Therefore, when considering an ideal grating, the upper and lower limits for η_0 and η_2 for a given reflectivity ρ_0 are determined by

$$\eta_{0,min}^{max} = \eta_{2,min}^{max} = \frac{1 \pm \rho_0}{2}. \tag{3.20}$$

As mentioned in Section 3.2 there are two types of loss mechanisms from gratings. The grating scattering loss is attributed to imperfections in the grating structure that can cause light to couple to higher diffraction orders, while light can also be absorbed by the grating coatings, resulting in transmission loss. Together these can be treated as an overall power loss.

To model the power loss L_G of a grating requires that the right hand side of equations 3.18 and 3.19 be replaced by $1 - L_G$, in order to conserve energy. From the specifications of our grating, as presented in Table 3.1, and the reflection/transmission efficiencies (ρ_1/τ_1) of the end mirror, all the cavity properties can be determined numerically. Just as relatively high finesse cavities are employed to obtain strong power buildup in conventional interferometers, weakly coupled and hence high finesse grating-coupled cavities are of interest. This motivated our choice of grating. Furthermore, based on the field equations 3.15, 3.16 and 3.17 a numerical simulation of the diffractive cavity was built, using the MATLAB software package. This simulation allowed us to compare experimental findings for the amplitude and power of output light fields with modelled predictions.

Parameter	Value[%]
η_0^2	99.714
η_1^2	0.069
η_2^2	0.018
ρ_0^2	99.663

Table 3.1: *Parameter values of the three-port diffraction grating, provided by AEI in Hannover where it was first tested.*

3.6 Characterisation of Output Signals

The FSR of our cavity is 15.27 MHz and by monitoring the DC signal from the transmitted port, the corresponding full width half maximum (FWHM) was determined to be 13.80 ± 0.64 kHz. The measured finesse of the cavity was 1107 ± 51, in agreement with the prediction of 1177 ± 27 From the grating parameters used in the model we were also able to calculate the expected grating loss using the identity $L_G = 1 - (\rho_0^2 + 2\eta_1^2)$, which was determined to be 0.199%, closely matching a measured value of $0.177 \pm 0.025\%$ found in a measurement at AEI-Hannover [58].

One way to establish whether the sensing signals predicted by the model agree with experiment is to sweep the length of the cavity by at least one round-trip wavelength (one FSR in frequency terms). The demodulated signal from each port was subsequently compared to the prediction. The slope of this signal at the operating point gives the effective optical gain for that output, as is needed to calculate linearised servo system responses. In this experiment, instead of sweeping the cavity length the laser frequency was swept. This has the advantage that it does not risk causing alignment changes of the cavity that could cause higher order cavity modes to become excited thus producing

extra features in the result.

As discussed in Chapter 2, the RF signal from each detection port can be demodulated in two orthogonal phases; 'in-phase' and 'quadrature-phase'. The demodulation phase in the 'quadrature-phase' case was adjusted to minimise the detected signal, while the 'in-phase' signal was obtained by adding a 90 degree phase shift in the demodulation process. The demodulated signals obtained in the experiment are shown in Figure 3.17 and are seen to be in good qualitative agreement with modelled predictions [59]. The discrepancies between the experiment and modelled length sensing signals can be attributed to the finite rate of sweep in the experiment. The model is 'quasi-static' and therefore does not predict the slight asymmetry in the patterns seen in the experiment as stored light leaks out after a small delay. There is a practical limit to how slow a sweep can be made due to uncontrolled 1 Hz motion of the pendulums, since longitudinal, lateral and angular motion of the mirrors cause small misalignments. These effects are almost unavoidable when dealing with suspended optics but it is clear that the model matches the main features of the observations.

It is necessary to calibrate the demodulated signals detected at each port with the modelled signals to investigate the level of quantitative agreement. This required comparison between the relative size of the in-phase slopes to that of the transmitted port. The ratios of the signal responses indicate good agreement and are presented in Table 3.2.

Analysis of Figure 3.17 indicates that only the transmitted signal will be symmetrical around the centre of resonance. This is because light has been diffracted into the cavity only once, and therefore all frequency components receive the same phase shift before resonating. From previous investigations with table-top cavities [48], the extent of the asymmetry was seen to be de-
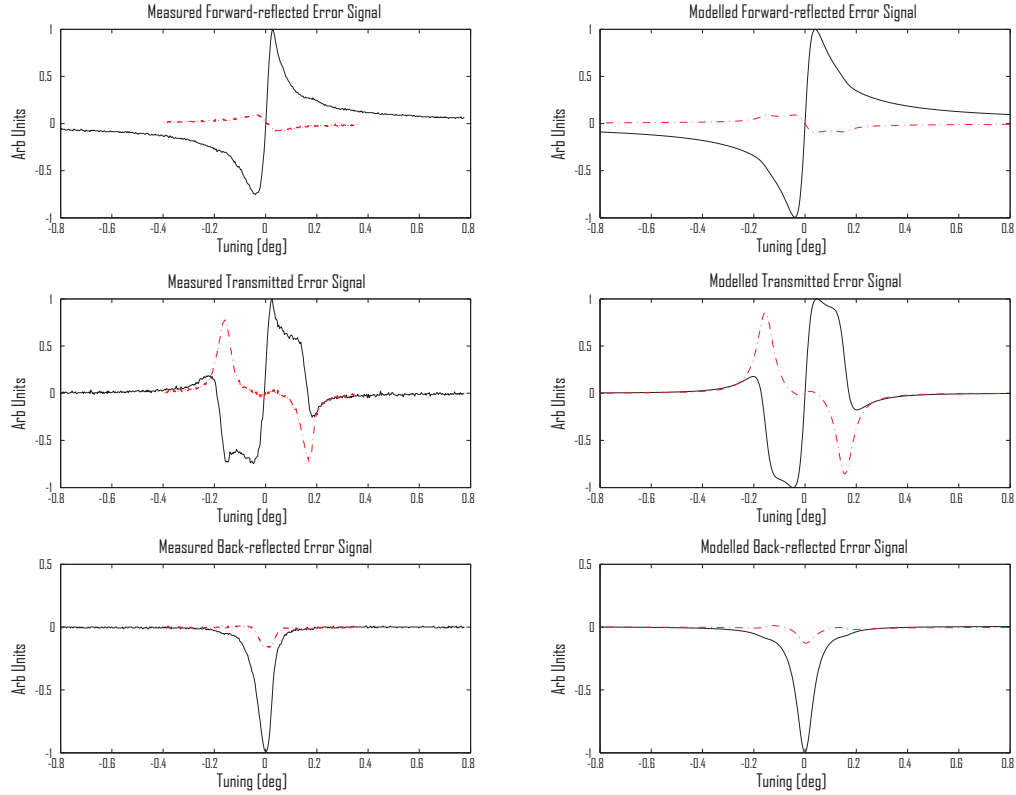
Figure 3.17: *Normalised RF power for each output port; forward-reflected (top), transmitted (middle), and back-reflected (bottom). The measured data and modelled predictions of the length sensing signals are presented on the left and right hand side respectively. The solid (black) trace indicates in-phase measurements, and the dashed (red) trace indicates quadrature-phase. The absolute scaling between modelled forward-reflected, transmitted, and back-reflected ports is approximately* $127 : 1 : 14$.

termined by the values of the η_0 and η_2 diffraction efficiencies. With our numerical simulation accurately validated by experiment, we were also able to probe the effects of asymmetry on the demodulated output signals by altering the grating parameters. An interesting result of this analysis is that, through careful choice of demodulation phase, we can extract signals from each of the

Parameter	Measured Value [dB]	Modeled Value [dB]
back-reflected/transmitted	-26.93	-26.99
transmitted/transmitted	0	0
forward-reflected/transmitted	43.07	44.74

Table 3.2: *The measured and modelled signal response for each port normalised to the response of the transmitted port.*

reflected ports which sum together to reconstruct a traditional Pound-Drever-Hall locking signal [60](see Figure 3.18). This has been compared to other measurements carried out with different apparatus that show the same effect, made at AEI [58].

The diffractive optic used in our investigation had a second order diffraction efficiency close to the minimum possible, hence the forward reflected signal had a shape that closely resembled the Pound-Drever-Hall signal. It was possible to lock the cavity using the signal from this port, although not quite at the centre of resonance, therefore the cavity was instead locked to the transmitted error signal (which does exhibit symmetrical behaviour around the centre of resonance). Locking to this port also makes it possible to investigate the dynamic behaviour and additional effects associated with suspended diffractively coupled optical systems.

3.7   Dynamic Grating Effects

Investigations of grating interferometers have shown that additional phase components attributed to the relative movements between the grating surface and incident light fields couple to the detected output fields [44]. Unlike
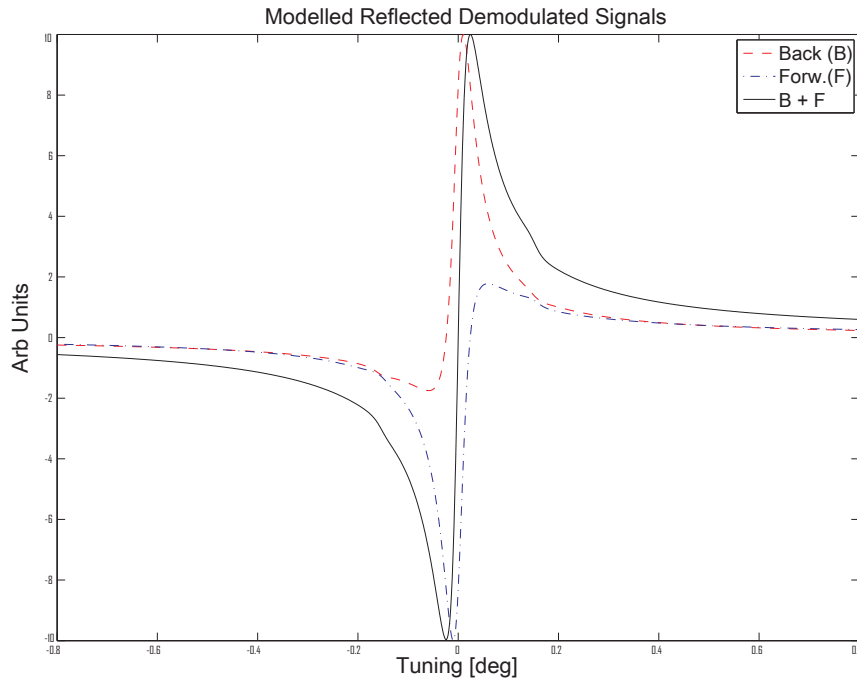
Figure 3.18: *Modelled demodulated signals; back-reflected (red) and forward-reflected (blue) indicated by dashed traces, and the combined back-reflected + forward-reflected (black) indicated by a solid trace. The grating parameters used here are for an ideal (lossless) grating with $\rho_0 = 0.99663$, $\eta_1 = 0.0407$, and $\eta_0 = \eta_2 = 0.7065$.*

conventional flat mirrors and beam splitters, the alignment of the grating geometry relative to the input beam, or conversely the alignment of the input beam relative to the grating geometry also affects the diffracted beam pointing differently, due to the reduced symmetry of these devices. The additional phase and alignment noise due to geometry changes can indeed set limitations to sensitivity of future detectors implementing diffractive optics whilst demanding more stringent alignment and control requirements of the suspended optics.

The remainder of this section will summarise the theoretical framework to describe the asymmetry of grating devices used as input couplers to cavities

and the associated dynamic affects on grating motion and alignment.

3.7.1   Relative Grating and Input Beam Alignment

The direction of the outgoing diffracted light from a grating is dependent on the grating orientation in relation to the input beam. Figure 3.19 illustrates a three port grating in second order Littrow mount as used in this experiment along with the required coordinate system that will be described. Here the grating is located in the $x - y$ plane, with the input beam located in the $x - z$ plane only and the grating grooves aligned parallel to the y axis. The input beam can be represented by a vector $\mathbf{a}$, while the outgoing beams can be denoted by $\mathbf{b}_m$. In order to describe the effects resulting from changes to the alignment of the grating and input beam it is useful to denote the coordinate system of the input beam using the notation (x', y', z') and likewise that of the output beams using (x''_m, y''_m, z''_m) as indicated by Figure 3.19. The relationship between the input and output angles, relative to the grating normal, α and β_m respectively, can be described by the grating equation

$$\sin \alpha + \sin \beta_m = \frac{m\lambda}{d}, \tag{3.21}$$

where m is the order of diffraction, λ is the wavelength of the light and d is the grating period. By analogy, the vector form of the grating equation can be written as

$$\mathbf{b} \times \mathbf{N} + \mathbf{a} \times \mathbf{N} = \frac{m\lambda}{d}\mathbf{G}, \tag{3.22}$$

where $\mathbf{N}$ represents the grating normal vector aligned along the z axis and $\mathbf{G}$ represents the grating unit vector aligned to the y axis.

There are three degrees of freedom for changing the relative alignment between the grating and the input beam that will be described independently.
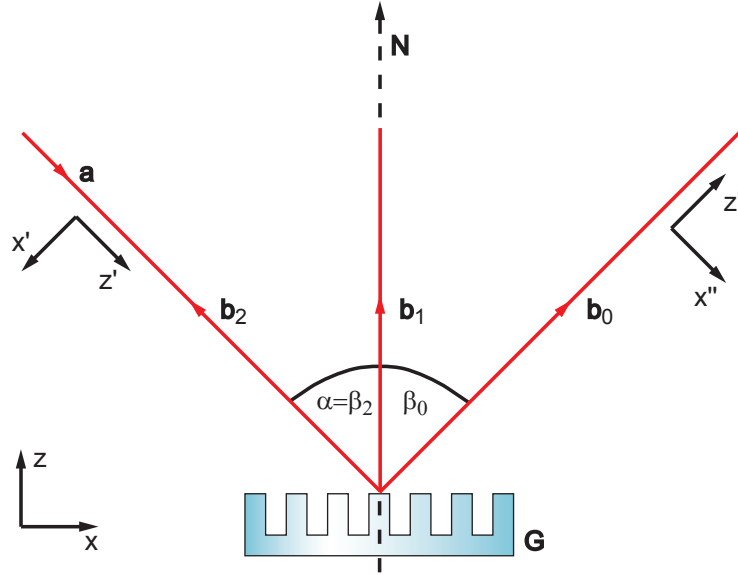
Figure 3.19: *Illustration of a three port grating in second order Littrow mount, indicating the input vector* **a** *and output vectors* **b**$_0$,**b**$_1$, *and* **b**$_2$. *The grating unit vector* **G** *is aligned out of the page and the grating normal vector* **N** *is aligned along the z axis.*

Roll Alignment

Using Equation 3.22 it can be shown that rotation of the grating around the z axis by a small angle θ (see Figure 3.20), given the unit vector $\mathbf{G} = (\sin\theta, \cos\theta, \mathbf{0})$, results in the output beam rotating around the x'' axis, also known as *pitch*, by an amount

$$\delta \approx \frac{m\lambda}{d}\theta. \tag{3.23}$$

Furthermore it can be shown that the corresponding change in the output beam angle is represented by

$$\Delta\beta \approx \frac{-m\lambda}{d}\frac{\theta^2}{2\cos\beta_m}. \tag{3.24}$$

Thus *roll* motion of the grating will change the *pitch* and the output angle of the outgoing beam, hence the loss of symmetry when compared to mirrors.
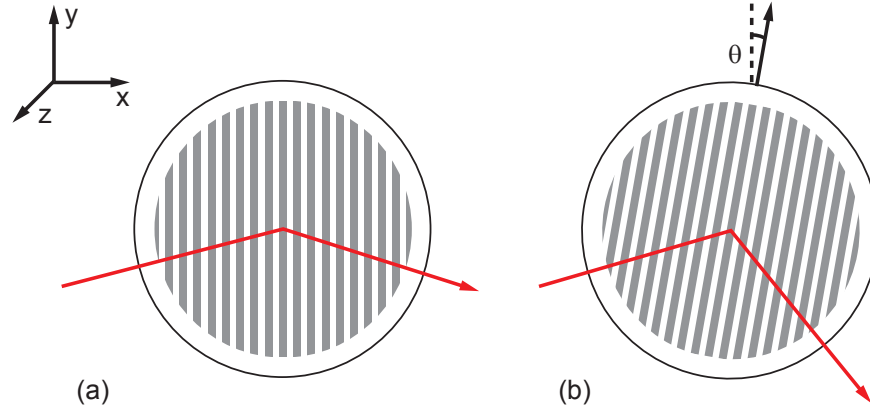
Figure 3.20: *Illustration of (a) a diffraction grating with the grating grooves aligned along the y axis and (b) the grating rotated around the z axis (out of the page) by a small angle θ causing the output beam to be rotated in pitch and yaw compared to (a).*

Pitch Alignment

When considering the rotation of the grating around the x axis, *pitch* of the grating, this is precisely equal to considering the pitch of the input beam relative to the grating, in other words rotation of the input beam around the x' axis as indicated by Figure 3.19. It has been shown that a change in the pitch angle δ' will give rise to a change in the output angles of the diffracted beams [44], described by

$$\Delta\beta_m \approx \frac{m\lambda}{d}\frac{\delta'^2}{2\cos\beta_m},$$
(3.25)

and

$$\delta' = \delta''_m.$$
(3.26)

Yaw Alignment

As with pitch alignment, when considering changes of the grating around the y axis, known as *yaw* alignment, this is analogous to changes of the input beam around the y axis. It can be shown that changes of input angle $\Delta\alpha$ around the y' axis will change the angle of the diffracted orders [44], described by

$$\Delta\beta_m = \frac{-\cos\alpha}{\cos\beta_m}\Delta\alpha, \qquad (3.27)$$

and

$$\delta_m'' = 0. \qquad (3.28)$$

Furthermore, there is also an additional factor, which is not related to the grating alignment, that causes changes to the output beam angles. From the grating equation (3.21) it can be seen that changes to the laser frequency (and wavelength) will cause changes to the output alignment, thus it can be shown

$$\Delta\beta_m = \frac{-m\lambda}{d\cos\beta_m}\frac{\Delta f}{f}. \qquad (3.29)$$

3.7.2 Translational Motion Between Grating and Input Beam

Along with the three rotational degrees of freedom, there are three translational degrees of freedom in which the grating can move, and the corresponding effects to the optical path length (and therefore phase) of the output beams shall be summarised.

Translation along y axis

Translational motion of the grating or the input beam along the y axis affects neither the alignment or phase of the diffracted output beams. Only translational changes along the x axis or the z axis will result in changes to the optical path length ζ of the mth order diffracted beam. Translation along the z axis results in the effects from translation along the x axis also, however, to summarise the basic behaviour, combined effects have been omitted here.

Translation along z axis

In order to demonstrate the effects resulting from z translation it is useful to consider just one input vector $\mathbf{a}$ as it interacts with the grating surface and one output vector $\mathbf{b}$. From the basic geometry illustrated in Figure 3.21, it is possible to observe that translation of the grating Δz along the z axis results in an optical path length difference described by

$$\zeta_{\Delta z} = \zeta_1 + \zeta_2 = -\Delta z(\cos \alpha + \cos \beta_m). \qquad (3.30)$$

Since translation of the grating along the *negative* z axis must result in a *positive* optical path length change, this demands the minus sign indicated in Equation 3.30.

Translation along x axis

When considering the translation of the grating along the x axis, it is also equivalent to consider the x axis translation of the input beam with respect to the grating as indicated by the geometry shown in Figure 3.22. The change in optical path length of the mth order diffracted beam $\zeta_{\Delta x}$ is therefore related
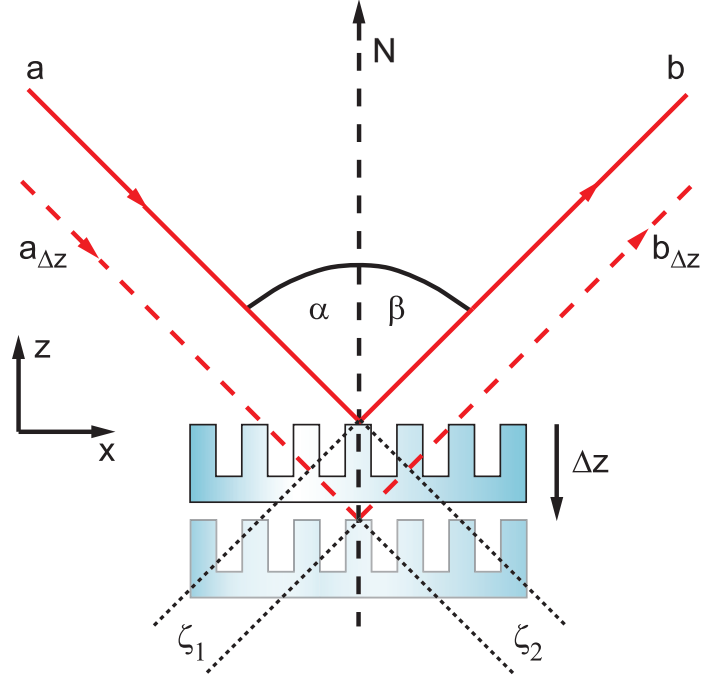
Figure 3.21: *Illustration of a diffraction grating translated along the z axis. Input and output vectors $\mathbf{a}_{\Delta z}$ and $\mathbf{b}_{\Delta z}$ have acquired an additional optical path lengths ζ_1 and ζ_2 in comparison to $\mathbf{a}$ and $\mathbf{b}$ respectively. The additional optical path length gained corresponds to a change of relative phase on the output vector.*

to the translational grating displacement Δx by

$$\zeta_{\Delta x} = \zeta_4 - \zeta_3 = -\Delta x(\sin\alpha + \sin\beta_m) = -\Delta x\frac{m\lambda}{d}. \qquad (3.31)$$

It is worth noting that due to the symmetrical periodic nature of the grating, the changes in optical path length must also be periodic for x axis translations of $0 < \Delta x < nd$, where n represents an integer. Therefore Equation 3.31 is defined for translation changes of less than one grating period. The corresponding phase shift ϕ associated to the change in optical path length can be represented by

$$\Delta\phi = \zeta_{\Delta x}\frac{2\pi}{\lambda}. \qquad (3.32)$$
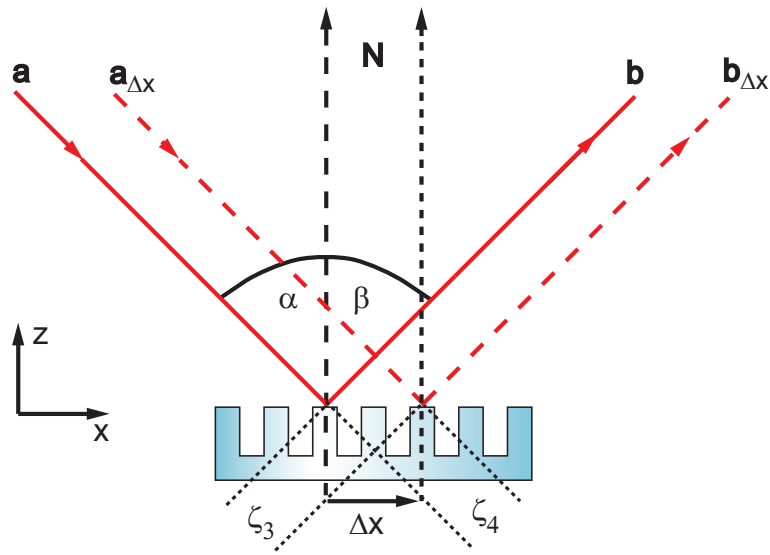
Figure 3.22: *Illustration of a diffraction grating translated along the x axis. Input and output vectors $\mathbf{a}_{\Delta x}$ and $\mathbf{b}_{\Delta x}$ have acquired additional optical path lengths ζ_3 and ζ_4 in comparison to $\mathbf{a}$ and $\mathbf{b}$ respectively. The additional optical path length gained corresponds to a change of relative phase on the output vector.*

By driving the grating sinusoidally across the beam (along the x axis), the phase of the diffracted beams will therefore be modulated. Optical systems that exhibit phase shifting effects in this way are already well known [53] and commonly utilised in acousto-optic modulators, where an acoustically generated travelling grating is used to change the frequency of a light beam.

3.8 Coupling of Translational Grating Motion to Output Signals

3.8.1 Theoretical Analysis

Theoretical investigations of the coupling of lateral grating displacement to all output ports of a diffractively coupled optical cavity [61] used frequency-domain analysis to derive the expected electric field responses. It was shown that the complex field amplitude arriving at the forward-reflected port (c3) (as indicated in Figure 3.16) generated in the prescribed modulating system can be defined by

$$a_3 = ip_0\eta_1^2 e^{-2i\phi_1}\frac{\pi\Delta x}{d}\rho_2\left(\frac{e^{-2ik_uL}}{1 - \rho_0\rho_1 e^{-2ik_uL}} - \frac{e^{-2ik_cL}}{1 - \rho_0\rho_1 e^{-2ik_cL}}\right),\qquad (3.33)$$

where p_0 represents the complex amplitude of the input carrier field, k_u is the wave-number of the upper sideband caused by lateral grating motion, k_c is the wave-number of the carrier field and L indicates the cavity length. A similar expression can be written for the lower sideband caused by lateral grating motion where the upper sideband wave number terms are replaced with the lower sideband wave number k_l. The first term inside the brackets in Equation 3.33 defines the phase evolution of the upper sideband field and is approximately constant while the frequency of motion is below the linewidth of the cavity. This means that the lateral grating motion will result in an f response to displacement compared to the flat frequency response generated by longitudinal motion.

With the diffractively coupled cavity system fully characterised and locked to the operating point using the transmitted port output signal, it was decided to validate these theoretical predictions experimentally, as will be discussed.

3.8.2 Experimental Demonstration of Lateral Grating Motion Coupling to Output Signals

Using the three global control electromagnetic actuators positioned to the rear of the test mass and installing a fourth at the side of the test mass perpendicular to the centre of mass it was possible to deliberately inject grating motion both along the cavity axis (longitudinal) and perpendicular (translational). By monitoring the forward-reflected output signal (c_3) it was possible to demonstrate the effects associated with translational grating motion. It is worth noting that the grating axis was chosen to be vertical because it is difficult to shake the pendulum in this direction.

When the grating is static, the forward-reflected output signal contains the upper and lower radio frequency sidebands (both at $10\,\mathrm{MHz}$) undergoing zeroth order diffraction, and the carrier field, which has experienced first order diffraction twice (coupling *in* and *out* of the cavity).

When the grating is undergoing sinusoidal translational grating motion, the forward-reflected output signal still contains the same three frequency components, however the carrier field that has undergone $|m| = 1$ diffraction twice will also acquire lateral motion induced modulation.

Two methods for testing the coupling of lateral grating motion to the forward-reflected port were devised. Figure 3.23(a) indicates method (a) for nearly pure translational injection, where large driving signals are applied to the coil 4 and small driving signals are applied to coils $1-3$ in order to remove residual longitudinal motion. While Figure 3.23(b) indicates method (b) for rotating the test mass around the centre of mass (parallel to the incident beam) by applying large driving signals to coils 1 and 2 causing translational motion of the front surface.
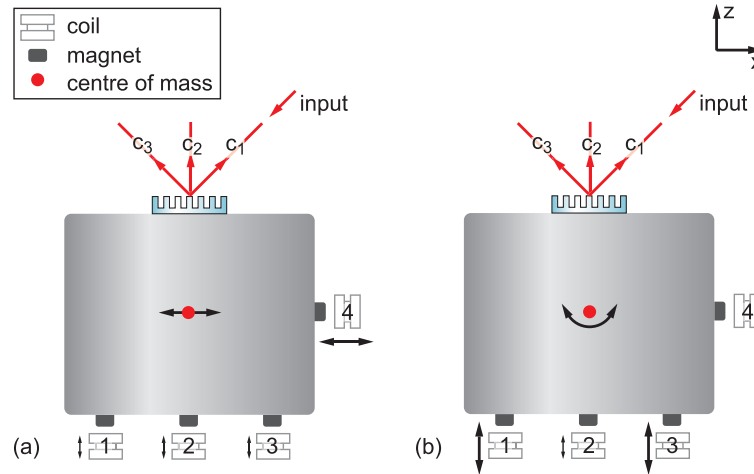
Figure 3.23: *Driving translational grating motion using coil-magnet actuators.
(a) pure side-to- side motion produced by actuating from the side and correcting
for any additional twisting motion using the rear coils, (b) rear coil actuation
drives the mass rotationally causing lateral motion of the front surface. In
the second case the small signal from longitudinal motion is dominated by the
larger translational signal produced.*

When injecting a fixed amplitude driving signal from a spectrum analyser in
method (a), the displacement Δx of the suspended test mass was measured
independently using a commercial vibration sensor (Polytec OFV 505 Vibrom-
eter). The vibration sensor was positioned inside the vacuum system and
optimised for sensing position changes of the test mass stage along the x-axis.
The forward reflected error signal (c3) was aligned onto a photodiode outside
of the vacuum system using a steering mirror, from which the signal could be
demodulated.

Using the spectrum analyser it is possible to inject sinusoidal signals through
the side mounted coil (coil 4 in Figure 3.23) and thus motion of the test mass
along the x-axis, whilst monitoring the frequency response of the forward-
reflected error signal. The measured frequency response is provided in Figure
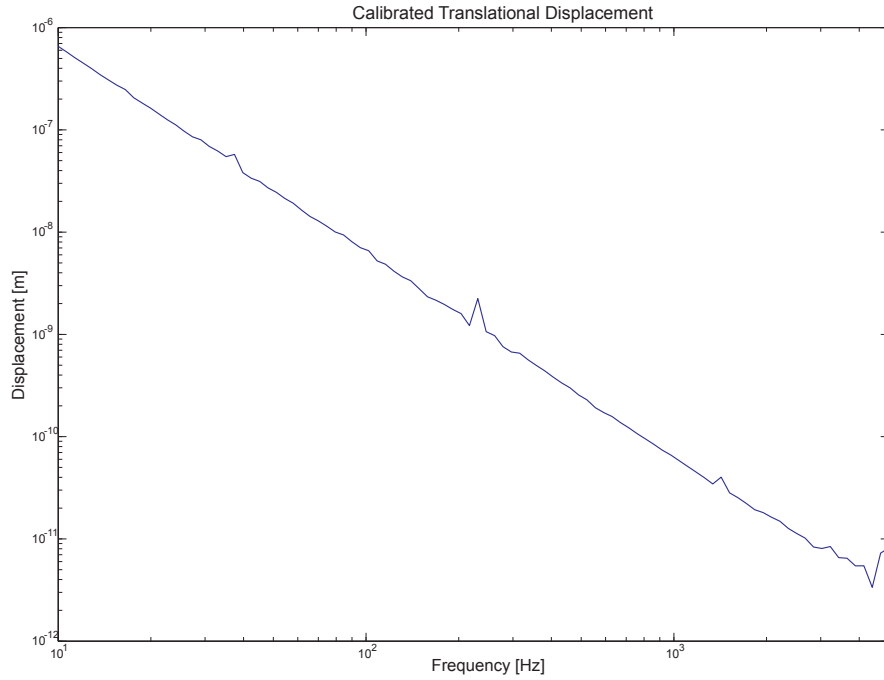
Figure 3.24: *Measured translational grating motion injected primarily using coil-magnet actuator (4) located at test mass side. A distinct $1/f^2$ frequency response expected for a freely suspended mass is observed. This data can be used to infer the predicted coupling response of lateral grating motion to the forward-reflected port defined by Equation 3.33.*

3.24 and the expected $1/f^2$ response is observed. This calibrated measurement is required to predict the strength of the amplitude signals obtained at the forward-reflected port for injected translational grating motion based on Equation 3.33.

When injecting motion onto the grating using both methods the response of the forward-reflected output signal was monitored on a $10\,\text{MHz}$ tuned photodetector and subsequently demodulated. Figure 3.25 shows the response of the forward-reflected signal amplitude to translational motion, the predicted response, and the response to longitudinal motion for comparison. It can be

seen that pure x translational motion agrees with the predicted response until approximately $300\,\mathrm{Hz}$, at which point the slope begins to rise due to an internal resonance of the cylindrical aluminium test mass to which the grating is mounted [62]. The internal resonance was confirmed using the finite element analysis package, Ansys [63], and monitoring the excited modes of an identical aluminium mass using an accelerometer. When rotating the test mass as in method (b) the internal resonance is no longer excited, giving a larger frequency span for monitoring the response, however smaller translational motion is achieved compared to method (a) as indicated by the reduced signal amplitude. Both driving methods verify the $1/f$ response to translational grating motion compared to the typical $1/f^2$ response for longitudinal driving.

3.9 Conclusions

In conclusion, we have constructed a triple-suspended diffractively-coupled FabryPérot cavity within the Glasgow $10\,\mathrm{m}$ prototype interferometer and developed a numerical model for the system. From the simulation we were able to investigate the use of conventional techniques for length sensing and control signal extraction from a diffractively coupled Fabry-Pérot cavity. Our experimental results in Section 3.6 provided both qualitative and quantitative verification of the theoretical framework supporting grating coupled interferometers. Additionally, it was possible to adapt the numerical model to show the extent of asymmetry in both reflected demodulated signals and furthermore reconstruct a symmetrical PDH signal with these signals, irrespective of their shape.

We demonstrated the effect of translational grating motion coupling into the length sensing signal from a diffractively coupled cavity observing a charac-
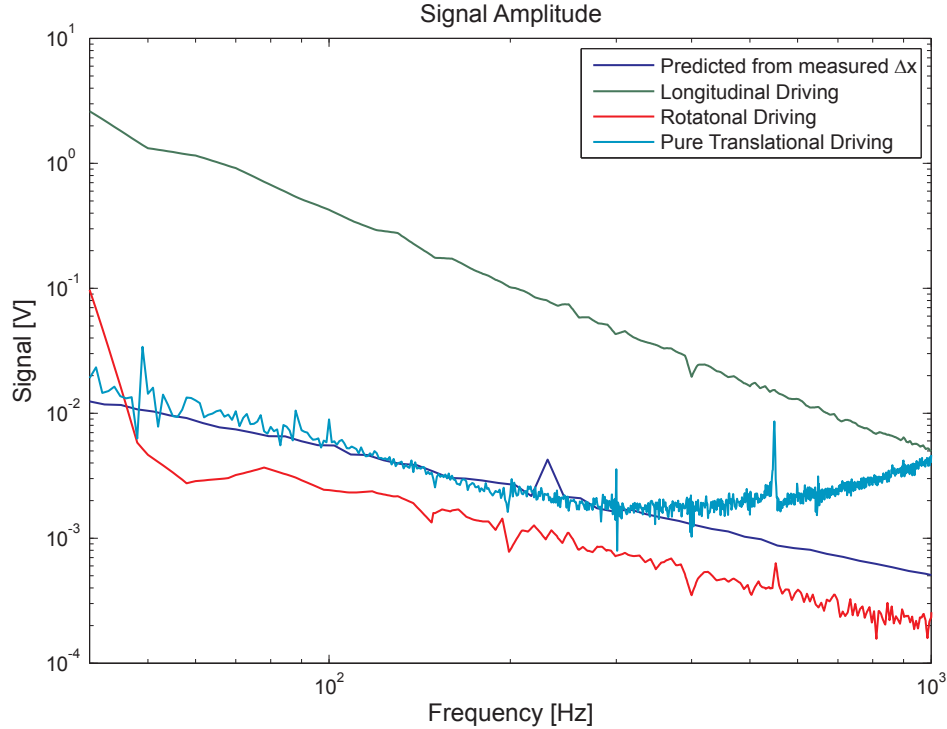
Figure 3.25: *Predicted and measured signal responses at port c3 for several grating motions. The theoretical response is calculated using Equation 3.33, known cavity parameters and the measured displacement from Figure 3.24. The longitudinal signal response is $1/f^2$ as would be expected from a conventional cavity topology. The pure-translational and rotational signals (driving methods (a) and (b) respectively) demonstrate clear $1/f$ responses. Above $300\,\mathrm{Hz}$ the pure-translational signal is dominated by an internal resonance of the test mass mounting the diffractive coupler.*

teristic $1/f$ slope in the signal response thus validating the theoretical predictions. An internal resonance dominated the signal response at frequencies above $300\,\mathrm{Hz}$ and although this is far lower in frequency and broader than would be expected for a gravitational wave interferometer mirror mass, it highlights an unavoidable coupling between internal vibrations and motion of the grating surface when dealing with diffractively coupled cavities, particularly

since translational grating signal responses are proportionally larger by a factor of the Fourier frequency than longitudinal signals. At low frequency the signal obtained has a far smaller response than that observed for an equivalent longitudinal length change but becomes more significant at higher frequencies. Additionally, the magnitude of the coupling will depend on the grating properties and the length of the cavity such that a longer cavity will produce greater coupling.

Chapter 4

Optomechanical Behaviour in a Suspended Coupled Fabry-Pérot Cavity

Thus far I have highlighted research efforts into an alternative technology and topology to mitigate sources of noise from future gravitational wave detectors when the intra-cavity power is increased. Meanwhile, with the advent of second generation detectors, such as Advanced LIGO, and all associated enhancements, the sensitivity is expected to improve by more than an order of magnitude [64] revealing fundamental noise limitations that arise from the measurement process. The quantum noise of such detectors is comprised of shot noise at high frequencies and radiation pressure force acting on the mirrors at low frequencies as illustrated in Figure 4.1. The radiation pressure acting on the suspended mirrors of optical cavities will become a dominant force in high-power regimes, modifying the mechanical dynamics of the pendulums. Opto-mechanical coupling is a well known effect [19, 65]. It has been
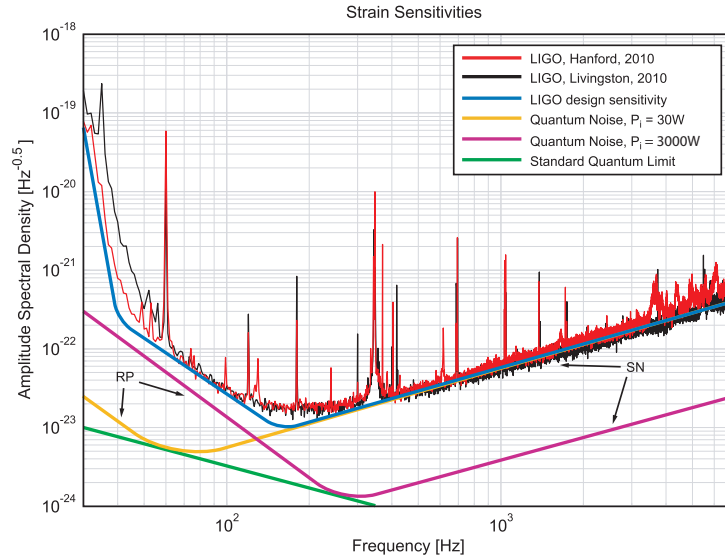
Figure 4.1: *Amplitude spectral density of the strain detectable for the LIGO detectors. Typical sensitivity observed in* 2010 *is illustrated in black and red, along with the design sensitivity indicated in blue. The quantum noise is illustrated for the current level of input power (yellow) and for an increase of* 100 *times (purple). The Standard Quantum Limit shown in green outlines the minimum noise achievable when the Shot Noise (SN) at high frequencies and Radiation Pressure noise (RP) at low frequencies are uncorrelated.*

proposed for use in future gravitational wave detectors to increase the narrow-band sensitivity [66, 67]. It is therefore important to gain practical experience in the control of coupled cavity systems whose dynamics are dominated by optical rigidity and to explore this in the context of typical suspended-optics interferometers.

In this Chapter I investigate the fields and forces upon the mirrors of a suspended Fabry-Pérot cavity and derive their dynamic behaviour numerically. By revealing the conditions for which radiation pressure forces induce optomechanical rigidity, I detail the design process behind the optical spring ex-

periment at Glasgow. The theoretical foundations used herein are later implemented in a numerical model in order to characterise the observed system dynamics under experimental conditions.

4.1 Field Equations for a Static Fabry-Pérot Cavity

The light fields of a suspended two-mirror cavity system are illustrated by Figure 4.2. The external fields are the incident light field E_i, the reflected field E_r comprising of the light that has reflected directly from the input mirror and superimposed with the leaked cavity field through the input mirror, and the transmitted field E_t generated by the cavity field that leaks through the end mirror. The circulating internal field can be considered using the light directly after the input mirror E_{c1} and end mirror E_{c2} as illustrated. $E_{c1'}$ and $E_{c2'}$ indicate the cavity fields after traversing one cavity length L. We write the reflected field as

$$E_r = \tau_a E_{c2'} + \rho_a E_i e^{-2i\phi} \tag{4.1}$$

and the transmitted field by

$$E_t = \tau_b E_{c1'}. \tag{4.2}$$

The internal fields can be described using the same procedure as in Chapter 3, to show

$$E_{c1} = E_i i\tau_a + E_{c2'}\rho_a, \tag{4.3}$$

$$E_{c1'} = E_{c1}e^{-i\phi} = E_i i\tau_a e^{-i\phi} + E_{c2'}\rho_a e^{-i\phi}, \tag{4.4}$$

$$E_{c2} = E_{c1}\rho_b e^{-i\phi}, \tag{4.5}$$

$$E_{c2'} = E_{c2}e^{-i\phi} = E_{c1}\rho_b e^{-2i\phi}. \tag{4.6}$$
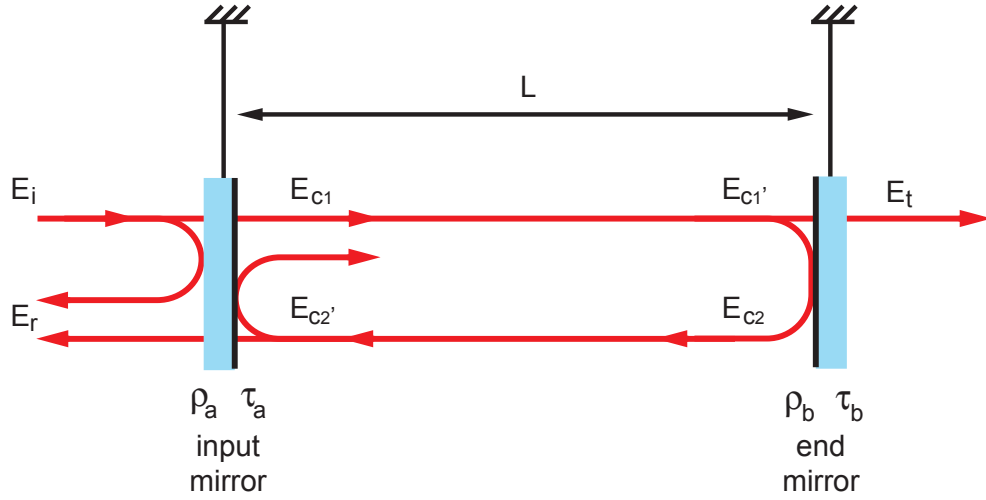
Figure 4.2: *Schematic diagram of a simple optical cavity showing the incident light field E_i interacting with the input mirror giving the cavity fields $E_{c1,c2}$ ($E_{c1',c2'}$ have gained an additional phase component due to traversing the length of the cavity). The cavity field leaks light through the input mirror and superimposes with the directly reflected light to produce a reflected light field E_r, as well as the light leaking through the end mirror to produce a transmitted field E_t.*

It is more useful to describe a single internal field with one equation, thus by assuming the cavity mirrors to be static and the input light amplitude to be constant ($E_i(t) = A$), we write the forward propagating cavity field, E_c, as

$$E_c = A\tau_a + E_c\rho_a\rho_b e^{-2i\phi}, \tag{4.7}$$

for which the solution is

$$E_c = \frac{A\tau_a}{1 - \rho_a\rho_b e^{-2i\phi}}. \tag{4.8}$$

The reflected field can be written as

$$E_r = A\rho_{ab}, \tag{4.9}$$

where ρ_{ab} indicates the static reflectivity of the cavity as seen by the incoming light, defined

$$\rho_{ab} = \rho_a - \frac{\tau_a^2 \rho_b e^{-2i\phi}}{1 - \rho_a \rho_b e^{-2i\phi}}. \tag{4.10}$$

We have therefore shown that the reflectivity of a static Fabry-Pérot cavity is a function of the detuning phase, and can be used effectively as a mirror with variable reflectivity for monochromatic light as experimentally demonstrated on an earlier Glasgow prototype[42].

Similarly, we can express the transmitted field as

$$E_t = E_c \tau_b e^{-i\phi}, \tag{4.11}$$

which can also be written as

$$E_t = \frac{A \tau_a \tau_b e^{-i\phi}}{1 - \rho_a \rho_b e^{-2i\phi}}. \tag{4.12}$$

Hence, the transmitted field is directly proportional to the cavity field, and is often used to determine the stored power.

The maximum amplitude of the cavity field 4.8 can be simplified to

$$E = g_{ab} A, \tag{4.13}$$

where g_{ab} represents the maximum amplitude gain of the Fabry-Pérot cavity defined by

$$g_{ab} = \frac{\tau_a}{1 - \rho_a \rho_b}. \tag{4.14}$$

4.2 Power Coupling in a Fabry-Pérot Cavity

For the static solution, the stored power (intensity) can be expressed using the Airy intensity profile [68] as

$$P = |E|^2 = g_{ab}^2 P_{in} \frac{1}{1 + F \sin^2 \theta}, \tag{4.15}$$

where $P_{in} = |A|^2$, θ is the cavity tuning and F is the coefficient of finesse defined by

$$F = \frac{4\rho_a\rho_b}{(1 - \rho_a\rho_b)^2};$$ (4.16)

where $\mathcal{F}$ is the cavity finesse. We see from Equation 4.15 that the resonances of a Fabry-Pérot cavity correspond to when the Airy intensity profile is unity:

$$\theta = n\pi$$ (4.17)

The FSR is the frequency separation between successive resonances and is defined by

$$\Delta\omega = 2\pi\frac{c}{2L} = \frac{\pi c}{L},$$ (4.18)

where c is the speed of light in vacuum, and L is the cavity length. The FSR of the Glasgow $10\,\text{m}$ prototype is approximately $2\pi(15.2\,\text{MHz})$.

The finesse, which is a measure of the quality of the cavity, can be defined by the FSR and the resonance linewidth $\gamma_{\omega,\theta}$, given by

$$\mathcal{F} = \frac{\Delta\omega}{\gamma_\omega} = \frac{\pi}{\gamma_\theta},$$ (4.19)

where the cavity linewidth is expressed in frequency γ_ω or tuning γ_θ and is defined as the Full Width at Half Maximum (FWHM) of the resonance, as illustrated in Figure 4.3. The finesse can also be evaluated based on the amplitude reflectivities of the cavity mirrors, given by

$$\mathcal{F} = \frac{\pi\sqrt{F}}{2} = \frac{\pi\sqrt{\rho_a\rho_b}}{1 - \rho_a\rho_b}.$$ (4.20)

Figure 4.3 illustrates the normalised intracavity power defined by Equation 4.15 as a function of angular frequency.
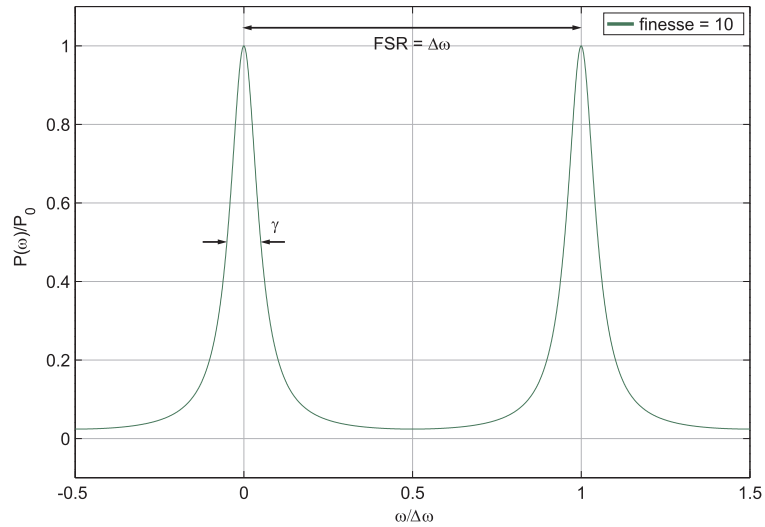
Figure 4.3: *Illustration of the intracavity power as a function of angular frequency based on the Airy intensity profile. The FSR, $\Delta\omega$, between successive resonance's is shown, along with the linewidth γ (FWHM).*

4.3 Field Equations for a Three-Mirror Coupled Cavity

Our previous analysis of the fields in two mirror Fabry-Pérot cavities can be expanded upon in the context of three mirror coupled cavity systems. As mentioned in Chapter 1, these assemblies are used to recycle light leaking from the longer arm cavities and maximise the time spent by the fields within the interferometer to improve detector sensitivity. At Glasgow a three mirror coupled cavity system was employed throughout our investigations into optomechanical dynamics and it is therefore useful to describe the relevant equations for the fields in such systems.

An additional mirror c is included between the laser and the input mirror from the earlier analysis. All three mirrors share the same optical axis and the
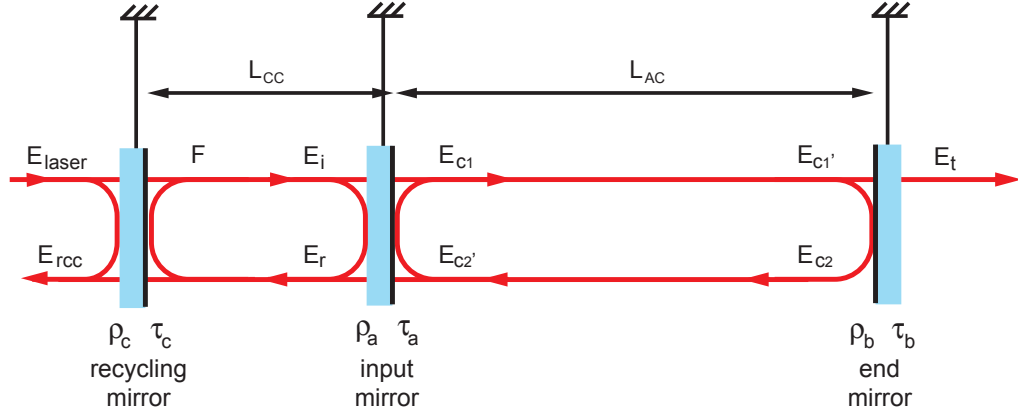
Figure 4.4: *Schematic diagram of two co-aligned cavities coupled together by the input mirror. The input field here is that of the laser E_{laser}, which interacts with the recycling mirror to give a reflected field E_{rcc} (including the external cavity field transmitted through the recycling mirror) and the transmitted field F (including the reflected external cavity field). The input light to the internal cavity is E_i.*

reflection coatings are located as indicated by Figure 4.4. The cavity formed between mirror c and mirror a is referred to herein as the *external* cavity, while the *internal* cavity is that formed between mirror a and mirror b.

If we first consider the case when there is no mirror motion, the internal cavity can be treated as before with the transmitted, reflected, and cavity fields being described by Equations 4.12, 4.9 and 4.8 respectively. However, the incident field is now generated inside the external cavity rather than the laser. Using the same procedure as before, we can describe the forward propagating external cavity field by

$$F = E_{laser}\tau_c - \rho_c\rho_{ab}Fe^{-2i\varphi}, \tag{4.21}$$

where φ is the phase acquired after traversing the external cavity length l. The

solution to 4.21 is shown to be

$$F = \frac{\tau_c A}{1 + \rho_c \rho_{ab} e^{-2i\varphi}}.$$

(4.22)

Therefore the incident field on mirror a is given by

$$E_i = F e^{-i\varphi}.$$

(4.23)

Thus we can write the internal cavity field as

$$E = \frac{\tau_a F e^{-i\varphi}}{1 - \rho_a \rho_b e^{-2i\phi}},$$

(4.24)

which expands to

$$E = A \left(\frac{\tau_c}{1 + \rho_c \rho_{ab} e^{-2i\varphi}} \right) \left(\frac{\tau_a e^{-i\phi}}{1 - \rho_a \rho_b e^{-2i\phi}} \right).$$

(4.25)

The first term in brackets corresponds to the amplification of light in the external cavity and the second term in brackets is that of the internal cavity. For resonance to occur in the internal cavity the following phase condition must be met:

$$\phi = n\pi,$$

(4.26)

where n is an integer. And since $e^{2ni\pi} = 1$, the phase components of the internal field in 4.25 can be omitted. The resonance condition of the external cavity depends on the state of the internal cavity, such that

$$\varphi = \pi \left(m + \frac{1}{2} + \frac{arg(\rho_{ab})}{2\pi} \right).$$

(4.27)

When the internal cavity is exactly on resonance, the reflectivity ρ_{ab} is real and the phase condition is then written

$$\varphi = \pi m + \frac{\pi}{2}.$$

(4.28)

4.4 Power Coupling in a Three-Mirror Coupled Cavity

It is considered optimal coupling when there is maximum power in the internal cavity. We define the static power by

$$P_{int} = |E|^2 = \left| \frac{\tau_c}{1 + \rho_c \rho_{ab} e^{-2i\varphi}} \right|^2 \left(\frac{\tau_a}{1 - \rho_a \rho_b} \right)^2 P_{laser}. \tag{4.29}$$

Thus by ensuring the external cavity is exactly on resonance and static, Equation 4.29 can then be expressed, similarly to 4.15 in terms of the internal cavity phase offset, as

$$P_{int} = g_{ca}^2 g_{ab}^2 P_{laser} \frac{1}{1 + F_c \sin^2 \theta}, \tag{4.30}$$

where g_{ca} and g_{ab} are the amplitude gains of the external and internal cavities respectively, and F_c is the coefficient of finesse for the coupled cavity system. When the internal cavity is exactly on resonance, corresponding to $\phi = 0$, the end term in Equation 4.30 becomes unity and we obtain the maximum cavity power,

$$P_0 = g_{ca}^2 g_{ab}^2 P_{laser}. \tag{4.31}$$

The optimal power coupling occurs when both of these factors are maximised for which there are three possible modes:

1. $\rho_{ab} = 0$. The internal cavity is optimally coupled with no light reflected and the amplitude gain would be determined as $g_{ca} = \tau_c$.

2. $\rho_{ab} < 0$. The internal cavity is termed overcoupled, meaning the resonance of light in the external cavity takes place when $\varphi = m\pi$.

3. $\rho_{ab} > 0$. The internal cavity is undercoupled so that the resonance of light in the external cavity occurs when $\varphi = m\pi + \frac{\pi}{2}$.

To understand the significance of the above three conditions it is important to consider the length of the arm cavities in current ground based detectors. The arm cavity length leads to fixed transit time T for the light propagating inside. Similarly, for a given detection bandwidth, there exists and optimum storage time τ, which is also a fixed parameter. The fixed storage time places a limit on the allowed reflectivities of the cavity mirrors, defined by [68]

$$\rho_a \rho_b = e^{-2T/\tau} = \text{constant.} \tag{4.32}$$

To ensure maximum gain in the arm cavity, the transmissivity of the end mirrors in the LIGO detectors, for example, are very low (typically $\tau_b = 20\,\text{ppm}$). Thus, from Equation 4.32, we see that the choice of end mirror constrains the choice of reflectivity for the input mirror. In many cases, it is found that the resulting cavity is not optimally coupled to the input light. Therefore the use of an additional mirror in front of this cavity forms a recycling cavity, whose reflectivity can be selected to match the internal arm cavity reflectivity ρ_{ab}, given by

$$\rho_c = (1 - \mathcal{L})|\rho_{ab}|, \tag{4.33}$$

such that the total reflectivity of the coupled cavity ρ_{cab} can reach zero, and thus maximum transmission of light into the system is achieved.

We see from 4.29 that the external cavity acts essentially as an additional source of power gain, and if controlled appropriately it is effectively decoupled from the internal cavity. This is particularly the case if, as in our experiment, the finesse of the internal cavity is much higher than that of the external cavity. Even if the external cavity is not precisely on resonance, the effect of this on the fields in the internal cavity is small. The details of the control of the three mirror coupled cavity is covered later. For simplicity we will ignore the external cavity and consider only the internal cavity for calculating the equations of motion for suspended mirror, as this cavity is of primary interest.

4.5   Suspended Mirror Equations of Motion

Two theoretical methods have been considered by the author to describe the equations of motion for a suspended mirror. The Lagrangian technique uses an energy method to determine the equations of motion and results in an arguably more elegant and concise solution when compared to state-space modelling, which utilises linear first order differential equations. However, numerical software packages such as MATLAB [57] are better suited to model problems designed in state space form. Therefore in this analysis we consider the Lagrangian formulation to obtain concise equations of motion, and then by applying Laplace transformation it is possible to describe the mirror motion in matrix form for use in numerical simulation packages.

We begin by considering the six degrees of freedom for a suspended mirror. There are three translational degrees of freedom along the x, y, and z axes, in addition to three rotational degrees of freedom ζ, ψ, and ϕ about each axis respectively, as illustrated in Figure 4.5. However, not all degrees of freedom have consequences on the reflection of light from the surface. Rotations along ζ, and translations along z and y axes can therefore be neglected for light propagating along the x axis. For clarity we term motion along the remaining degrees of freedom x, ψ, and ϕ as *longitudinal*, *pitch* and *yaw* respectively. In general, the design of a mirror suspension is symmetrical about the xz-plane, therefore yaw motion is decoupled from longitudinal and pitch motion. Additionally, the mirror is typically suspended from four symmetrically spaced wires separated in x and y, resulting in direct coupling between *longitudinal* and *pitch* motion. Thus, there are primarily just two independent motions of concern; *planar* motion along the x-axis and *yaw* motion, which will herein be described.
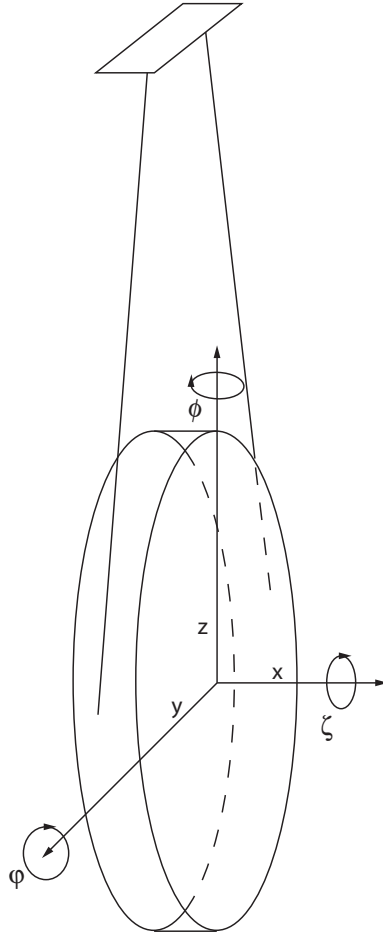
Figure 4.5: *Schematic diagram of a suspended mirror indicating the three translational degrees of freedom (x,y,z) and the three rotational degrees of freedom about each axis (ζ,ψ,ϕ).*

The Lagrangian of the suspended system is defined to be the kinetic energy minus the potential energy,

$$\mathcal{L} = K - P. \tag{4.34}$$

The kinetic and potential energies are expressed in terms of the coordinates of the system, q_i, which exist for each degree of freedom and in our case represent x, ψ and ϕ. By obtaining the Lagrangian for the two aforementioned independent motions, the equations of motion can then be described by the
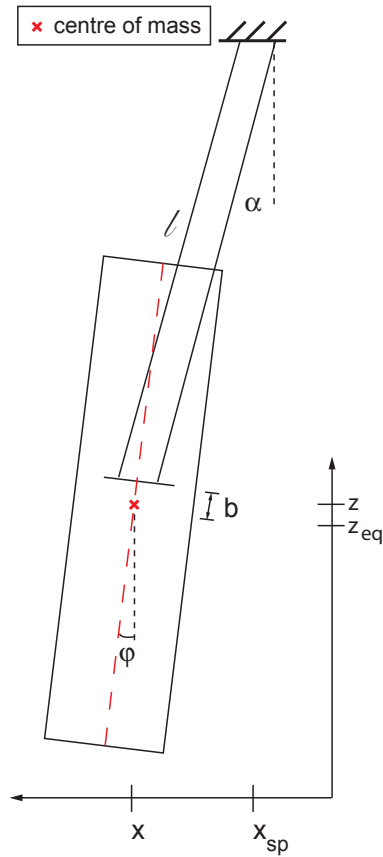
Figure 4.6: *Schematic diagram of a suspended mirror acted upon by planar motion, moving a distance $x - x_{sp}$ from the equilibrium suspension point, and the centre of mass (highlighted by a red cross) has risen to z. The wire length is denoted l, the separation between the break-off and centre of mass is denoted by b. The suspension wires are at an angle α, whilst the mirror pitch is given by ψ.*

Euler-Lagrange equation,

$$\frac{d}{dt}\left(\frac{\partial \mathcal{L}}{\partial \dot{q}_i}\right) = \frac{\partial \mathcal{L}}{\partial q_i}. \tag{4.35}$$

When the mirror is acted upon by *planar* motion, as illustrated in 4.6, we describe the resulting change in coordinates for the mirror centre of mass

$(x,0,z)$ as,

$$x = x_{sp} + l\sin\alpha + b\sin\psi \approx x_{sp} + l\alpha + b\psi, \tag{4.36}$$

$$z = l + b - l\cos\alpha - b\cos\psi \approx \frac{l\alpha^2}{2} + \frac{b\psi^2}{2}, \tag{4.37}$$

where x_{sp} denotes the x position of the suspension point, l denotes the wire length, b denotes the wire break-off point above the centre of mass, and α represents the angle of the suspension wires to the vertical. It is worth noting that we have made the small angle approximation. Furthermore, we can eliminate one variable by substituting for

$$\alpha = \frac{1}{l}\left(x - x_{sp} - b\psi\right), \tag{4.38}$$

to describe the elevation of the centre of mass as,

$$z = \frac{(x - x_{sp} - b\psi)^2}{2l} + \frac{b\psi^2}{2}. \tag{4.39}$$

When the mirror is acted upon by *yaw* motion, as illustrated in 4.7, we describe the resulting change in coordinates for the mirror centre of mass $(0,0,z')$, where $z' = (z - z_{eq})$, by first defining the projection of the wire onto the xy-plane as

$$d^2 = R_1^2 + R_2^2 - 2R_1 R_2 cos(\phi - \phi_{sp}), \tag{4.40}$$

where R_1 and R_2 indicate the distance to the suspension point and break-off point to the centre of mass, respectively. Since the wire remains the same length, we can also state the constraint

$$l^2 + (R_1 - R_2)^2 = (l - z')^2 + d^2. \tag{4.41}$$

It can therefore be shown that the equation for the centre of mass elevation is

$$z'^2 - 2lz' + 4R_1 R_2 \sin^2\frac{(\phi - \phi_{sp})}{2} = 0. \tag{4.42}$$

For small rotations, we can neglect z'^2 and make the small angle approximation to simplify the expression for the elevation in z to,

$$z' = \frac{R_1 R_2(\phi - \phi_{sp})}{2l}. \tag{4.43}$$
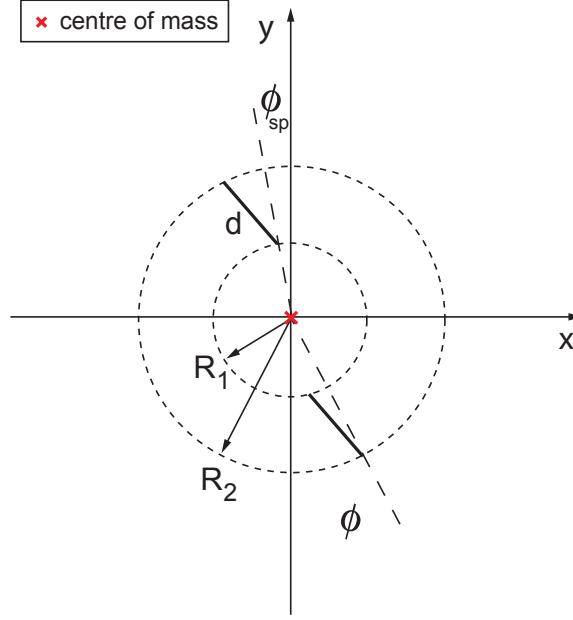
Figure 4.7: *Schematic diagram of a suspended mirror acted upon by yaw motion. The suspension points have been rotated to an angle ϕ_{sp}, whilst the break-off points of the suspension wire on the mirror, have been rotated by an angle ϕ. R_1 and R_2 indicate the distance to the suspension point and break-off point to the centre of mass respectively.*

The kinetic energy of the suspended mirror is the sum of both the translational and rotational motion, defined

$$K = \frac{1}{2}m\dot{x}^2 + \frac{1}{2}I_\psi\dot{\psi}^2 + \frac{1}{2}I_\phi\dot{\phi}^2, \tag{4.44}$$

where I_ψ and I_ϕ are the moments of inertia of the mirror defined as

$$I_\psi = I_\phi = m\left(\frac{R^2}{4} + \frac{L^2}{12}\right), \tag{4.45}$$

where R and L are the radius and length of the cylindrical mirror.

The potential energy of the suspended mirror is defined

$$P = mg(z + z'), \tag{4.46}$$

where m is the mass of the mirror and g denotes the gravitational acceleration. Hence, using Equations 4.39 and 4.43 the complete equation for both planar and yaw motion is

$$P = \frac{mg}{2l}[(x - x_{sp} - b\psi)^2 + bl\psi^2 + R_1 R_2(\phi - \phi_{sp})^2]. \tag{4.47}$$

Finally, from 4.34, the complete Lagrangian for the mirror under planar and yaw motion is therefore

$$\mathcal{L} = \frac{1}{2}\left\{m\dot{x}^2 + I_\psi\dot{\psi}^2 + I_\phi\dot{\phi}^2 - \frac{m}{l}\left[(x - x_{sp} - b\psi)^2 + bl\psi^2 + R_1 R_2(\phi - \phi_{sp})^2\right]\right\}. \tag{4.48}$$

We therefore get the Lagrangian for all three degrees of freedom by substituting 4.48 into 4.35, giving

$$\ddot{x} = \frac{-g}{l}(x - x_{sp} - b\psi), \tag{4.49}$$

$$I_\psi\ddot{\psi} = \frac{-mgb}{l}\left[(l + b)\psi + (x - x_{sp})\right], \tag{4.50}$$

$$I_\phi\ddot{\phi} = \frac{-mgR_1R_2}{l}(\phi - \phi_{sp}). \tag{4.51}$$

These equations are useful as they reveal the natural mode frequencies for each degree of freedom:

$$\omega_x^2 = \frac{g}{l}, \tag{4.52}$$

$$\omega_\psi^2 = \frac{mgb}{I_\psi l}(l + b), \tag{4.53}$$

$$\omega_\phi^2 = \frac{mgR_1R_2}{I_\phi l}. \tag{4.54}$$

To fully describe the equations of motion for each degree of freedom we introduce a loss mechanism to account for the presence of friction, which acts as velocity dependent damping force β, termed *viscous damping*. With this

loss mechanism taken into account the full equations of motion for a freely suspended mirror can be obtained [68]:

$$\ddot{x} + \beta_x \dot{x} + \omega_x^2 x = \omega_x^2 (x_{sp} + b\psi), \tag{4.55}$$

$$\ddot{\psi} + \beta_\psi \dot{\psi} + \omega_\psi^2 \psi = \frac{\omega_\psi^2}{l+b}(x - x_{sp}), \tag{4.56}$$

$$\ddot{\phi} + \beta_\phi \dot{\phi} + \omega_\phi^2 \phi = \omega_\phi^2 \phi_{sp}. \tag{4.57}$$

As it is of interest to model each suspended pendulum in a numerical simulation to analyse their dynamic behaviour, we must transform the equations of motion 4.55-4.57 from the time domain into the frequency domain, in order to efficiently utilise computer memory when running numerical simulations. By describing the equations of motion in state space form, it is possible to obtain multiple outputs from multiple inputs, and enable a numerical model to be built in order to probe the system's dynamic response.

The state space equations utilise four matrices, [$\mathbf{A}$, $\mathbf{B}$, $\mathbf{C}$, $\mathbf{D}$], to define the equations of motion of the pendulum, and are written as

$$\dot{\vec{r}} = \mathbf{A}\vec{r} + \mathbf{B}\vec{u}, \tag{4.58}$$

$$\vec{y} = \mathbf{C}\vec{r} + \mathbf{D}\vec{u}, \tag{4.59}$$

where the input and output vectors are respectively defined $\vec{u}$ and $\vec{y}$, and r is the state vector defined by,

$$\vec{r} = \begin{bmatrix} \vec{q} \\ \dot{\vec{q}} \end{bmatrix}, \tag{4.60}$$

or explicitly in the above derivation as,

$$\vec{r} = \begin{bmatrix} x, & \psi, & \phi, & \dot{x}, & \dot{\psi}, & \dot{\phi} \end{bmatrix}^T. \tag{4.61}$$

Equation 4.60 contains the required identities for a single stage pendulum system in order to maintain simplicity in this section, however, additional

pendulum stages are easily included with the addition of components in the state vector and the [**A**, **B**, **C**, **D**] matrices.

For many cases it is most useful to investigate the suspension dynamics in the frequency domain, and therefore Equations 4.58 and 4.59 are required to be Laplace transformed, resulting in

$$s\vec{R}(s) = \mathbf{A}\vec{R}(s) + \mathbf{B}\vec{U}(s), \tag{4.62}$$

$$\vec{Y}(s) = \mathbf{C}\vec{R}(s) + \mathbf{D}\vec{U}(s), \tag{4.63}$$

respectively, where s denotes the Laplace variable.

In this experiment the author utilised an existing state space model developed extensively by M. Husman, C. Torrie, M. Barton, N. Robertson and K. Strain at Glasgow [69, 70]. The model was amended to incorporate the effects due to radiation pressure forces and associated viscous damping as will be discussed.

4.6 Radiation Pressure Effects in Suspended Cavities

As the stored light in a three mirror coupled cavity interacts with the mirrors, it imparts a radiation pressure force and modifies the suspended mirror dynamics as illustrated by Figure 4.8. In this section, we will highlight the dependence of the mirror position, or more specifically the cavity detuning, to the radiation pressure force acting upon the mirrors. In so doing, we determine the suspended mirrors to be no longer strictly independent and reveal the state required to induce a resonance of the cavity length, commonly referred to as the optical spring effect.
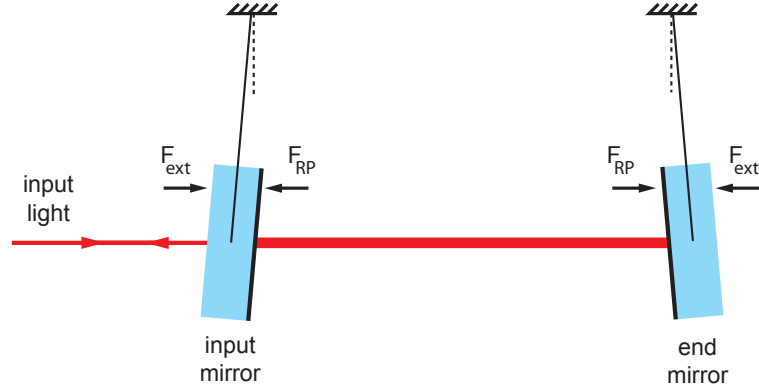
Figure 4.8: *Illustration of Fabry-Pérot cavity on resonance with the cavity mirrors held away from true vertical due to the radiation pressure force F_{RP} but maintained in equilibrium by external forces F_{ext}, consisting of the restoring force of the pendulum and the control force.*

The radiation pressure force on the input cavity mirror, F_{RP_a}, and the end mirror, F_{RP_b}, is directly proportional to the power ($P = |E|^2$) incident upon it, derived from the net fields acting on it, described by

$$F_{RP_a}(t) = \frac{1}{c}\left[|E_i(t)|^2 + |E_{ref}(t)|^2 - |E_{c1}(t)|^2 - |E_{c2'}(t)|^2\right], \qquad (4.64)$$

$$F_{RP_b}(t) = \frac{1}{c}\left[|E_{c1'}(t)|^2 + |E_{c2}(t)|^2 - |E_t(t)|^2\right]. \qquad (4.65)$$

In addition to the downwards force due to gravity, which acts to restore the pendulum to equilibrium, the cavities of an interferometer are held on resonance by applying a feedback force to the mirrors, thus controlling their relative positions. In long baseline gravitational wave detectors and at the Glasgow prototype, this force, known as *global control* [1] is generated by electromagnetic actuators. An array of electromagnetic actuators is mounted on a reaction

---

[1]We distinguish local control, where the sensing and feedback signals are at a single mirror from global control which affects the overall state of the interferometer by controlling the relative positions of mirrors, based on optically derived signals.

mass located at the rear of the main chain suspension. It is also suspended as a pendulum in order to provide a seismically isolated platform from which to apply control. Forces can also be applied at the location of the suspension points in order to control motion below the resonant pendulum resonances. This is used for *local control* and compensation for slow drifts (e.g. Earth tides in km-scale interferometers). Both local and global control stages can be used to damp unwanted excited pendulum modes arising from high Q suspension designs. The details of the force feedback method for this experiment are given below.

The effect of the feedback forces can be represented by a single external force F_{ext}, and included within our previously determined equations of motion in the time domain,

$$\ddot{x}_a + \beta \dot{x}_a + \omega_p^2 x_a = \frac{1}{m_a} \left(F_{RP_a}(t) + F_{ext}(t) \right), \qquad (4.66)$$

$$\ddot{x}_b + \beta \dot{x}_b + \omega_p^2 x_b = \frac{1}{m_b} \left(F_{RP_b}(t) + F_{ext}(t) \right), \qquad (4.67)$$

where β denotes the damping rate, ω_p represents the pendulum frequency, and $m_{(a,b)}$ denotes the mirror mass. This is a complete description of the suspended mirror motions as they interact dynamically with incident light fields.

In high finesse Fabry-Pérot cavities, the internal radiation pressure incident upon the cavity mirrors is much greater than the radiation pressure from the incident light on the input mirror, and thus the magnitude of the radiation pressure force incident upon the cavity mirrors is almost identical but acting in the opposite direction, allowing us to write,

$$F_{RP_a} \simeq -F_{RP_b} \qquad (4.68)$$

As will become apparent, it is useful to decouple each of the mirrors by expressing the relative mirror motions as a change to the cavity length, such

that

$$\xi = x_b - x_a. \qquad (4.69)$$

Using Equations 4.66, 4.67 and 4.68, we can re-write the equation of motion for changes to the cavity length as

$$\ddot{\xi} + \beta\dot{\xi} + \omega_p^2\xi = \frac{1}{m_b}\left(F_{RP_b}(t) + F_{ext}(t)\right) - \frac{1}{m_a}\left(F_{RP_a}(t) + F_{ext}(t)\right), \qquad (4.70)$$

$$\ddot{\xi} + \beta\dot{\xi} + \omega_p^2\xi = \frac{1}{m_r}\left(F_{RP_b}(t) + F_{ext}(t)\right), \qquad (4.71)$$

where ξ denotes the cavity length, and m_r is the reduced mass, defined by

$$m_r = \frac{m_a m_b}{m_a + m_b}. \qquad (4.72)$$

We want to derive the principal concept of optical spring generation within a cavity, and express the optical spring constant in useful parameters for comparing experimental observations to the numerical model. The following analysis begins by considering first the quasi-static solution - that for which mirror motions are slow compared to the response time of the cavity. Later a time-dependent description of the optical spring will be applied to account for additional effects which occur when the frequency of mirror motion approaches the cavity linewidth.

In our experimental setup we planned to investigate optical spring behaviour within a cavity using an end mirror approximately 30 times lighter than the input mirror. In this regime, it is reasonable to consider only the end mirror movable, which helps to simplify the analysis of radiation pressure effects inside the cavity. When the cavity is on resonance the end mirror can be held in a state of equilibrium if the mechanical restoring force, gravity and radiation pressure force are balanced and constant. From Equation 4.65 and the static cavity field derived earlier 4.8 we can remove the subscript b and write the

maximum radiation pressure force on the end mirror as,

$$F_{RP_{max}} = \frac{1}{c}\left[\left(\frac{\tau_a E_i}{1 - \rho_a \rho_b}\right)^2 + \left(\frac{\tau_a \rho_b E_i}{1 - \rho_a \rho_b}\right)^2 - \left(\frac{\tau_a \tau_b E_i}{1 - \rho_a \rho_b}\right)^2\right]. \qquad (4.73)$$

From the field equations 4.23, and 4.24 we can further express the maximum radiation pressure force in terms of internal cavity power, the reflection and transmission efficiencies of the end mirror, and the cavity detuning,

$$F_{RP_{max}} = \frac{P\left(1 + \rho_b^2 - \tau_b^2\right)}{c}\frac{1}{1 + F\sin^2\theta}. \qquad (4.74)$$

In most full scale gravitational wave detectors, and in the Glasgow prototype $\rho_b^2 \approx 1$ and $\tau_b^2 \approx 0$, therefore acknowledging Equation 4.30, we obtain the familiar expression for the maximum radiation pressure force on the end cavity mirror

$$F_{RP_0} = \frac{2P_0}{c}. \qquad (4.75)$$

The author uses the expression 4.75 to develop the analysis of generating optical springs within cavities, however the model used for comparison later utilises the full form described by 4.74, with reflection and transmission efficiencies limited by real mirror loss.

Since the properties of the mirrors are assumed to be constant, we can express the changes in radiation pressure force as a function of maximum cavity power and cavity detuning as,

$$F_{RP} = \frac{2P_0}{c}\frac{1}{1 + F\sin^2\theta}. \qquad (4.76)$$

Hence, for the static case we can write the equations of motion for the end mirror described by 4.70 as

$$m_r\omega_p^2\xi - F_e(t) = \frac{2P_0}{c}\frac{1}{1 + F\sin^2\theta}. \qquad (4.77)$$

Parameter	Value	Description
τ_c^2	0.0495000	recycling mirror transmission
τ_a^2	0.0122820	input mirror transmission
τ_b^2	0.0000024	end mirror transmission
ρ_c^2	0.9504500	recycling mirror reflectivity
ρ_a^2	0.9877180	input mirror reflectivity
ρ_b^2	0.9999396	end mirror reflectivity
M_c	$1.5\,\mathrm{kg}$	recycling mirror mass
M_a	$2.7\,\mathrm{kg}$	input mirror mass
M_b	$0.1\,\mathrm{kg}$	end mirror mass
L_{ext}	$5.16\,\mathrm{m}$	external cavity length
L_{int}	$9.87\,\mathrm{m}$	internal length
γ_{RC}	$29.05\,\mathrm{MHz}$	external cavity linewidth
γ_{AC}	$31.88\,\mathrm{kHz}$	internal cavity linewidth
P_{laser}	$0.15\,\mathrm{W}$	input power
λ	$1064\,\mathrm{nm}$	laser light wavelength

Table 4.1: *System properties for the Glasgow* 10 m *prototype in the optical spring experiment.*

If the mirror is *statically* shifted by an amount dx (or equivalently if the laser frequency is changed by $d\omega$) the radiation pressure force will change,

$$dF_{RP} = \frac{2}{c}\frac{\partial P}{\partial x}dx. \tag{4.78}$$

In other words, it is possible to treat the cavity mirrors as being connected with an optical spring, having a spring constant

$$K_{opt} = -\frac{2}{c}\frac{\partial P}{\partial x} = -\frac{2}{c}\frac{\partial P}{\partial \theta}\frac{\partial \theta}{\partial x}. \tag{4.79}$$

The internal cavity power is a function only of detuning θ, which is small relative to the FSR, thus we can make the small angle approximation ($\sin\theta =$

θ) and write

$$\frac{\partial P}{\partial \theta} = -\frac{2P_0 F\theta}{(1 + F\theta^2)^2}.$$ (4.80)

We can express the detuning parameter as $\theta = \frac{2\pi x}{\lambda}$, resulting in the derivative with respect to x as,

$$\frac{\partial \theta}{\partial x} = \frac{2\pi}{\lambda}.$$ (4.81)

This allows us to present the optical spring constant explicitly as,

$$K_{opt} = \frac{8\pi P_0 F\theta}{c\lambda (1 + F\theta^2)^2}.$$ (4.82)

Furthermore, a *positive* optical spring constant acts to enhance the rigidity of the suspended mirror, thus the pendulum resonance frequency is increased, which can be described using the relationship,

$$f_{opt} = \frac{1}{2\pi}\sqrt{\frac{K_{opt} + K_{mech}}{m_r}},$$ (4.83)

where K_{mech} is the mechanical spring constant of the lowest stage pendulum with length l defined by

$$K_{mech} = \frac{m_b g}{l}.$$ (4.84)

However, in the Glasgow prototype system the mechanical spring constant of the pendulum $K_{mech} \approx 3.3\,\text{N/m}$, which can be shown to be sufficiently smaller than the expected optical spring constants and therefore can be ignored, meaning we can write Equation 4.83 simply as

$$f_{opt} = \frac{1}{2\pi}\sqrt{\frac{K_{opt}}{m_r}}.$$ (4.85)

It is worth noting that we use the reduced mass in this equation because the two cavity mirrors are connected by the same optical spring with equivalent spring constant.

Figure 4.9 shows the relationship between the cavity power and optical spring constant as a function of cavity detuning for a single Fabry-Pérot cavity using the parameters for the cavity mirrors a and b detailed in Table 4.1. For

Figure 4.9: *Calculated intracavity power (blue curve) and the optical spring constant (green curve) as a function of detuning for a single Fabry-Pérot cavity defined by the parameters in Table 4.1.*

convenience, the detuning is herein expressed in dimensionless units relative the cavity linewidth δ_γ. As the cavity detuning is increased (positive) the optical spring strength increases, while for negative detuning, the optical spring constant is anti-restoring, meaning that the incident radiation pressure force assists any change to mirror position. Therefore we have shown that negative detuning results in an unstable system. This case is not of interest in our experiment and is henceforth ignored.

Based on the numerical model for a static cavity it can be shown that the maximum power build up of the internal cavity alone would be approximately 48 W, and for a cavity detuning $\delta_\gamma \approx 0.29$ the maximum optical spring strength would be around $K = 396$ N/m, with an optical spring frequency $f_{opt} \sim 10.2$ Hz.

However, without optimum power coupling and maximum detuning the optical spring frequency reduces rapidly and since the pendulum modes of the triple suspensions occur up to several tens of Hz, it would be challenging to observe optomechanical behaviour in the Glasgow prototype with just one optical cavity.

We can also investigate the expected level of spring strength and frequencies for a three mirror coupled cavity system using the parameters from Table 4.1. It is found that the expected internal cavity power build up is around 1991 W, providing a resonant radiation pressure force on the cavity end mirror $F_{RP} \approx 13.3\,\mu\text{N}$. It follows that the maximum optical spring strength obtained for a coupled cavity arrangement detuned to $\delta_\gamma \approx 0.29$ is $K = 9.4 \times 10^5\,\text{N/m}$. Correspondingly, the maximum optical spring frequency would be approximately $f_{opt} = 496\,\text{Hz}$. Hence the coupled cavity system would bring the optical spring well into a range in which measurements are convenient.

Figure 4.9 illustrates the effect of cavity detuning on both the intracavity power and the optical spring constant. The intracavity power has dropped to half the maximum when the detuning is equal to the resonance linewidth. The optical spring constant changes sign depending on which side of the resonance the detuning occurs. It can be seen that exactly on resonance, the spring constant is zero, while maximum optical spring constant is found when $\delta_\gamma \approx \pm 0.29$. Note the maximum optical spring constant varies depending on the parameters of the cavity. The intracavity power at this level of detuning corresponds to $P_{\delta_\gamma=0.29} \approx 0.75P_0$, where P_0 represents the intracavity power for zero detuning.

However, rearranging 4.19 the coupled cavity linewidth can be calculated as,

$$\gamma_\omega = \frac{\Delta\omega}{\mathcal{F}} = \frac{2c}{L\sqrt{F}}. \tag{4.86}$$

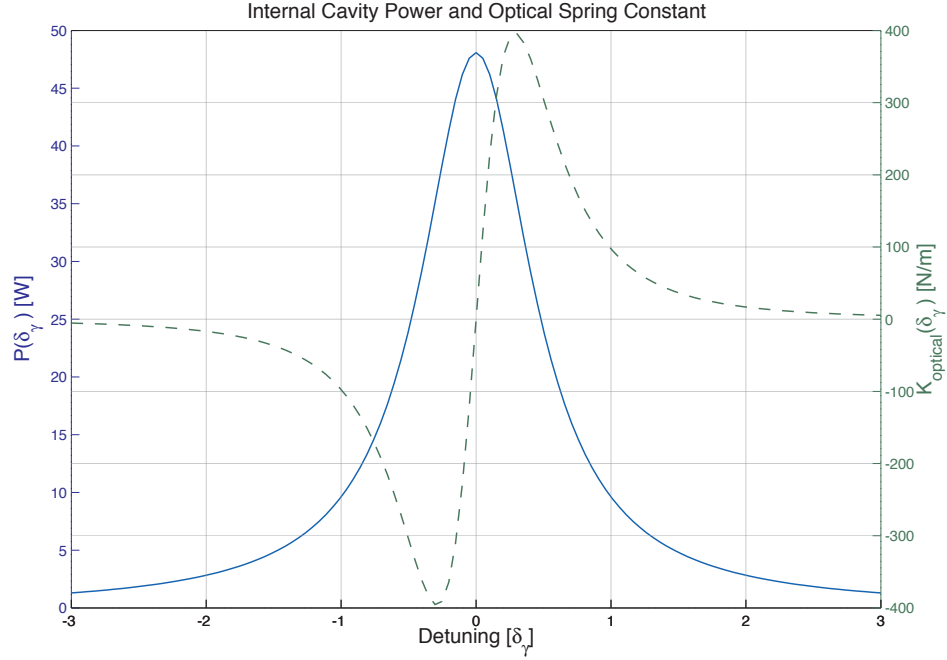Using the system parameters detailed in Table 4.1, we find the expected
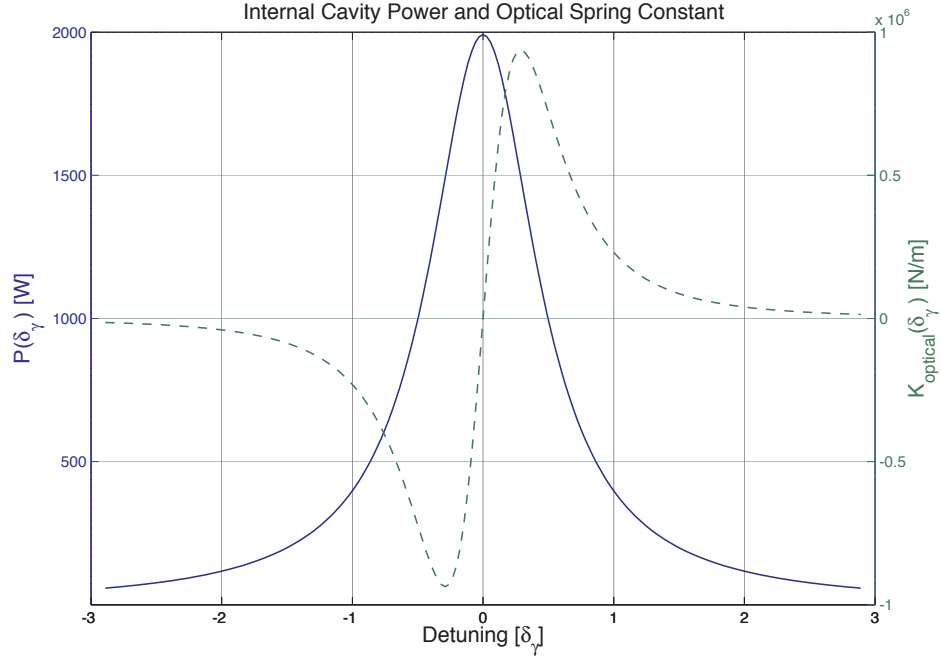
Figure 4.10: *Calculated intracavity power (blue curve) and the optical spring constant (green curve) as a function of detuning for a coupled Fabry-Pérot cavity defined by the parameters in Table 4.1.*

linewidth of the coupled cavity to be approximately $2\pi(526)$Hz. The coupled internal cavity linewidth is therefore sufficiently narrower than the single Fabry-Pérot cavity alone, any measurement process to obtain the optical response would induce mirror motion at comparable frequencies. Therefore our earlier assumption of quasi-static detuning is not sufficient for our experiment and we must include the response time of the cavity within our analysis.

The frequency dependent optical rigidity has been studied [65, 71], and upon simplification can be shown to be

$$K_{opt}(\omega) = K_{opt}\frac{1 + \delta_\gamma^2}{(1 + i\omega\gamma)^2 + \delta_\gamma^2}. \qquad (4.87)$$

Hence, the complete description of the frequency dependent optical rigidity is complex with the real components attributed to rigidity and imaginary parts
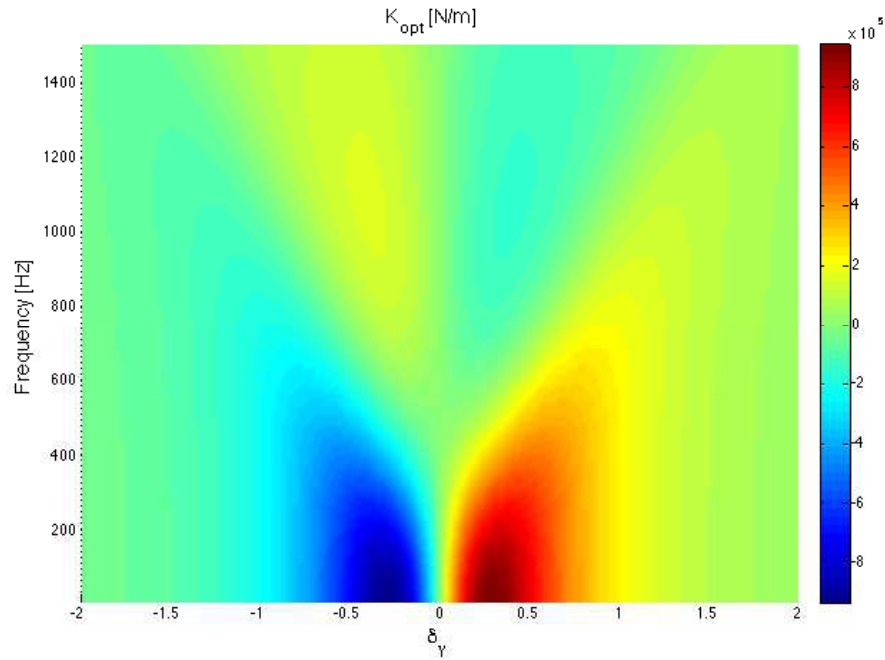
Figure 4.11: *Optical spring strength as a function of cavity detuning and frequency of observation, based on the complete frequency dependent spring strength equation 4.87. The details are discussed in the text.*

describing a velocity dependent damping force. The full form of the optical spring constant is valid for all mirror frequencies, and we see that for sufficiently slow mirror motion ($\omega \to 0$) the imaginary term disappears resulting in the expression obtained earlier for static detuning.

Figure 4.11 shows the expected change to the strength of the optical spring constant with respect to detuning and frequency of observation, based on the numerical model. At frequencies greater than the cavity linewidth the spring constant is predicted to change sign. In other words there is a fundamental limit to the observation of an optical spring that is directly related to the response time of the cavity.

At this point it is useful to look at the response of the mirror when coupled to

a strong optical field under optomechanical conditions, in other words the displacement per unit force. This analysis reveals the corresponding enhancement and degradation to the system for gravitational wave sensing. The complex susceptibility can be written as [72],

$$\frac{x}{F} = \frac{1}{-\omega^2 + (2\pi f_{opt})^2 + im_r\omega\beta}, \tag{4.88}$$

where we define the damping rate of the system as the sum of the mechanical damping rate, β_m and the optical damping rate β_{opt},

$$\beta = \beta_m + \beta_{opt}. \tag{4.89}$$

The imaginary part of 4.87 provides the optical damping coefficient, described by

$$\beta_{opt} = \frac{\Im(K_{opt})}{m_r\omega} = \frac{-2K_{opt}}{m_r\gamma(1 + \delta_\gamma^2 - \omega_\gamma^2)^2 + 4\omega_\gamma^2}, \tag{4.90}$$

where the sign change indicates the damping force opposes the direction of the optical restoring force and therefore, depending on whether detuning is positive or negative the optical damping will counteract or enhance the mechanical damping force. The optical damping rate is shown in Figure 4.12, for different levels of detuning and frequency of observation. The former case can result in a phenomenon known as parametric instability when the optical damping exceeds the mechanical damping, whereas negative detuning increases the damping of the suspended mirror and can provide a useful mechanism towards removing unwanted thermal energy from coupled mirror systems, known as *cold damping* [73, 74]. In the Glasgow system there are two effects which act to stabilise the spring. Firstly, as described below, the cavity length is controlled by a servosystem. This has a pole (or pair of poles) associated with its unity gain frequency. As that frequency is far above the optical spring resonance, instability of the spring plays no significant role in the stability of the closed-loop system. Additionally there is mechanical damping associated with
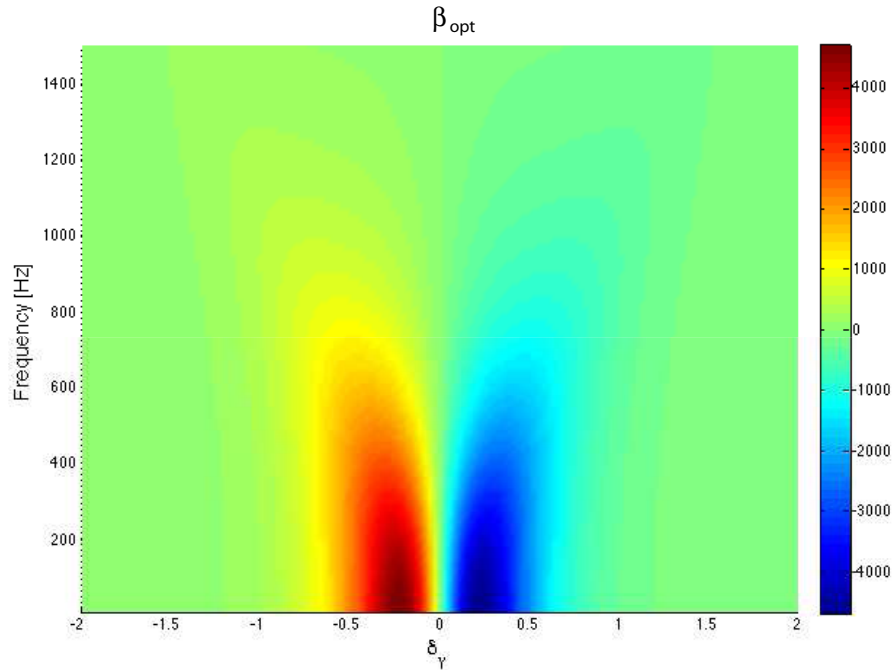
Figure 4.12: *The optical damping rate is shown for a range of cavity detuning levels and the frequency of observation.*

the mirror. The two dominant components of this damping are the loss in the wires and their clamps which hold the mirror, and loss due to the attached actuation magnets inducing currents in the associated coils.

Figure 4.13 shows the corresponding magnitude and phase response, derived from 4.88 and 4.89 for various levels of cavity detuning, indicating an amplification around the optical spring resonance features with a corresponding phase change of 180 degrees. From the predicted optical response of the system, we observe a 180 degree phase decrease as a stable optical spring regime, whereas it can also be shown that in some cases a 180 degree phase increase reveals an unstable optical spring state. Also shown in Figure 4.13 is the suppressed system response at frequencies below the optomechanical resonance, suggesting an increased rigidity acting against mirror motion.
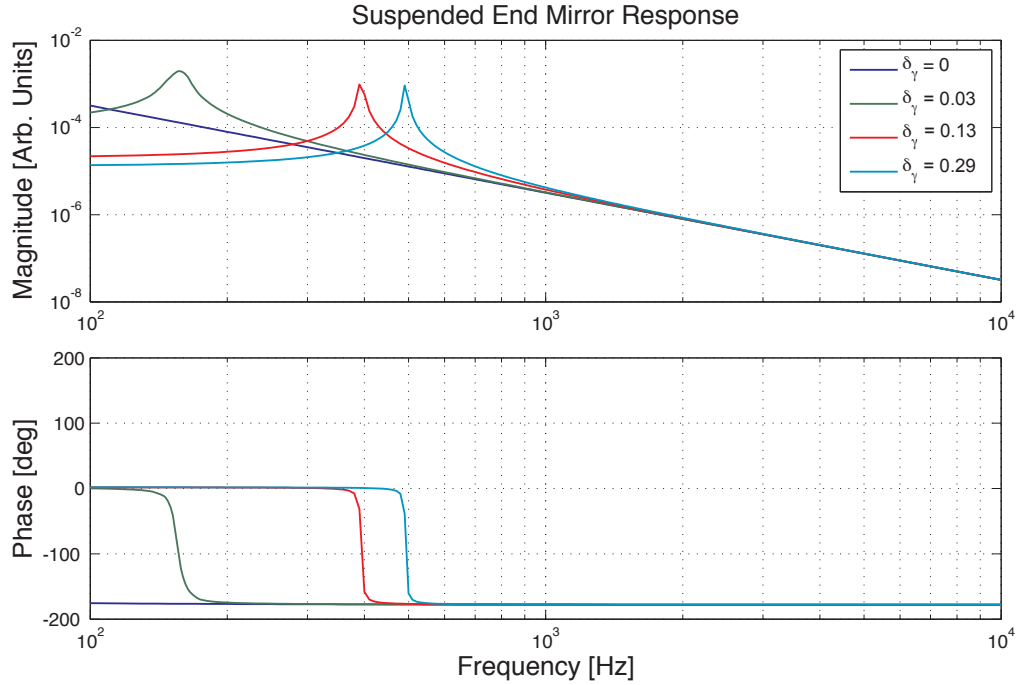
Figure 4.13: *Suspended cavity end mirror response based on Equation 4.88 using system properties defined in Table 4.1 for different levels of cavity detuning. The response is amplified around the location of an optical spring, while being suppressed at lower frequencies. A characteristic 180 degree phase change is observed at the locations of the optomechanical resonance.*

4.7 Characterising Optomechanical Coupling in a Triple-Suspended Recycled Cavity

Our aim was to develop a system capable of observing opto-mechanical behaviour within a prototype scale interferometer whose optical components are suspended as multi-stage pendulums. The desired setup would allow future experiments into various aspects of radiation pressure dominated cavities such as the control requirements employed through analogue and digital feedback, as well as characterising the dynamic behaviour associated to optical rigidity

in coupled cavity systems. Furthermore, a working system would enable the Glasgow prototype to become a test bed for proof-of-principle experiments into alternative optical topologies utilising optical rigidity, such as optical bar and optical lever interferometers.

4.7.1   Experimental Design and Implementation

In this section I will detail the analysis and choice of design for a replacement mirror of low mass, and its suspension, to increase overall sensitivity to radiation pressure effects.

Cavity End Mirror

To observe opto-mechanical coupling between the mirrors of an optical cavity, the radiation pressure force exerted by the internal cavity field must be comparable to, or greater than, the mechanical restoring force of the pendulums [65]. Since the radiation pressure force is inherently weak, this requires high finesse cavities to maximise the amount of stored light. The mirror test masses in the Glasgow prototype are approximately 2.7 kg, however reducing the mass of one of the cavity mirrors it will become more sensitive to radiation pressure effects. Previous experiments to observe and characterise the behaviour of optical springs in prototype-scale optical cavities have been limited to test masses of up to 1 g [75, 76, 65]. At Glasgow we aimed to generate optical spring behaviour using significantly larger mirror masses of 100 g for the end mirror and the existing 2.7 kg input mirror.

The mirror to be used in the experiment was 1 inch in diameter with a 15 m concave radius of curvature. It was manufactured from a fused silica substrate,

with a highly reflective coating designed to be 99.9950% reflective at normal incidence (a very high quality ion-beam sputtering processed was used, and the substrate had been polished to sub-Angstrom roughness to reduce scatter). The mirror is then mounted inside an aluminium holder for suspending. It was decided to maintain the standard cylindrical shape for the aluminium holder but instead to miniaturise the overall design in order to bring the total mass of the lowest stage to approximately $100\,\mathrm{g}$ including the mirror, wire clamps, screws, and magnets. The control over the position of the mass would be achieved using an almost identical reaction mass housing coils for electromagnetic actuation. Figure 4.14 shows the final design drawing created in the computer-aided-design engineering package SolidWorks [77], from which the remainder of the design drawings have been generated.

Isolation and Control

The existing input mirror is mounted as the lower stage of a triple pendulum, in order to effectively isolate seismic noise above the fundamental pendulum mode. To ensure that any changes to the dynamic behaviour of the lightweight mirror can be confidently attributed to increased sensitivity of radiation pressure effects, a triple-stage suspension design was also chosen for this design. Hence the end mirror will be seismically isolated above the resonant pendulum frequency having a transfer function of the magnitude response falling off as a $1/f^6$ slope.

As with the existing input mass suspension, in order to control the position of the test mass electromagnetic actuators were located at the test mass stage, as illustrated in Figure 4.14, for global alignment. The local control actuation, located at the upper stage in the existing Glasgow prototype suspensions, is achieved using an arrangement of six shadow sensors (positioned to control
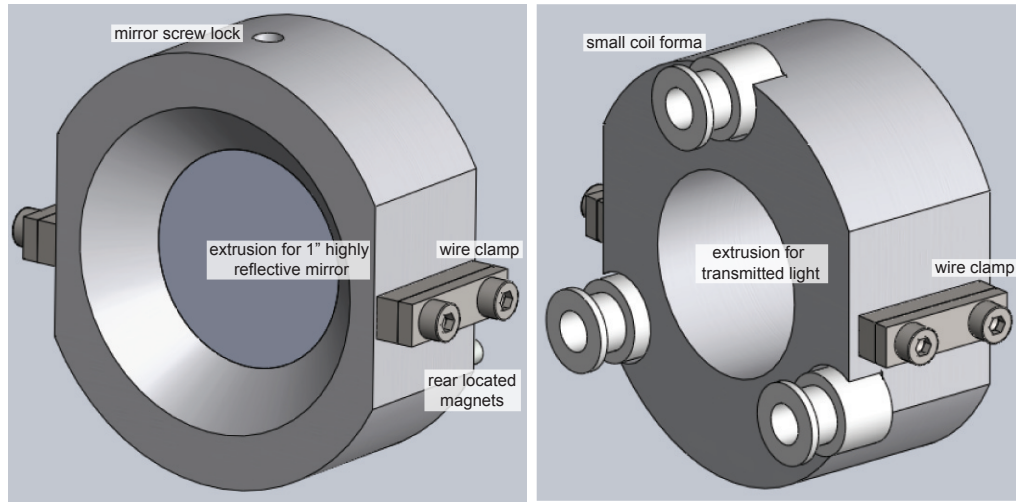
Figure 4.14: *Computer-aided-design drawing of the assembled lower test mass (left) and the lower reaction test mass (right). The test mass incorporates a standard design to mount a mirror at its centre of mass, whilst clamping points of suspension wires are positioned 1 mm above the centre-of-mass plane. A symmetric array of magnets at 3 locations are positioned at the rear of the mass to be actuated upon by the co-located coils on the reaction test mass suspended within proximity for control. The reaction mass is of similar design to meet mass restrictions, and incorporates an extruded centre to allow transmitted light to be monitored.*

all degrees of freedom) and electromagnetic actuators, as indicated by Figure 4.15. This technique monitors the shadow of an illuminated flag upon a photodiode to obtain information about the suspension behaviour and provide active damping and additional dynamic range to global control. For the replacement end mirror suspension however, a passive eddy-current damping technique was chosen because of overall size constraints, limitations in the construction process, and simplicity to employ.

The choice for a 100 g test mass as part of a triple suspension imposes re-
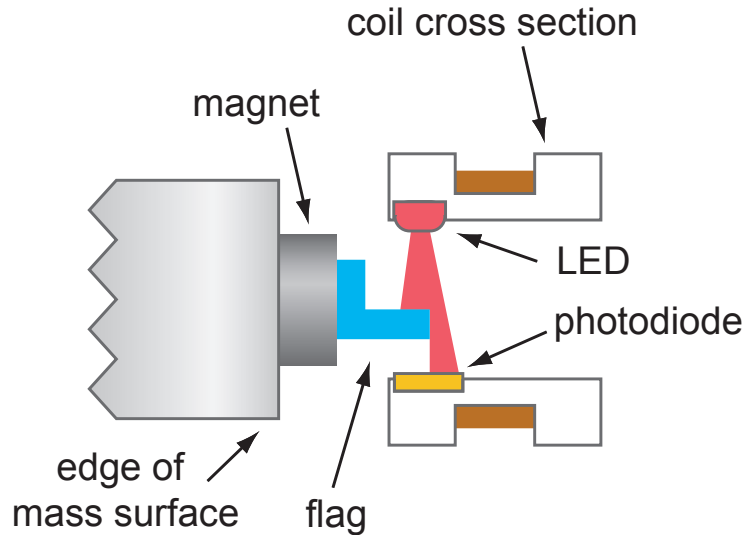
Figure 4.15: *Illustration of the shadow sensor arrangement used to sense and damp motion of the suspensions as well as control alignment of the each suspension chain.*

straints on the design of the other stages. Since all the rigid-body pendulum modes need to be damped by the eddy-current dampers at the top stage, it is necessary for the pendulum motion to efficiently couple into at least one degree of freedom of that stage. The starting point to achieve this is to connect the lower stages using 4 wires at each level. The efficiency of coupling from the lower to the upper stage is then maximised by ensuring the masses and moments of inertia of each pendulum stage about the corresponding axes are within a factor of approximately 2, with the stiffness of each stage increasing from upper to lower [70]. It was possible to integrate these restrictions within the triple-suspension design by ensuring the intermediate and upper masses were restricted to $100\,\text{g}$ and designed with approximately the same moment of inertia about the equivalent axis. The suspension wire break off point for each stage was chosen to be $1\,\text{mm}$ above and below the xy-plane of the corre-

sponding centre-of-mass, providing stability. The constraints for stiffness are met by having the wires for the upper stage angled inwards along the y-axis, and similarly for the intermediate stage, by way of a clamping unit between the front and rear faces.

The eddy-current damping unit design was chosen by locating a suitable strength magnet within proximity to a copper surround (calculated in the numerical simulation package Mathematica [78]), and at a suitable distance from the centre of mass (to increase the lever arm), such that the state-space simulation indicated a sufficient damping force to damp excited modes. The requirements for eddy-current damping and mass constraints of the upper stage led to the overall design as pictured in Figure 4.16. Note that the relatively strong damping applied at the top mass is decoupled from the final pendulum stage supporting the mirror at all frequencies above the highest pendulum resonance (a few Hz).

The chosen intermediate stage design is similar to the upper stage, to restrict the overall mass to 100 g, whilst also incorporating clamping point displacements along the y-axis for upper and lower wires to ensure angled wires increase the suspension stiffness from upper to lower stages as shown in Figure 4.17. Moreover, the break-off points are similarly located 1 mm above and below the centre-of-mass plane along the xy-axis.

The end mirror suspension was chosen to have equal 30 cm wire lengths, between each stage, with an adjustable upper-most clamping position to maintain the same overall suspension length as the input mirror suspension and ensure the incident cavity beam to be central on the end mirror.

Both the choice of wire for suspending the mirror and the location of suspension points for each stage affect some of the pendulum modes. Explicitly, for
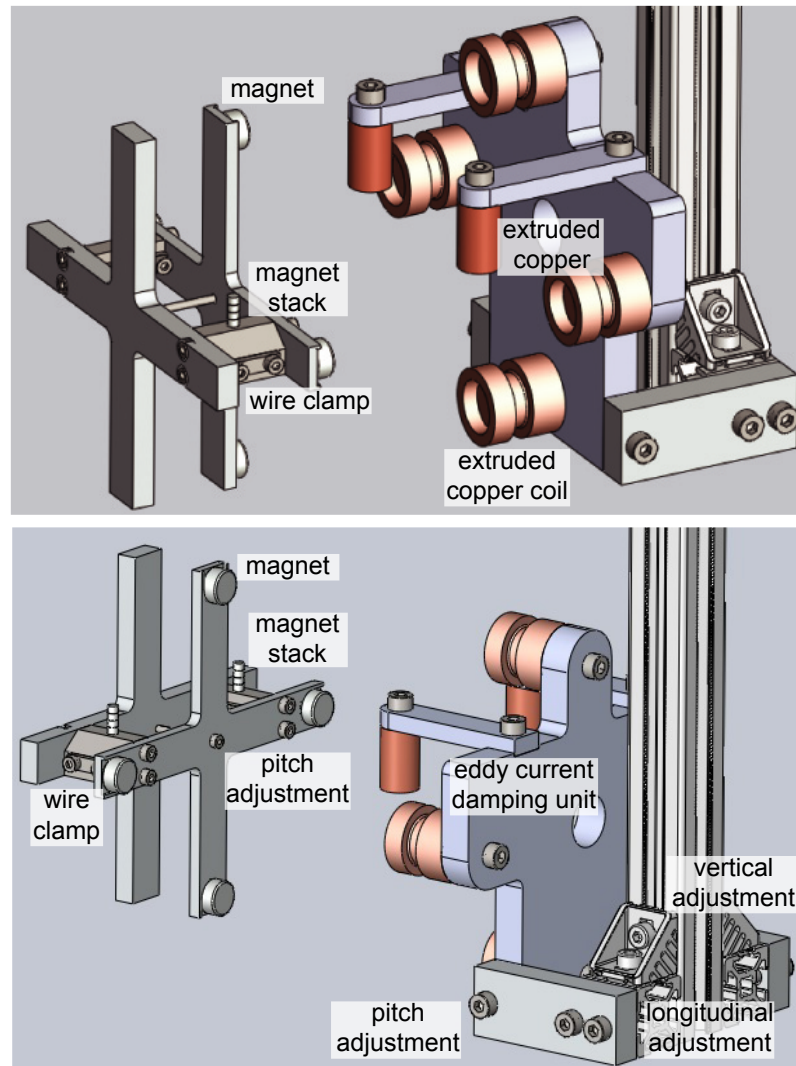
Figure 4.16: *Different views for the computer-aided-design assembly of the upper mass and eddy-current damping unit. The upper mass (left hand side of each view) incorporates angled wire clamping, suitable locations for magnets on the front and upper faces, fine tuning pitch adjustment screw, and overall mass/inertia restrictions met. The eddy-current damping unit (right hand side of each view) has copper surrounds for each magnet. The front face also incorporates copper wound coils for alignment. Adjustment to vertical, longitudinal and pitch position is possible as indicated.*
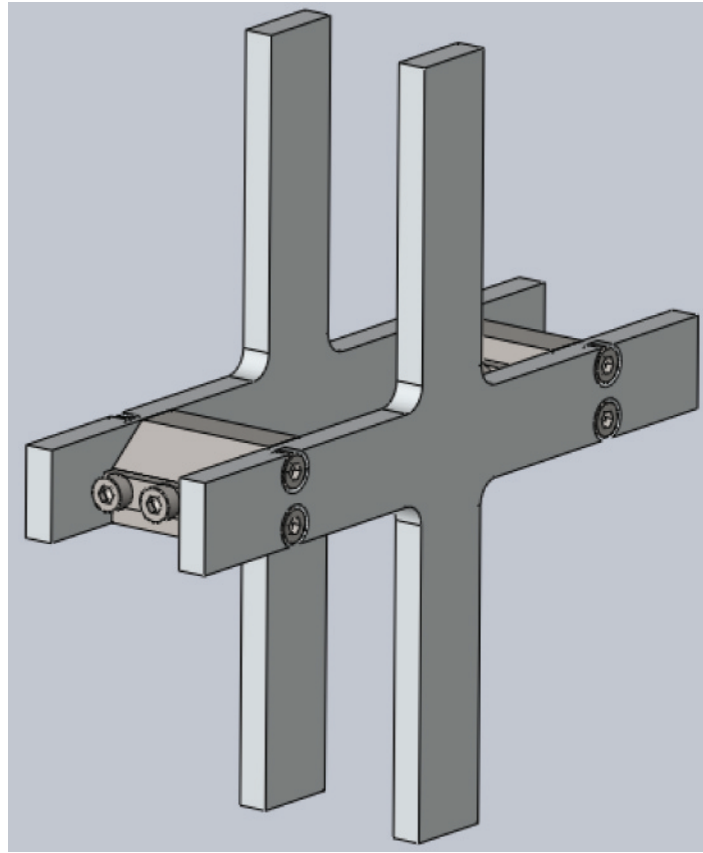
Figure 4.17: *Computer-aided-design assembly of the intermediate mass.*

a given material, the pitch modes of each stage are reduced in frequency when the wire thickness is reduced. The choice of wire was selected through an iterative process using the state space numerical model to restrict the pendulum modes within the desired bandwidth. It was found that $55\,\mu$m radius stainless steel wire was a suitable candidate to balance the requirement for sub-100 Hz pendulum modes whilst remaining large enough for handling during construction.

The upper-most wire clamping points on the existing triple-stage suspensions in the prototype are fixed to a series of cantilever-mounted blade springs to enhance the vertical isolation. The cantilever blades are constructed from

maraging steel (processed to pin its dislocations giving it a very high elastic limit). The springs are pre-curved such that under load they are approximately flat, such that small displacements of their tips as they flex are almost purely vertical. However, in working with triple suspensions suspended from these springs, it had been noticed that the clamping points are seldom aligned on the same plane. Although offsets at the upper clamping point are not a concerning issue for large masses, these perturbations would potentially limit the range for alignment of a light-weight suspension. Therefore, it was decided to clamp the upper-most suspension points to a fixed support, which itself would be isolated by way of a passive seismic isolation stack. As noted above damping of all suspension modes is facilitated by having two wires suspend the upper mass, followed by four wires to suspend the intermediate mass, and a final four wires suspend the test mass as shown in Figure 4.18. The separations of the wires along the x-axis are optimised using the state space model to ensure the (coupled) pitch and longitudinal modes are within the desired bandwidth. This has become a standard approach to suspension design at Glasgow and brings the additional benefit of allowing control of the lower stages from the top-most mass, similar to the operation of a marionette.

The pendulum modes for the overall suspension design were obtained from the state space model are detailed in Table 4.2. To characterise the suspension modes two initial tests were performed: (*i*) attempt to lock the cavity on resonance with global control and without the eddy-current damping unit (no local control) in order to monitor the cavity response transfer function and (*ii*) repeat the measurement but with the damping unit in place. The first test was unsuccessful as the cavity could not be held locked for a duration substantial to monitor low frequencies, indicative of undamped pendulum modes. However, the second test, whilst the local control damping is applied, showed that the cavity could be locked indefinitely throughout measurements and a low, mid
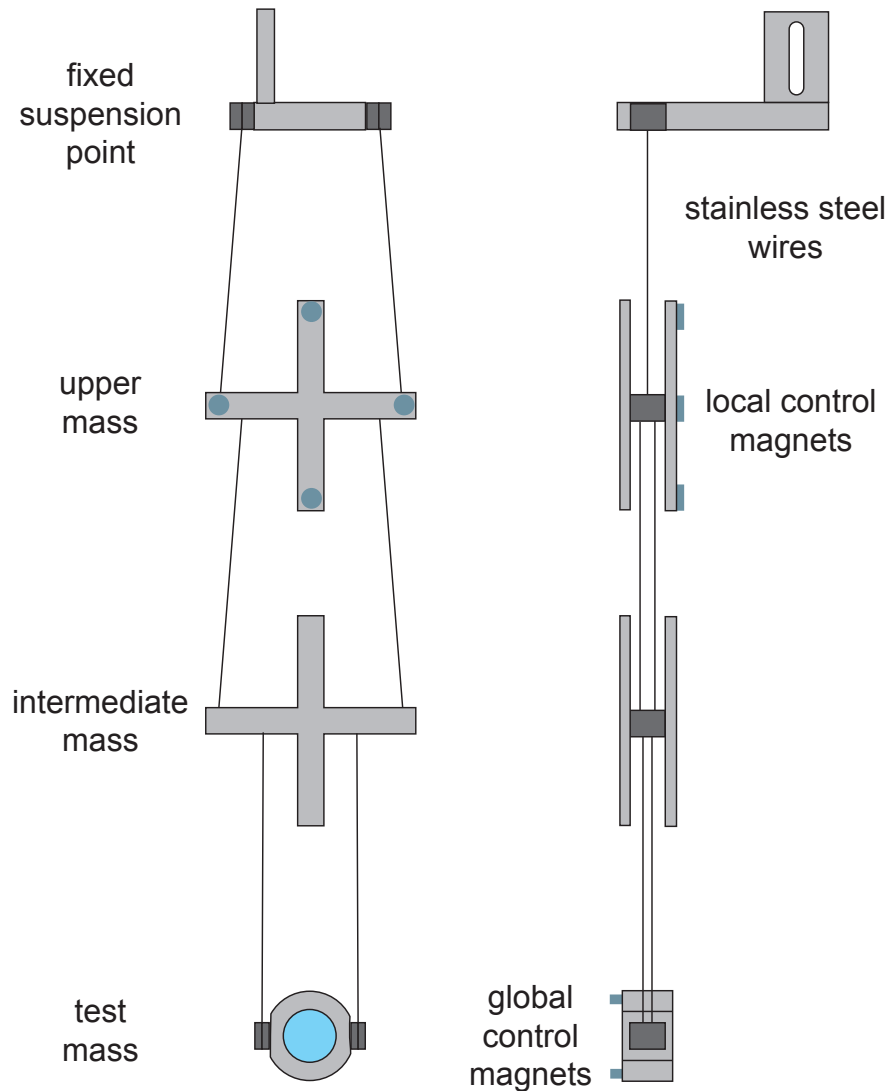
Figure 4.18: *Schematic of the entire main suspension chain as front view (left) and side view (right). The eddy-current damping unit has been omitted for clarity. Two angled wires suspend the upper mass, four angled wires suspend the intermediate mass, and four vertical wires suspend the test mass.*

range and high frequency cavity response signal could be obtained. When the cavity field is maintained in a TEM_{00} resonance, the detected output signal from a photodiode is monitored by a signal analyser (model Stanford Research Systems SR785), to reveal the longitudinal/pitch and rotational mode

Normal Mode	Predicted Mode Frequencies [Hz]	Quality Factor
Longitudinal/Pitch	0.60, 1.52, 1.95,	8.20, 2.59, 2.45,
	2.59, 17.89, 30.88	1.07, 12.28, 17.96
Rotational	1.10, 2.12, 2.36	2.37, 0.97, 17.40
Translational/Roll	0.60, 1.52, 1.95,	8.38, 2.59, 2.48,
	44.89, 102.87, 151.91	47.59, 87.20, 1018.28
Vertical	26.69, 81.04, 133.40	82.34, 93.09, 528.91

Table 4.2: *Mode properties for the light-weight end mirror triple-suspension design.*

frequencies of the cavity mirrors. As indicated by Figure 4.19, all resonant features are in good agreement with the model and outside the bandwidth of interest for observing optical spring behaviour.

Suspension Assembly and Implementation

Having chosen the overall suspension design, it is essential to devise an assembly process that will meet the desired tolerance. One key advantage of the entire suspension is low mass, which enables an alternative assembly procedure, much simpler than that used for the larger mass suspensions. Since the total suspension length is less than 1 m, it is possible to construct the entire suspension with the eddy-current damping unit within a single aluminium jig on a table-top. By assembling the suspension this way, the position accuracy of each element is comparable to the manufacturing machine tolerance (±0.5 mm) as the individual separations are well defined. The suspension wires can also be clamped to high precision in this way. Once the entire suspension is assembled, it can be manoeuvred into position inside the vacuum system for the upper-most clamping stage to be fixed to the supporting structure.
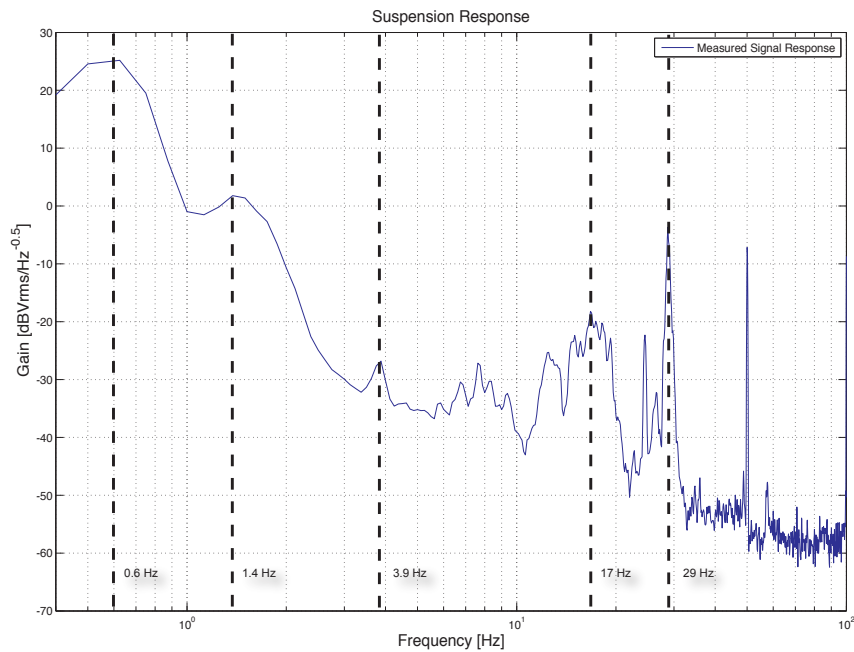
Figure 4.19: *Low frequency response indicating features that can be attributed to the expected longitudinal/pitch modes of the suspension. The feature located at 50 Hz is most likely the result of a ground loop.*

The suspension is subsequently unlocked from the jig, which is then removed, leaving only the suspension hanging. This process was remarkably successful as well as being efficient in construction time, since both the main suspension and reaction suspension hung as intended in the first instance, as shown in Figure 4.20.

However, this unique design is not without its own problems. The clamping piece for the upper and lower stages must pin two wires, therefore each wire position has to be correctly aligned at the same time. In addition, the upper and intermediate wires are clamped to a piece of stainless steel connecting the front and back cross pieces, which are difficult to adjust once each stage is assembled. This restricts future amendments, such as replacing broken wires,
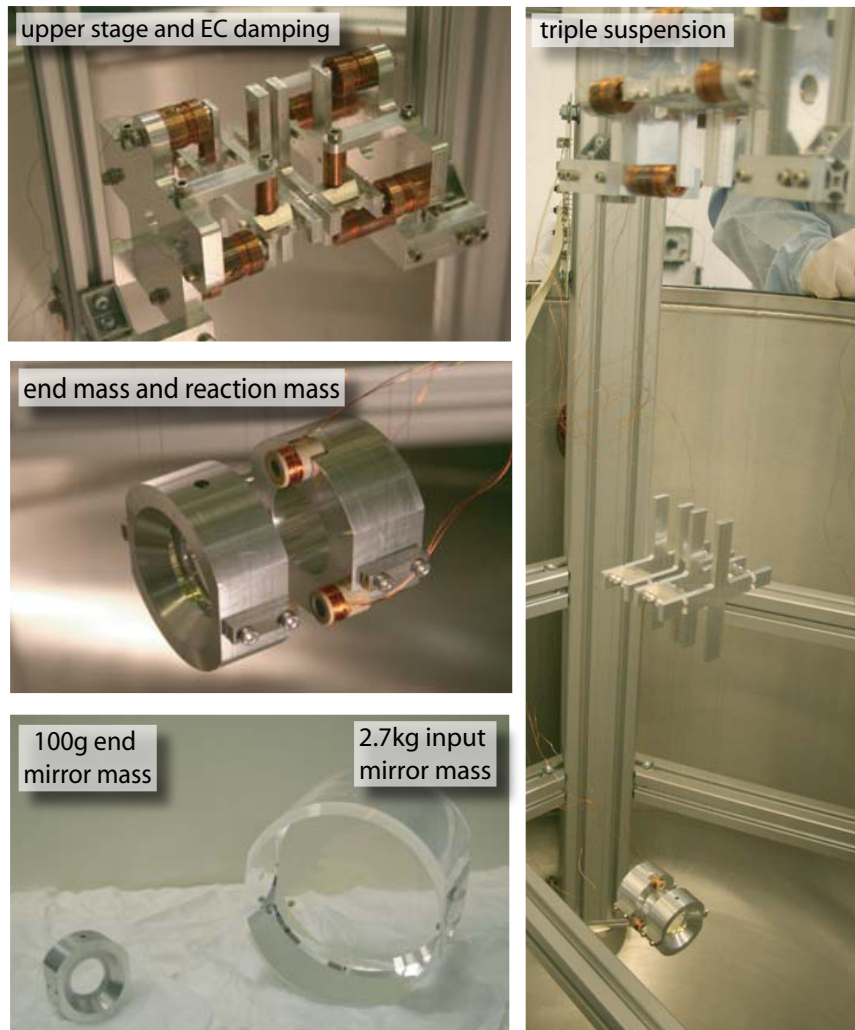
Figure 4.20: *Photographs of the full triple stage suspension (right) located at the end of the arm cavity, the upper stage and surrounding eddy-current (EC) damping unit (top left), the* $100\,\mathrm{g}$ *test mass and reaction mass (middle left), and comparison of light-weight end mass and input mirror mass (bottom left).*

without placing the suspension inside the assembly jig and removing from the system entirely.

4.7.2 Experimental Method

In this section the length sensing and control scheme used to maintain the coupled cavities at the operating point is first highlighted. Following on from the control scheme, the method employed for detuning of the internal cavity in order to induce optical spring behaviour is discussed.

Coupled Cavity Control Scheme

As with any large scale laser interferometric gravitational wave detector utilising coupled optical cavities, it is necessary to control the relative positions of the mirrors in the Glasgow prototype to maintain the desired resonant conditions in each cavity. The typical procedure for length sensing and control is based on the Pound-Drever-Hall technique whereby various radio frequency (RF) modulation sidebands are imposed onto the carrier light, with a particular modulation index. By splitting the carrier into various frequency components that resonate in different cavities, and monitoring the reflected light on photodetectors through demodulation, it is possible to sense the beat between the frequency components after traversing through the system. The beat between each frequency component reveals any phase shift that it acquired resulting from changes in the cavity length.

In this experiment it was important to obtain a flexible control scheme and to completely decouple the length sensing signals from both optical cavities. Ensuring the sensing signals from each cavity to be completely independent required both amplitude and phase modulation sidebands to be imposed onto the carrier light. Figure 4.21 illustrates the system for modulation and demodulation used for the experiment.

The arm cavity length-sensing signal can be derived by applying phase modulation (PM) onto an electro-optic modulator (EOM) to generate phase sidebands. The light returning from the cavity is then passed through a Faraday isolator to pick the light off the beam path, where it is then split on a 50 : 50 beamsplitter; one path to an 18 MHz tuned photodiode and the other path to a 4.525 MHz tuned photodiode (discussed shortly). The light detected on the 18 MHz photodiode is then mixed with a local oscillator (LO) at 18 MHz, thus demodulating the signal to be filtered through feedback servo electronics to control the high frequency motion via the piezo-electric-transducer (PZT) on the laser and control low frequency motion via the temperature input to the laser crystal. The PM sidebands were chosen arbitrarily to be non-resonant in both cavities.

Meanwhile, the recycling cavity (RC) length-sensing signal is derived by applying PM sidebands at 10 MHz, which is non-resonant in both cavities, and amplitude modulation (AM) sidebands at 14.525 MHz, which is exactly half the free spectral range of the recycling cavity and resonant only in the recycling cavity. The control of the recycling cavity is performed by feeding back to electromagnetic actuators positioned on the rear of the recycling mirror mass.

A similar length sensing and control scheme for the three mirror coupled cavity system had been previously demonstrated on the Glasgow 10 m prototype [79]. In this experiment, it was demonstrated that even without an auto-alignment system installed it was possible to optimise the local oscillator phase and modulation frequency to achieve purity of orthogonal sensing from both cavities. Hence, the arm cavity can be subjected to detuning without affecting the sensing and control signals used for the recycling cavity, a key feature in this experiment.
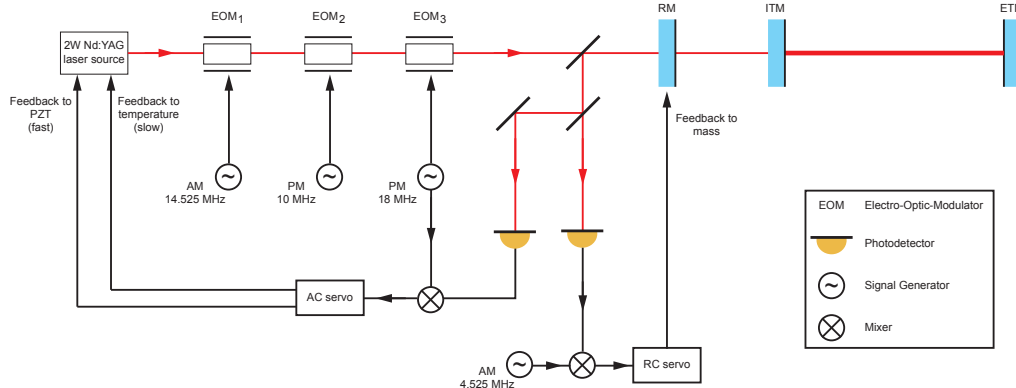
Figure 4.21: *Illustration of the amplitude modulation (AM) and phase modulation (PM) scheme used for length sensing and control of the recycling cavity (RC) and arm cavity (AC) whilst maintaining decoupling.*

Characterising the Coupled Cavity

Before characterising the dynamic effects associated to opto-mechanical coupling of cavity mirrors in detuned cavities, it is important to measure the response of the resonant cavity to external forces, to reveal any unwanted features. Using a signal analyser to inject motion via actuators on the cavity mirror for a fixed laser frequency, or equally the laser frequency input to a static cavity, the response of the coupled arm cavity signal can be monitored. Figure 4.22 indicates that the response closely matches the expected $1/f^2$ slope for a suspended mass up to approximately 200 Hz where the signal becomes limited by the noise floor of analyser at the expected frequency range for optical spring generation. Additionally, a 27 kHz resonant feature is evident, indicating there was an instability in the control servo path due to the unity gain point, which at the time of this measurement could be easily excited if an unsuitable level of gain was used to lock the system. This instability feature was later fixed by replacing one of the resistors in the feedback path to change the location of the unity gain point.
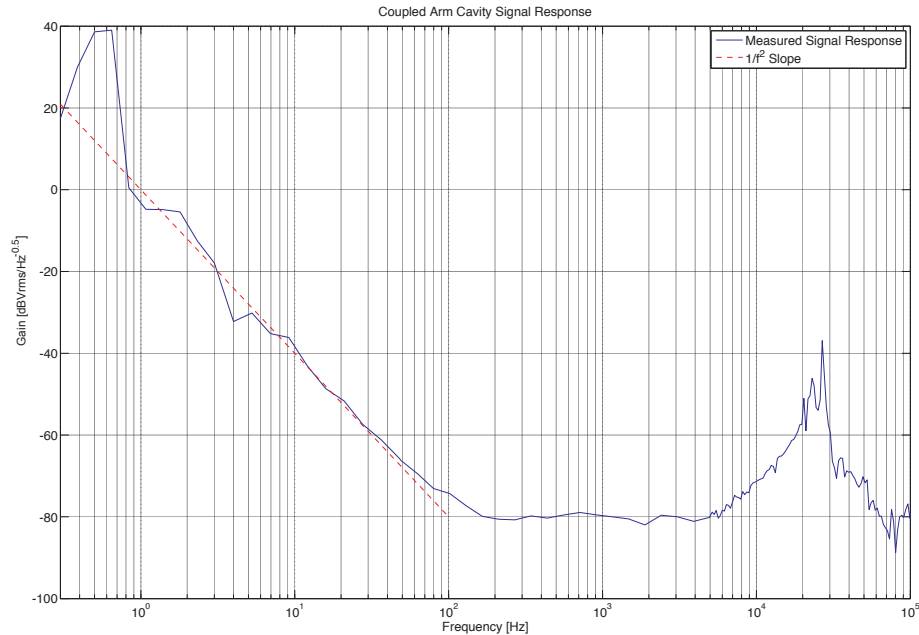
Figure 4.22: *Full-span frequency response of the coupled arm cavity indicating a $1/f^2$ shape at low frequencies. A distinct feature at approximately $27\,\mathrm{kHz}$ corresponds to the unity gain point, which at the time of this measurement could be made unstable without careful choice of the overall gain, however this problem was later fixed by increasing the unity gain frequency with additional filtering.*

Furthermore, on close inspection of the measured DC signal from the photo-diode located behind the cavity end mirror to monitor the transmitted light, it was noted that the light level appeared to reduce when the overall gain of the feedback path to the PZT was increased. This behaviour suggested that there was an oscillation in the error signal being used to hold the system at the operating point. However, this was not evident from frequency response measurements, therefore suggesting that it was located outside the observable bandwidth of the cavity and the spectrum analyser (the SR785 is limited to around $100\,\mathrm{kHz}$). Therefore a high frequency spectrum analyser was used to monitor the demodulated error signal, revealing a resonant feature at $273\,\mathrm{kHz}$,
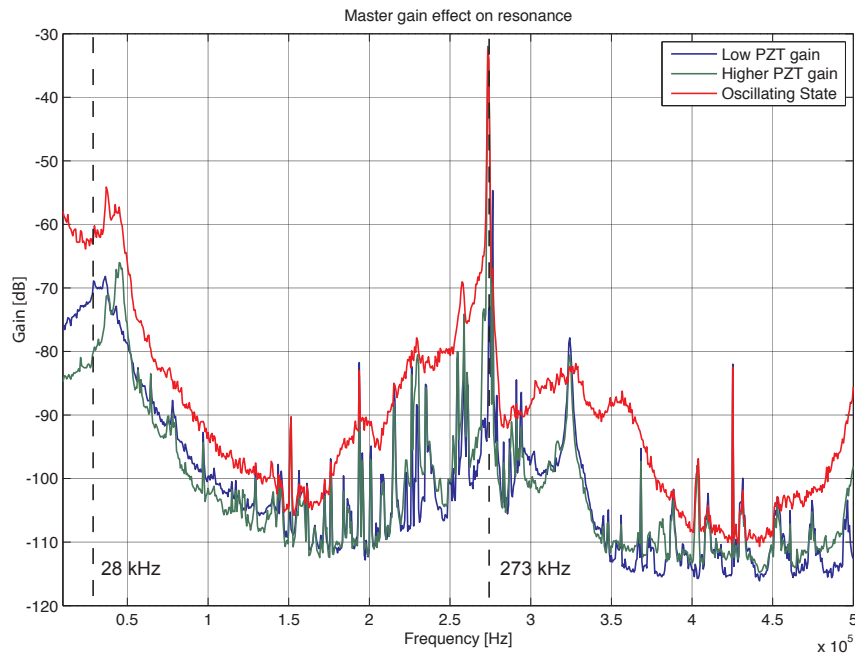
Figure 4.23: *High frequency FFT frequency response of the internal cavity error signal used in the PZT feedback path. A distinct resonant feature at $273\,\mathrm{kHz}$ is observable when the overall gain in the feedback path is increased. A notch filter was subsequently implemented to remove the oscillation and enable high gain to be used for stability during cavity lock.*

which became more pronounced when the PZT gain was increased, as indicated by Figure 4.23. A notch filter was later added to the feedback path in order to remove the high frequency oscillation, thus enabling higher overall gain to be used for increased operational stability and resulting in maximum stored power in the internal cavity.

Form these characterisation steps it was shown that there was no pendulum mode frequencies or unstable feedback resonances perturbing the optical response within the frequency band of interest, thus permitting further investigations into opto-mechanical behaviour induced via cavity detuning.

A suitable gain was chosen for the PZT feedback path to hold the three mirror coupled cavity system locked and stable for extensive periods in order to obtain measurements of optical response. However, it is also necessary to validate the system parameters, such as the mirror properties, the coupled cavity finesse, and the resonant linewidth.

A complete characterisation of a *single* Fabry-Pérot cavity is relatively trivial to perform, for which there are several techniques. The following details one method used in this experiment. Firstly, an accurate measurement of the transmission efficiencies of each mirror can be obtained using a calibrated power meter and a known laser source. In addition, since an accurate estimate on length of the cavity is known, the FSR is easily obtained using Equation 4.18. Thus by obtaining the resonance linewidth the cavity finesse can be calculated using Equation 4.19.

One technique to determine the resonance linewidth accurately, requires sweeping either the laser frequency or the cavity length through one FSR, whilst monitoring the transmitted or reflected DC signal from a photodetector on an oscilloscope. It is also possible to inject an additional signal, with a known frequency from a signal generator, into the feedback path whilst scanning the length of the cavity and monitoring the reflected/transmitted light on a photodetector. This technique acts to impose frequency sidebands with a well defined frequency separation, and thus the DC signal observed on an oscilloscope can be subsequently calibrated accurately. In this experiment the latter approach was performed by injecting a 200 kHz frequency signal on the PZT feedback path and monitoring the reflected DC signal on an oscilloscope (Tektronix TDS2000C Series) as shown by Figure 4.24.

The finesse measurement and associated error margin places a lower limit on
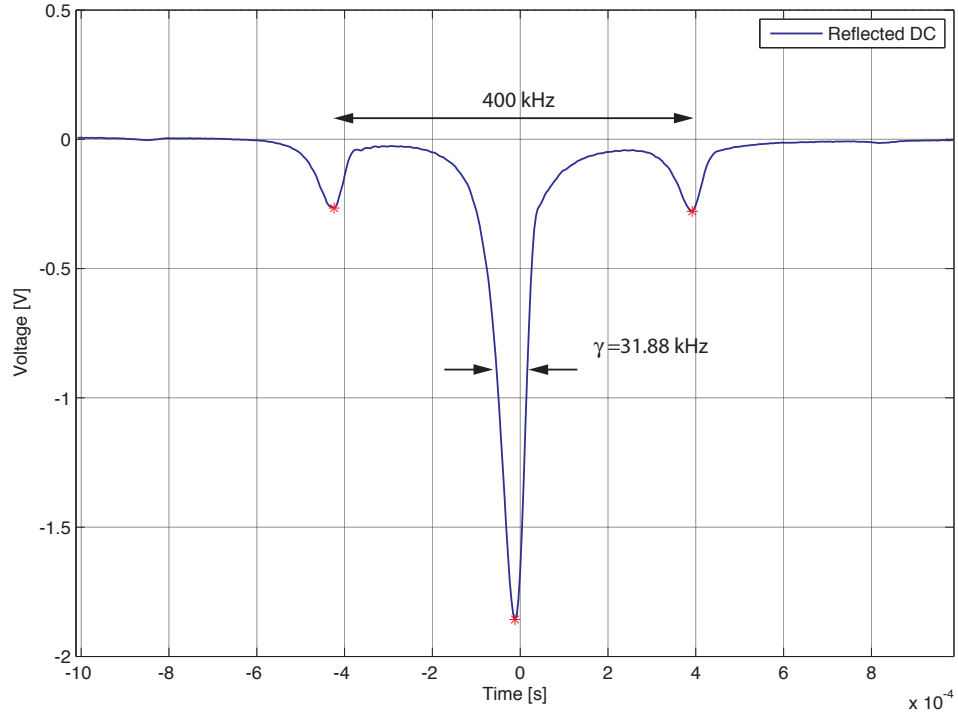
Figure 4.24: *Data from one of the oscilloscope measurements used to calculate the internal cavity finesse. The injected light has additional frequency sidebands applied using the PZT feedback path and a signal generator, whilst the light that is reflected from the cavity is monitored on a photodetector and the DC component monitored on the oscilloscope.*

the sum of the total loss for the cavity mirrors as described by

$$\mathcal{F} = \frac{2\pi}{\tau_a^2 + \mathcal{L}_a + \tau_b^2 + \mathcal{L}_b} \tag{4.91}$$

where $\mathcal{L}_a$ and $\mathcal{L}_b$ are the power losses of the input mirror and end mirror respectively. Thus it is possible to make reasonable assumptions about the loss of each mirror and compare a numerical model with the experimental results.

However, in systems where cavities are coupled together, such as the three mirror coupled cavity used in this experiment, the precise parameters of the

mirrors when the system is held at the operating point are not easily obtained. The aforementioned technique can not be used for the direct measurement of the cavity linewidth and finesse due to the limitations of our photodetectors and the overwhelming size of the coupled cavity length sensing signal. Instead, it was necessary to characterise each cavity alone in order to determine the total losses, and calculate the properties of the three mirror coupled cavity system numerically.

A series of linewdith and finesse measurements were obtained when the internal and external cavity mirrors were aligned separately. The measured finesse of the internal cavity was 478.1 ± 25.8, while the external cavity finesse was found to be 86.5 ± 11.0. The loss from each cavity was determined using Equation 4.91. In order to simplify the task of setting the appropriate loss on each mirror in the model, no loss was placed on the input mirror, while the recycling mirror and end mirror were allocated a power loss that was restricted by the margin of error for the total loss measured in each cavity.

Measuring Optical Springs

From the system analysis, discussed in Section 4.6, a maximum frequency range for an optical spring feature is expected to be approximately $500\,\mathrm{Hz}$, which means it is located within the bandwidth of the control servo system. In order to characterise an optical spring feature in the Glasgow prototype, it is therefore necessary to measure the PDH error signal in response to injected excitations of the mirror position or, equivalently, laser frequency, as the control loop forces one to follow the other.

In the design of this experiment a low noise pre-amplifier is implemented inside the control servo loop. The pre-amplifier of choice (Stanford Research Systems
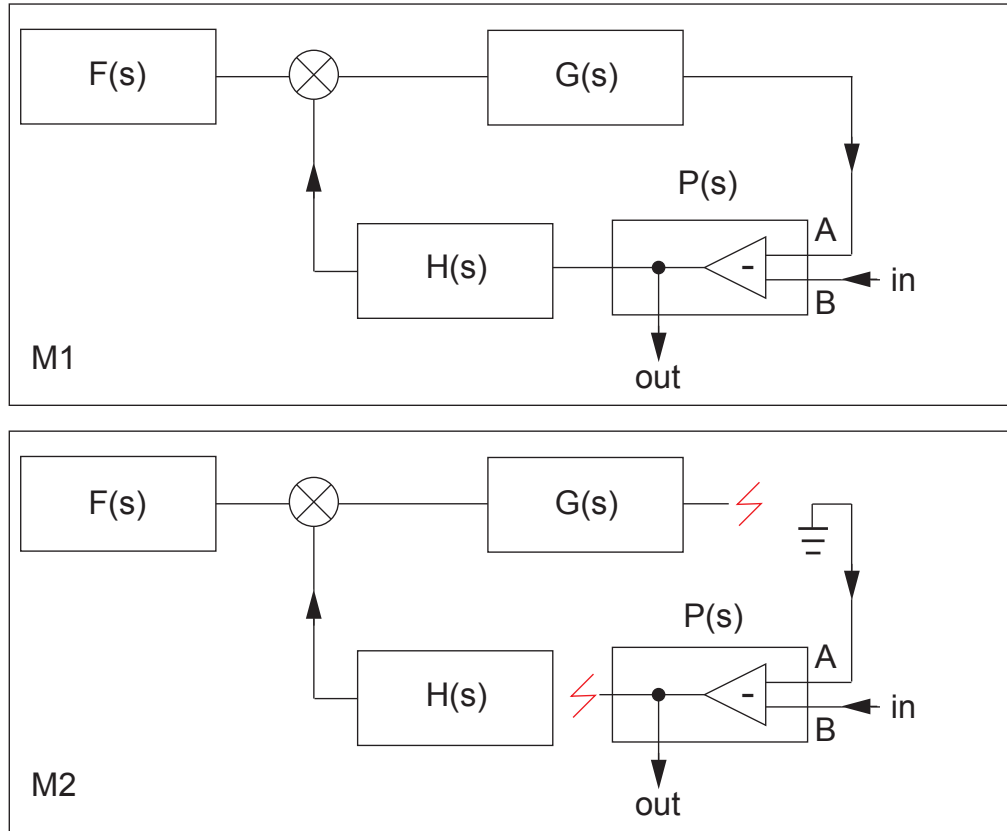
Figure 4.25: *Feedback loop block diagram. An M1 measurement (top) is obtained with the loop closed, and an M2 measurement (bottom) contains only the component used to inject and monitor signals (in this case a dual channel pre-amplifier).*

SR560) has two input channels (A and B) and two outputs of the same signal and is useful in characterising the optical response. It is possible to describe each of the components in the system as part of a block diagram in the complex frequency domain, denoted s, as indicated by Figure 4.25, where $F(s)$ indicates a force applied to the optical path, $G(s)$ represents the optical response, $P(s)$ represents the shape of the pre-amplifier and $H(s)$ represents the feedback response. As we are interested in the optical response of the system when the cavity mirrors are opto-mechanically coupled, several transfer functions are of

interest:

- A *closed-loop* transfer function, which describes the net result from each feedback component in the loop, when the system is operating (closed). This should therefore be unity across all frequencies within the range of the servo loop.

- An *open-loop* transfer function, containing the sum of all the elements inside the loop: the optical cavity response, the servo electronics and the feedback actuator response.

- The feedback frequency response $H(s)$, which contains the entire effect of the feedback servo and the actuation response.

Using the pre-amplifier, the open and closed-loop transfer functions are obtained from two measurements, $M1$ and $M2$, described in Figure 4.25. Mathematically, we can describe $M1$ by,

$$M1 = \frac{P(s)}{1 + G(s)H(s)},$$
(4.92)

and $M2$ is simply the effect of the pre-amp used to inject and monitor signals,

$$M2 = P(s).$$
(4.93)

Thus, we can write the open-loop transfer function, GH, as

$$G(s)H(s) = 1 - \frac{M2}{M1}.$$
(4.94)

The closed-loop transfer function $\frac{G(s)H(s)}{1+G(s)H(s)}$, is obtained by,

$$\frac{G(s)H(s)}{1 + G(s)H(s)} = \frac{M1}{M2} - 1.$$
(4.95)

In a working feedback system, the closed-loop transfer function should remain unity over the frequency band of the servo, which was validated in our experiment by performing this analysis, shown in Figure 4.26.
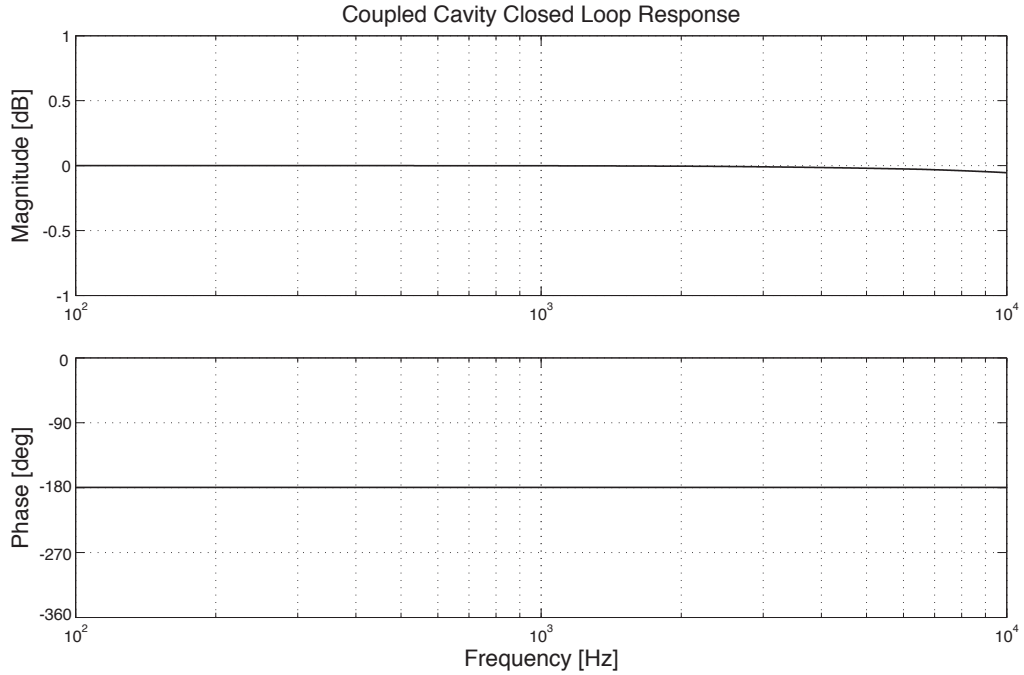
Figure 4.26: *Closed-loop frequency response for the coupled arm cavity showing unity over the entire frequency band. A* 360 *degree correction has been applied to the measured phase data to account for phase wrapping.*

By obtaining the open-loop function, it is possible to remove the measured response of the servo and feedback actuator, $H(s)$ to obtain only the optical response of the coupled cavity system.

In this experiment the arm cavity was held resonant by feeding back to the laser frequency. By applying feedback signals onto the laser PZT in response to changes of cavity length, it is possible to avoid disturbing the beam position on the cavity optics which could potentially lead to *additional* fluctuations of the cavity power, disrupting the measurements. The PZT response stated by the manufacturer is 1.4 MHz/V and constant across the frequencies of interest, therefore the actuator response can be ignored. It was possible to inject signals into the input of the feedback servo electronics and monitor the output on
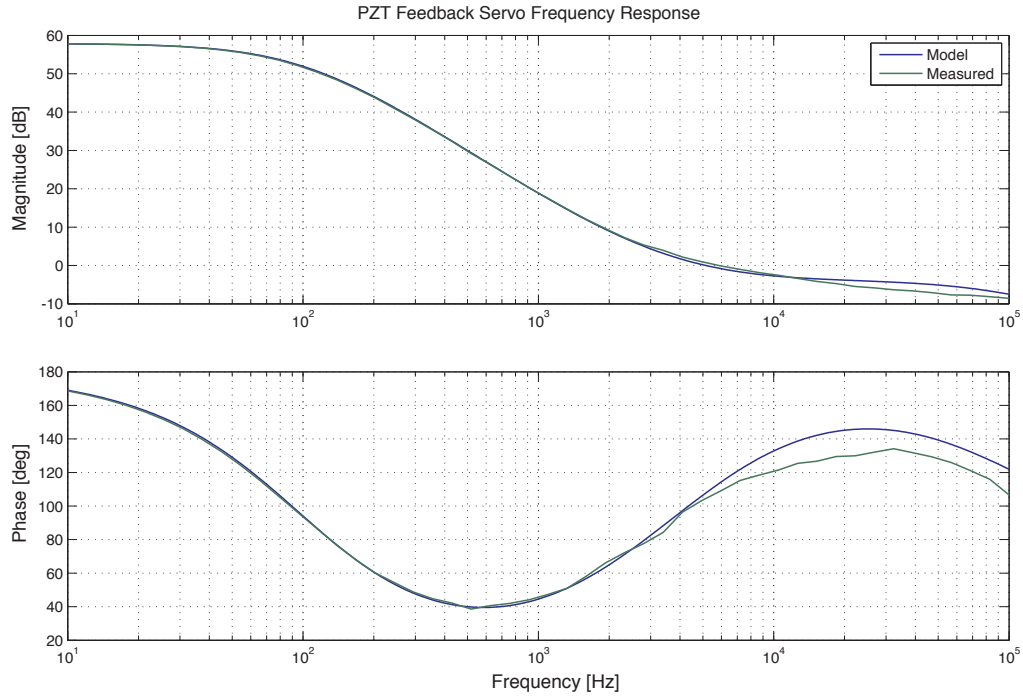
Figure 4.27: *Measured (blue) and modelled (green) frequency response for the feedback servo to the PZT show close comparison. The discrepancy around* 27 kHz *is likely due to the unity gain feature.*

the signal analyser over a frequency band of interest, known as a swept-sine measurement. The expected signal response closely matches a numerical model built in LISO [80] to simulate the effect of the servo, illustrated by Figure 4.27.

The signal analyser, used to measure the response of the various components in the loop, also has the ability to apply a DC offset to the injected swept-sine signals. Therefore, once the loop is closed and the system is locked to the centre of resonance, the arm cavity can be detuned by injecting a DC offset from the signal analyser to shift the laser frequency. After applying a chosen offset the signal analyser is then used to measure the frequency response of the entire loop.

4.7.3 Experimental Results

The optical response of the coupled cavity was measured for different levels of detuning, indicated by Figures 4.28 and 4.29. Several important features of the system were observed when injecting different levels of offset to detune the coupled arm cavity:

- The transmitted power that was being monitored on an oscilloscope, which is directly proportional to the internal cavity power (as shown by Equation 4.12), was observed to reduce for increasing levels of both positive and negative detuning. Such behaviour is expected, since the cavity is being moved away from exact resonance, and will therefore store less light.

- Only positive levels of cavity detuning induced a 180 degree phase flip in the measured optical frequency response at locations of optical spring features. This is also expected as only the positive side of the resonance should induce an optical restoring force, whereas the negative side of the resonance should result in an unstable optical anti-spring. In other words, lengthening the cavity, *blueshifting* the laser frequency, induces an optical spring, while *redshifting* the laser frequency results in an anti-spring.

- When the laser frequency is blueshifted, to induce optical rigidity, measurements of the optical response at frequencies below the optical spring resonance became increasingly more difficult to perform. As a result, and without increasing the level of the swept-sine signal, lower frequency measurements required increasing the number of averages the analyser used to observe the signal above the background noise. This issue is well explained if optical rigidity is suppressing the response of the mirror.

- The optical spring links, in a non-linear (parametric) sense, the static offset applied to set the detuning and the instantaneous frequency injected to perform the transfer function measurement. Ideally the latter would be kept very small (*i.e.* no more than a few percent of the offset) but unfortunately in our experiment that was not generally possible as the transfer function measurement had to compete against background noise. Part of this noise, e.g. random laser frequency fluctuations, was Gaussian and amenable to reduction by increasing the averaging time (within reasonable limits set by the duration of the system remaining operational), but other components, e.g. residual acoustic noise coupling in at various places, including resonances of the suspensions, cannot be averaged out. The results presented here take the current method to its practical limit, and an improved method is identified below, as a subject for future investigation.

In order to characterise the optical spring effect at frequencies greater than $100\,\mathrm{Hz}$ and approaching the linewidth of the coupled internal cavity, it was found necessary to inject large amplitude driving signals to make transfer function measurements as well as using many averages. The effect of the large amplitude driving signals acts to modulate the strength of the optical spring, thus changing the frequency location and resulting in a *smearing* of its absolute position. In Figure 4.28 one of the reflected error signal response measurements taken with a detuning $\delta_\gamma = 0.08$ clearly indicates a smeared optical spring effect and indicates approximately two 180 degree phase changes, revealing the apparent change in the detuning over the period of the measurement.

Furthermore, based on the two numerical models derived in Section 4.6 for static and dynamic detuning, we would expect the strength and frequency of the optical spring to be considerably reduced due to the mirror motion, when
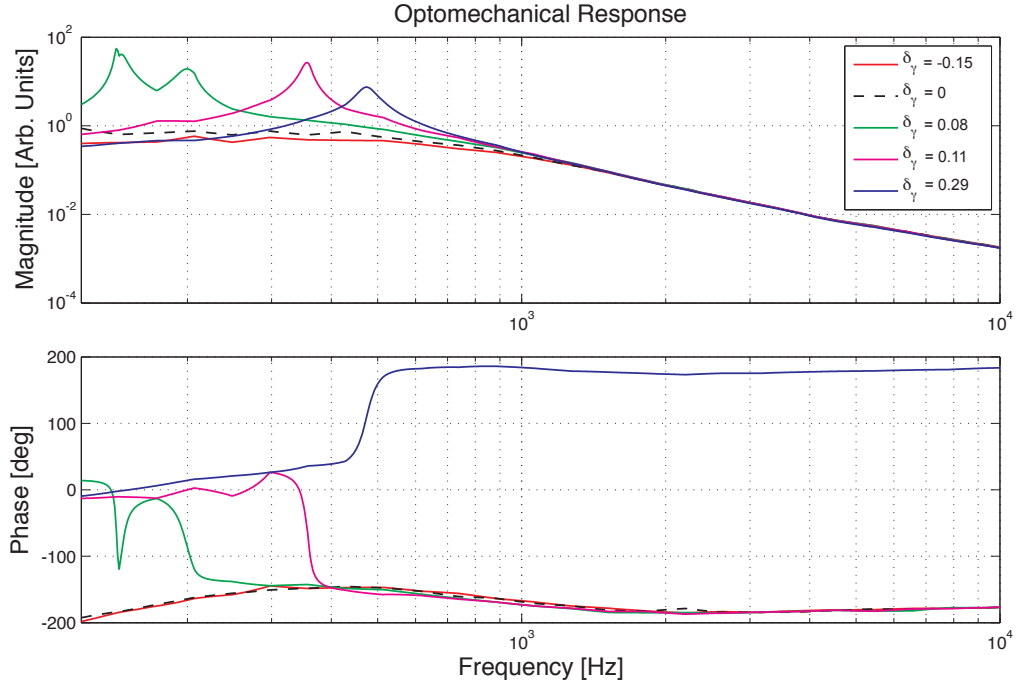
Figure 4.28: *Full-span frequency response of the coupled arm cavity for different levels of detuning. The optical response for $\delta_\gamma = 0$ is indicated by a black dashed line. For positive detunings a distinctive peak is observed above, corresponding to the optical spring resonance, with larger spring frequencies proportional to larger detuning. The phase plot below also indicates a 180 degree phase flip at the optical spring locations as expected. When the cavity detuning is negative, the magnitude of the optical response is reduced. The shape of the green trace is presumed to originate from a change in cavity detuning over the period of measurement. A 360 degree correction has been applied to the measured phase data to account for phase wrapping.*

compared to the static case. However, the results suggest that when using large averaging the effects from modulation of the detuning can be mitigated, allowing for the measurement of the maximum optical spring effect predicted from the static detuning regime.
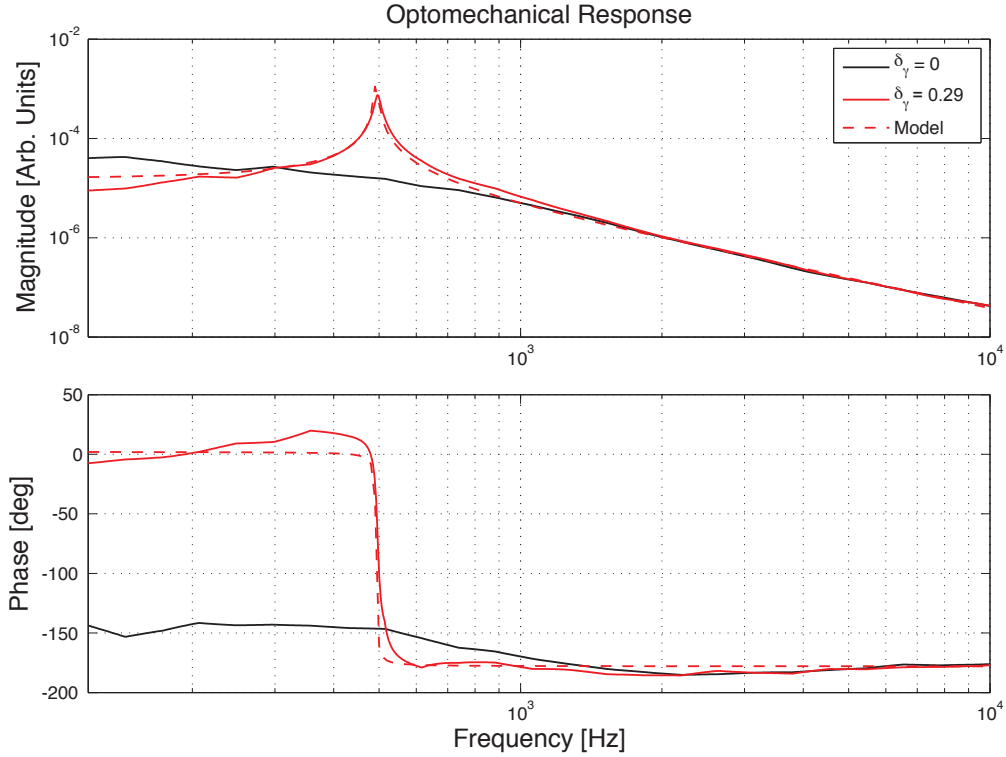
Figure 4.29: *Full-span frequency response of the coupled arm cavity for no detuning (black) and at maximum detuning (red) before the cavity would fall out of lock. A clear resonance feature at approximately 500 Hz is observed with the phase plot below indicating a distinct 180 degree phase flip at the optical spring frequency. The measured optical spring feature and frequency agree well with the modelled response for equivalent detuning (red dashed).*

Figure 4.29 presents the largest observed optical spring frequency, f_{os}, located at around 496 Hz. As the reduced mass of the coupled two mirror system is known, $m_r = 96.4$ g, we can determine the rigidity for an optical spring at this frequency by,

$$K = (2\pi f_{os})^2 m_r = 9.4 \times 10^5 \, \text{N/m}. \tag{4.96}$$
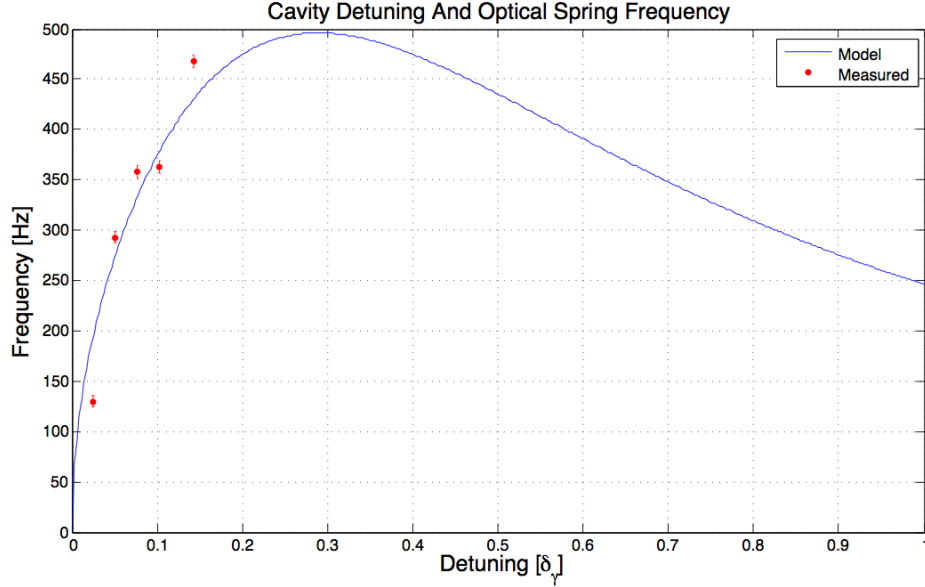
Figure 4.30: *Measured optical spring locations (red) for known injected offsets to laser frequency, and modelled predictions (blue).*

Furthermore, using a beam analyser directly after the input mirror, the approximate beam area was found to be $A = 8.24\,\mu\text{m}^2$. By neglecting the expansion of the beam inside the cavity, which has a total length $L_{AC} = 9.87\,\text{m}$, we can attribute an effective Young's modulus to the stiffness of the light coupling the two cavity mirrors as,

$$E = \frac{K L_{AC}}{A} \approx 1.0 \times 10^{12}\,\text{Pa}. \tag{4.97}$$

To put the result from Equation 4.97 into perspective, we can compare it to the Young's modulus of natural diamond $E_{diamond} = 1.05 \times 10^{12}\,\text{Pa}$ [81], indicating that our investigations on optical rigidity with a fully suspended coupled cavity enabled a effective coupling medium of about the same stiffness as diamond.

We can investigate the locations of measured optical spring frequencies with the cavity detuning, by noting the locations of the 90 degree point in the resonant feature of the phase response and comparing with the numerical model. We

noted that, as is often the case, the 90 degree phase point could be quite well estimated even if the magnitude of the transfer function was distorted. However, it is important to correctly scale the injected offset with the effect that cavity detuning has on the measured error signal. This is achieved by accounting for the change to the internal cavity power for each detuning, since this will reduce the overall size of the peak-peak error signal relative to the injected offset, *i.e.* adjusting the magnitude of injected signals relative to the size of the error signal.

With the above consideration in the numerical model we obtain Figure 4.30, which shows the modelled range of optical spring frequencies expected for a given detuning, along with measured results. The agreement between the model and experiment indicates that the effects resulting from induced optical rigidity are well understood. Discrepancies between the measured and modelled data in Figure 4.30 can be attributed to slight fluctuations in the location of the measured spring during the measurement process, and thermal changes in the laboratory over the time scale of the entire data collection period (approximately 1 hour).

4.8 Conclusions

In conclusion, we have derived the mathematical framework supporting the production of optical springs, optical rigidity and the associated damping effects in mirror systems that are suspended as pendulums, as with gravitational wave detectors. From the analysis a numerical model was developed to investigate the expected behaviour within the Glasgow prototype interferometer where the end mirror and suspension has been modified to enhance sensitivity to radiation pressure effects. The design of a light-weight end mirror mass

and triple-stage suspension was aided using the state space simulation that describes the mirror motion. The reliability of the state space simulation was later validated when observing the expected low frequency pendulum modes in cavity response when the cavity is maintained at the operating point.

A modified triple-stage mirror suspension design was manufactured and installed into one of the prototype interferometer arms to allow experimental investigations into optomechanical behaviour. As is the case for suspended optics interferometers, a significant amount of time was spent making fine adjustments to the system alignment in order to maximise the radiation pressure incident on the cavity mirrors. Furthermore, an adequate method for measuring the optical response was acquired after gaining suitable experience to understand the limitations of cavity detuning and the measurement process. The experimental results indicate a quantitative agreement between the locations of optical spring resonance features and the predictions of the numerical model. In as much as resonances were observed to have a clear phase lead (as opposed to the normal phase lag) behaviour, we also provide qualitative confirmation of the anti-damping associated with a (positive) optical spring.

The largest optical spring observed at $f_{opt} = 496\,\text{Hz}$ corresponds to an optical spring constant of $K_{opt} = 9.4 \times 10^5\,\text{N/m}$, for which an effective coupling medium between the cavity mirrors would have a Young's modulus essentially that of diamond. By implementing such strong rigidity between cavity mirrors it could be possible in future experiments to turn off the control to the cavity mirrors, or laser frequency, whilst maintaining a stable system for lock.

For future experiments, the key is to measure against a laser that is locked to an on-resonance cavity, in order to reduce the background noise. It should be easy to reduce the noise around $500\,\text{Hz}$ from the current level of 1 to $10\,\text{Hz}/\sqrt{\text{Hz}}$ by a factor of more that 1000, thus allowing far more accurate probes of the opti-

cal spring behaviour, particularly in more complicated systems. Additionally, reducing mirror loss and achieving higher circulating power would also provide stronger springs with resonances at even higher frequencies, where noise is also less. However, any increase to the optical spring frequency must at least be restricted to the cavity linewidth, otherwise no characterisation the resonant feature can be performed due to the inherent delay in the cavity response time.

Chapter 5

Conclusions and Future Work

At the time of writing this thesis, many of the laser interferometric ground based gravitational wave detectors that make up the global network have been operating close to or beyond the initial design sensitivity across some of the detection band. Recently there have been engaging and successful tests of the detectors and the subsequent data analysis pipeline by way of hardware injections, validating the operation of the network. Although the current network is yet to make its first direct detection of gravitational waves, there has already been valuable contributions made to the field of observational astronomy as upper limits are placed on several potential sources, such as the stochastic gravitational-wave background [82] and many known radio pulsars [83].

The next steps towards the detection of gravitational radiation and the birth of gravitational wave astronomy depend on implementing new technology successfully within some of the core components of these detectors. LIGO in the US has recently been decommissioned and has entered the first phase of upgrades to Advanced LIGO with the replacement of several key elements such as larger mirror masses, fused silica suspension fibres, increasing the input

laser power and adding a signal recycling mirror to the existing configuration. The combination of each upgrade is expected to make significant progress towards reaching the fundamental limits of these detectors, imposed by quantum nature, which is the result of continuous research and development of new technology and operational techniques performed on prototype systems.

Working at the Glasgow 10 m prototype facility has shown it to be an excellent test bed for rapidly implementing new experiments of importance to the field of laser interferometry. The research presented on diffractively coupled cavities contributes to the necessary characterisation of diffraction gratings in suspended systems and helps to inform the evaluation of such devices for use in future generations of gravitational wave detectors. The numerical model that we developed from the theoretical foundations of grating components shows close agreement with the experimental results, verifying that the system was well characterised and understood. Since our experimental demonstration on three port coated gratings, there have been a host of different novel grating devices, made possible through improvements to the fabrication process, that are currently under investigation and the Glasgow prototype has been a key facility in their final stage testing [84].

The input power to the next generation of detectors, such as Advanced LIGO, is expected to be approximately 200 W, which is an order of magnitude greater than that used in their most recent operation. As the power levels in the arm cavities of the detectors approach 1 MW, radiation pressure will significantly modify the dynamics of the suspended mirrors and it will become necessary to upgrade the control system appropriately. The prototype system at Glasgow has now a fully operational equivalent arm cavity sensitive to radiation pressure effects such as optical spring behaviour, and as the system is upgraded to full digital control, it will be possible to explore optomechanical effects on

the control servo system in greater detail. These investigations will be of value to the recently constructed prototype system in Hannover, where response measurements below the standard quantum limit are soon to commence. Furthermore, throughout the research and development of the triple stage lightweight mirror suspension, several technical issues regarding the small design were highlighted, which were brought to the attention of those involved in the Hannover prototype light-weight suspension. These include:

- Acknowledging the limitations of standard cleaning procedures when concerned with small threaded holes of around 2.5 mm diameter. The standard procedure used at Glasgow relies upon soaking ferris and non-ferris materials separately in an ultra-sonic bath to create microscopic bubbles in an aqueous cleaning solution, which releases contaminants from the surface of submerged material. However, it was noted that the conventional bathing solution was still too viscous to suitably submerge M2.5 threaded holes, resulting in a residue that remained inside several elements. Great care was required to ensure each suspension element was free of oils and trapped material, and provide a vacuum compatible assembly.

- The choice of wire size used to apply signals to the global control actuators is limited by the level of current required for suitable control. In this case the mass and rigidity of each coated copper wire was not negligible, and there was a significant influence on the light-weight reaction mass, resulting in careful positioning to avoid misalignment.

A future experiment at the Glasgow prototype concerned with optomechanical effects from radiation pressure, will involve swapping the input mirror and end mirror, such that a light-weight mirror is coupled between the external and internal cavity. This arrangement is analogous to the optical lever topology.

By implementing a light-weight mirror between two larger cavity mirrors, detuning each cavity to induce an optical spring, and by including an additional measurement device (e.g. an small interferometer) to monitor the position of the light-weight mirror, it is expected that detector sensitivity at frequencies around the optomechanical resonance will be enhanced. Performing such investigations would demonstrate an important proof-of-principle experiment to the wider collaboration and help to inform future designs for the next generation of gravitational wave detectors.

The goal for the current network in the years to come is to isolate the suspension thermal noise, which dominates the low frequency band and higher frequency limiting noise arising from the mirror coatings and internal modes. With these noise sources overcome it may be possible to reach the SQL by squeezing the vacuum state entering the dark port. Over the past few years there has been considerable progress towards the realisation of squeezing technology [85, 86] showing up to $10\,\mathrm{dB}$ improvement across much of the detection band that is otherwise limited by photon shot noise. Recently, this technology has been applied to GEO600 [28], and initial testing was undertaken at the LIGO site before it entered a series of upgrades to Advanced LIGO over the next few years.

The employment of squeezing technology would also enable lower laser power to obtain the level of noise performance required, thus addressing concerns regarding the thermal compensation in high power designs. Future designs of gravitational wave detectors may look to employ both strong optical springs and squeezing to overcome the SQL. In large scale systems, and with greatly improved performance over at least some of the detection band, it is hoped the first direct detection of gravitational waves will follow shortly after and open a new field of gravitational astronomy.

Bibliography

[1] A. Einstein. *Zur Elektrodynamik bewegter Körper*. *Annalen der Physik*, 17:891–921, 1905.

[2] A. Einstein. *Die Grundlage der allgemeinen Relativitätstheorie*. *Annalen der Physik*, 49:769–822, 1916.

[3] B. F. Schutz. *A first course in general relativity*. Cambridge University Press, second edition, 2009.

[4] P. Saulson. *Fundamentals of Interferometric Gravitational Wave Detectors*. World Scientific, Singapore, 1994.

[5] B. Schutz. *Gravitational wave astronomy*. *Classical and Quantum Gravity*, 16:A131–A156, 1999.

[6] V. Kalogera *et al*. *The Cosmic Coalescence Rates for Double Neutron Star Binaries*. *The Astrophysical Journal Letters*, 601(2):L179–L182, 2004.

[7] V. Kalogera *et al*. *The Cosmic Coalescence Rates for Double Neutron Star Binaries*. *The Astrophysical Journal Letters*, 614:L137–L138, 2004.

[8] J. Abadie *et al*. *Predictions for the rates of compact binary coalescences observable by ground-based gravitational-wave detectors*. *Classical and Quantum Gravity*, 27:173001, 2010.

[9] J. H. Taylor, R. A. Hulse, L. A. Fowler, G. E. Gullahorn, and J. M. Rankin. *Further observations of the binary pulsar PSR 1913+16. Astrophysical Journal*, 206:53–58, 1976.

[10] J. H. Taylor and J. M. Weisberg. *Further experimental test of relativistic gravity using the binary pulsar PSR 1913+16. Astrophysical Journal*, 345:434–450, 1989.

[11] M. D. Pitkin. *Searches for continuous and transient gravitational waves from known neutron stars and their astrophysical implications.* PhD Thesis, University of Glasgow, 2006.

[12] A. Hewish *et al. Observation of a Rapidly Pulsating Radio Source. Nature*, 217:709, 1968.

[13] D. R. Lorimer. *Binary and Millisecond Pulsars at the New Millenium. Living Reviews. Relativity*, 4(5), 2001.

[14] K. S. Thorne. *Gravitational Waves. in 'Proceedings of the Snowmass 95 Summer Study on Particle and Nuclear Astrophysics and Cosmology', edited by E. W. Kolb, R. Peccei*, 31:page 1, 1983.

[15] J. Hough, H. Walther, B.F. Schutz, J. Ehlers, H. Welling, I.F. Corbett, and V. Kose. *Proposal for a Joint German-British Interferometric Gravitational Wave Detector. Max-Planck-Institut fur Quantenoptik Report 147 and GWD/137/JH(89)*, 1989.

[16] C. Fabry and A. Pérot. *Théorie et applications d'une nouvelle méthode de spectroscopie interférentielle. Annales des Chimie et des Physique*, 16:115–144, 1899.

[17] A. Buonanno and Y. Chen. *Optical noise correlations and beating the standard quantum limit in advanced gravitational-wave detectors. Classical and Quantum Gravity*, 18(15):L95, 2001.

[18] A. Buonanno and Y. Chen. *Quantum noise in second generation, signal-recycled laser interferometric gravitational-wave detectors. Physical Review D*, 64(4):042006, 2001.

[19] J. Harms, Y. Chen, S. Chelkowski, A. Franzen, H. Vahlbruch, K. Danzmann, and R. Schnabel. *Squeezed-input, optical-spring, signal-recycled gravitational-wave detectors. Physical Review D*, 68(4):042001, 2003.

[20] B. W. Barr. *Experimental Investigations into Advanced Configurations and Optical Techniques for Laser Interferometric Gravitational Wave Detectors.* PhD Thesis, University of Glasgow, 2003.

[21] L. Schnupp. *Presentation at the European Collaboration Meeting on Interferometric Detection of Gravitational Waves (Sorrento, Italy).* 1988.

[22] S. Goßler. *The suspension systems of the interferometric gravitational-wave detector GEO 600.* PhD Thesis, Universität Hannover, Hannover, Germany, 2004.

[23] A. Gillespie and F. Raab. *Thermally excited vibrations of the mirrors of laser interferometer gravitational-wave detectors. Physical Review D*, 52(2):577–585, 1995.

[24] J. Hough, H. Ward, G. A. Kerr, N. L. MacKenzie, B. J. Meers, G. P. Newton, D. I. Robertson, N. A. Robertson, and R. Schilling. *The stabilisation of lasers for interferometric gravitational wave detectors in 'The Detection of Gravitational Waves' edited by David G. Blair.* Cambridge University Press, 1991.

[25] K. A. Strain. *Techniques in Laser Interferometry for the Detection of Gravitational Radiation.* PhD Thesis, University of Glasgow, Glasgow, Scotland, 1990.

[26] C. M. Caves. *Quantum-Mechanical Radiation-Pressure Fluctuations in an Interferometer. Physical Review Letters.*, 45(2):75–79, 1980.

[27] C. M. Caves. *Quantum-mechanical noise in an interferometer. Physical Review D*, 23(8):1693–1708, 1981.

[28] H. Vahlbruch, A. Khalaidovski, N. Lastzka, C. Gräf, K. Danzmann, and R. Schnabel. *The GEO 600 squeezed light source. Classical and Quantum Gravity*, 27(8), 2010.

[29] *www.ligo.caltech.edu.jzweizig.distribution.LSCData.*

[30] T. Accadia *et al. Calibration and sensitivity of the Virgo detector during its second science run. Classical and Quantum Gravity*, 28(2):025005, 2011.

[31] *www.geo600.uni-hannover.de.geocurves.*

[32] K. Kuroda *et al. Japanese large-scale interferometers. Classical and Quantum Gravity*, 19:12371245, 2002.

[33] M. Punturo *et al. The Einstein Telescope: a third-generation gravitational wave observatory. Classical and Quantum Gravity*, 27:194002, 2010.

[34] A. Freise, S. Hild, K. Somiya, K. Strain, A. Viceré, M. Barsuglia, and S. Chelkowski. *Optical detector topology for third-generation gravitational wave observatories. General Relativity and Gravitation*, pages 1–31, 2010.

[35] R. Thielsch, A. Gatto, and N. Kaiser. *Mechanical Stress and Thermal-Elastic Properties of Oxide Coatings for Use in the Deep-Ultraviolet Spectral Region. Applied Optics*, 41(16):3211–3217, 2002.

[36] S. Rowan, J. Hough, and D. R. M. Crooks. *Thermal noise and material issues for gravitational wave detectors. Physics Letters A*, 347(1-3):25 – 32, 2005.

[37] S. D. Penn, P. H. Sneddon, H. Armandula, J. C. Betzwieser, G. Cagnoli, J. Camp, D. R. M. Crooks, M. M. Fejer, A. M. Gretarsson, G. M. Harry, J. Hough, S. E. Kittelberger, M. J. Mortonson, R. Route, S. Rowan, and C. C. Vassiliou. *Mechanical loss in tantala/silica dielectric mirror coatings. Classical and Quantum Gravity*, 20(13):2917, 2003.

[38] D. R. M. Crooks, P. Sneddon, G. Cagnoli, J. Hough, S. Rowan, M. M. Fejer, E. Gustafson, R. Route, N. Nakagawa, D. Coyne, G. M. Harry, and A. M. Gretarsson. *Excess mechanical loss associated with dielectric mirror coatings on test masses in interferometric gravitational wave detectors. Classical and Quantum Gravity*, 19(5):883, 2002.

[39] I. W. Martin, E. Chalkley, R. Nawrodt, H. Armandula, R. Bassiri, C. Comtet, M. M. Fejer, A. Gretarsson, G. Harry, D. Heinert, J. Hough, I. MacLaren, C. Michel, J.-L. Montorio, N. Morgado, S. Penn, S. Reid, R. Route, S. Rowan, C. Schwarz, P. Seidel, W. Vodel, and A. L. Woodcraft. *Comparison of the temperature dependence of the mechanical dissipation in thin films of Ta_2O_5 and Ta_2O_5 doped with TiO_2. Classical and Quantum Gravity*, 26(15):155012, 2009.

[40] A. Bunkowski, O. Burmeister, D. Friedrich, K. Danzmann, and R. Schnabel. *High reflectivity grating waveguide coatings for 1064 nm. Classical and Quantum Gravity*, 23(24):7297, 2006.

[41] G. M. Harry, H. Armandula, E. Black, D. R. M. Crooks, G. Cagnoli, J. Hough, P. Murray, S. Reid, S. Rowan, P. Sneddon, M. M. Fejer, R. Route, and S. D. Penn. *Thermal noise from optical coatings in gravitational wave detectors. Applied Optics.*, 45(7):1569–1574, 2006.

[42] K. A. Strain, K. Danzmann, J. Mizuno, P. G. Nelson, A. Rüdiger, R. Schilling, and W. Winkler. *Thermal lensing in recycling interfero-*

metric gravitational wave detectors. *Physics Letters A*, 194(1-2):124 – 132, 1994.

[43] I. W. Martin and S. Reid. Private Communication, 2010.

[44] A. Bunkowski A. Freise and R. Schnabel. *Phase and alignment noise in grating interferometers.* *New Journal of Physics*, 9(12):433, 2007.

[45] T. Clausnitzer, E.-B. Kley, A. Tünnermann, A. Bunkowski, O. Burmeister, K. Danzmann, R. Schnabel, S. Gliech, and A. Duparré. *Ultra low-loss low-efficiency diffraction gratings.* *Optics Express*, 13(12):4370–4378, 2005.

[46] M. D. Perry, R. D. Boyd, J. A. Britten, D. Decker, B. W. Shore, C. Shannon, and E. Shults. *High-efficiency multilayer dielectric diffraction gratings.* *Optics Letters*, 20(8):940–942, 1995.

[47] K. Hehl, J. Bischoff, U. Mohaupt, M. Palme, B. Schnabel, L. Wenke, R. Bödefeld, W. Theobald, E. Welsch, R. Sauerbrey, and H. Heyer. *High-Efficiency Dielectric Reflection Gratings: Design, Fabrication, and Analysis.* *Applied Optics*, 38(30):6257–6271, 1999.

[48] A. Bunkowski, O. Burmeister, K. Danzmann, R. Schnabel, T. Clausnitzer, E.-B. Kley, and A. Tünnermann. *Demonstration of three-port grating phase relations.* *Optics Letters*, 31(16):2384–2386, 2006.

[49] F. Brückner, T. Clausnitzer, O. Burmeister, D. Friedrich, E.-B. Kley, K. Danzmann, A. Tünnermann, and R. Schnabel. *Monolithic dielectric surfaces as new low-loss light-matter interfaces.* *Optics Letters*, 33(3):264–266, 2008.

[50] F. Brückner, D. Friedrich, M. Britzger, T. Clausnitzer, O. Burmeister, E.-B. Kley, K. Danzmann, A. Tünnermann, and R. Schnabel. *Encapsulated*

subwavelength grating as a quasi-monolithic resonant reflector. Optics Express, 17(26):24334–24341, 2009.

[51] F. Brückner, D. Friedrich, T. Clausnitzer, M. Britzger, O. Burmeister, E.-B. Kley, A. Tünnermann, and R. Schnabel. *Realization of a Monolithic High-Reflectivity Cavity Mirror from a Single Silicon Crystal.* Physical Review Letters, 104(16):163903, 2010.

[52] A. Bunkowsk, O. Burmeister, K. Danzmann, and R. Schnabel. *Input-output relations for a three-port grating coupled Fabry-Perot cavity.* Optics Letters, 30(10):1183–1185, 2005.

[53] A. E. Siegman. *Lasers.* Oxford University Press, 1981.

[54] B. Willke, S. Brozek, K. Danzmann, V. Quetschke, and S. Gossler. *Frequency stabilization of a monolithic Nd:YAG ring laser by controlling the power of the laser-diode pump source.* Optics Letters, 25(14):1019–1021, 2000.

[55] R. Drever, J. Hall, F. Kowalski, J. Hough, G. Ford, A. Munley, and H. Ward. *Laser phase and frequency stabilization using an optical resonator.* Applied Physics B, 31:97–105, 1983.

[56] A. Freise. *An interferometer simulation program.* www.gwoptics.org/finesse.

[57] MathWorks. *A numerical computing environment. www.mathworks.co.uk.*

[58] M. Britzger. Private Communication, 2008.

[59] M. P. Edgar, B. W. Barr, J. Nelson, M. V. Plissi, K. A. Strain, O. Burmeister, M. Britzger, K. Danzmann, R. Schnabel, T. Clausnitzer, F. Brückner,

E.-B. Kley, and A. Tünnermann. *Experimental demonstration of a suspended diffractively coupled optical cavity.* *Optics Letters*, 34(20):3184–3186, 2009.

[60] M. P. Edgar, B. W. Barr, J. Nelson, M. V. Plissi, K. A. Strain, O. Burmeister, M. Britzger, K. Danzmann, R. Schnabel, T. Clausnitzer, F. Brückner, E.-B. Kley, and A. Tünnermann. *Experimental demonstration of a suspended, diffractively coupled Fabry-Pérot cavity.* *Classical and Quantum Gravity*, 27(8):084029, 2010.

[61] J. Hallam, S. Chelkowski, A. Freise, S. Hild, B. Barr, K. A. Strain, O. Burmeister, and R. Schnabel. *Coupling of lateral grating displacement to the output ports of a diffractive Fabry-Pérot cavity.* *Journal of Optics A: Pure and Applied Optics*, 11(8):085502, 2009.

[62] B. W. Barr, M. P. Edgar, J. Nelson, M. V. Plissi, K. A. Strain, O. Burmeister, M. Britzger R. Schnabel, K. Danzmann, J. Hallam, A. Freise, T. Clausnitzer, F. Brückner, E.-B. Kley, and A. Tünnermann. *Translational, rotational, and vibrational coupling into phase in diffractively coupled optical cavities.* Optics Letters, 36:2746–2748, 2011.

[63] ANSYS Inc. *An engineering simulation software program.* *www.ansys.com.*

[64] Advanced LIGO Team. *Advanced LIGO Reference Design.* 2007.

[65] T. Corbitt, D. Ottaway, E. Innerhofer, J. Pelc, and N. Mavalvala. *Measurement of radiation-pressure-induced optomechanical dynamics in a suspended Fabry-Perot cavity.* *Physical Review A*, 74(2):021802, 2006.

[66] V. B. Braginsky, M. L. Gorodetsky, and F. Ya. Khalili. *Optical bars in gravitational wave antennas.* *Physics Letters A*, 232(5):340 – 348, 1997.

[67] F. Y. Khalili. *The "optical lever" intracavity readout scheme for gravitational-wave antennae. Physics Letters A*, 298(5-6):308 – 314, 2002.

[68] M. Rakhmanov. *Dynamics of Laser Interferometric Gravitational Wave Detectors.* PhD Thesis, California Institute of Technology, Pasadena, California, 2000.

[69] M. Husman. *Suspension And Control For Interferometric Gravitational Wave Detectors.* PhD Thesis, University of Glasgow, Glasgow, Scotland, 1999.

[70] C. Torrie. *Development of Suspensions for the GEO600 Gravitational Wave Detector.* PhD Thesis, University of Glasgow, Glasgow, Scotland, 2001.

[71] V. B. Braginsky and S. P. Vyatchanin. *Low quantum noise tranquilizer for Fabry-Perot interferometer. Physics Letters A*, 293(5-6):228 – 234, 2002.

[72] T. Corbitt. *Quantum noise and radiation pressure effects in high power optical interferometers.* PhD Thesis, Massachusetts Institute of Technology, Cambridge, Massachusetts, 2008.

[73] J.-M. Courty, A. Heidmann, and M. Pinard. *Quantum limits of cold damping with optomechanical coupling. The European Physical Journal D*, 17(3):399–408, 2001.

[74] T. Corbitt, C. Wipf, T. Bodiya, D. Ottaway, D. Sigg, N. Smith, S. Whitcomb, and N. Mavalvala. *Optical Dilution and Feedback Cooling of a Gram-Scale Oscillator to 6.9 mK. Physical Review Letters*, 99(16):160801, 2007.

[75] B. S. Sheard, M. B. Gray, C. M. Mow-Lowry, D. E. McClelland, and S. E. Whitcomb. *Observation and characterization of an optical spring. Physical Review A*, 69(5):051801, 2004.

[76] T. J. Kippenberg, H. Rokhsari, T. Carmon, A. Scherer, and K. J. Vahala. *Analysis of Radiation-Pressure Induced Mechanical Oscillation of an Optical Microcavity. Physical Review Letters*, 95(3):033901, 2005.

[77] SolidWorks. *A 3D design solution for creating parts, assemblies and 2D drawings. www.solidworks.co.uk.*

[78] Wolfram Research. *A computational software program. www.wolfram.com/products/mathematica.*

[79] S. H. Huttner, B. W. Barr, J. R. Taylor, M. V. Plissi, B. Sorazu, and K. A. Strain. *Techniques in the optimization of length sensing and control systems for a three-mirror coupled cavity. Classical and Quantum Gravity*, 25(23):235003, 2008.

[80] G. Heinzel. *Advanced optical techniques for laser-interferometric gravitational-wave detectors.* PhD Thesis, Universität Hannover, Hannover, Germany, 1999.

[81] N. Savvides and T.J. Bell. *Hardness and elastic modulus of diamond and diamond-like carbon films. Thin Solid Films*, 228(1-2):289 – 292, 1993.

[82] B. P. Abbott *et al. LIGO: the Laser Interferometer Gravitational-Wave Observatory. Reports on Progress in Physics*, 72(7):076901, 2009.

[83] B. Abbott *et al. Upper limits on gravitational wave emission from 78 radio pulsars. Physical Review D*, 76(4):042001, 2007.

[84] D. Friedrich, B. W. Barr, F. Brückner, S. Hild, J. Nelson, J. Mcarthur, M. V. Plissi, M. P. Edgar, S. H. Huttner, B. Sorazu, S. Kroker,

M. Britzger, E.-B. Kley, K. Danzmann, A. Tünnermann, K. A. Strain, and R. Schnabel. *Waveguide grating mirror in a fully suspended 10 meter Fabry-Perot cavity. Optics Express*, 19:14955–14963, 2011.

[85] H. Vahlbruch, S. Chelkowski, B. Hage, A. Franzen, K. Danzmann, and R. Schnabel. Demonstration of a squeezed-light-enhanced power- and signal-recycled michelson interferometer. *Physical Review Letters*, 95(21):211102, 2005.

[86] H. Vahlbruch, M. Mehmet, S. Chelkowski, B. Hage, A. Franzen, N. Lastzka, S. Goßler, K. Danzmann, and R. Schnabel. *Observation of Squeezed Light with 10-dB Quantum-Noise Reduction. Physical Review Letters*, 100(3):033602, 2008.